NOVEL ORGANIC TANDEM SOLAR CELLS

by

Ernest Adiyiah Asare

Submitted to the Department of Physics

in partial fulfillment of the requirements for the degree of

Master of Science in Physics

at the

Nazarbayev University

April 2023

Author ……...

Department of Physics

April 27, 2023.

Certified ……

Viktor V. Brus

Assistant Professor

Thesis Supervisor.

Accepted by ……..

Gonzalo Hap Hortelano

Dean, School of Science and Technology

NOVEL ORGANIC TANDEM SOLAR CELLS

by

Ernest Adiyiah Asare

Submitted to the Department of Physics
in partial fulfillment of the requirements for the degree of
Master of Science in Physics

Abstract

Organic tandem solar cells have attracted significant attention as a promising technology for next-generation photovoltaics due to their potential to achieve high power conversion efficiencies. In this study, we present a simulation-based approach using transfer matrix modeling to investigate the optical and electrical properties of organic tandem solar cells. We investigate the influence of different device parameters such as the thickness of the active layers on the device performance. The simulation results demonstrate that the optimized thicknesses of the active layers involved in the tandem structure can significantly improve the short circuit current J_{SC} thereby increasing the power conversion efficiency compared to the single-junction solar cells. Additionally, the transfer matrix model provides a comprehensive understanding of the optical behavior of the device, including the absorption and reflection of light at different interfaces. These results provide valuable insights into the design and optimization of high-performance organic tandem solar cells.

Thesis Supervisor: Viktor V. Brus
Title: Assistant Professor

Acknowledgments

First and foremost, I thank God for the gift of life and strength. Prof. Viktor Brus, who served as my advisor, has my sincere gratitude for his unwavering encouragement, tolerance, and especially throughout this project. A special thanks goes out to Prof. Ernazar Abdikamalov for his invaluable counsel and support throughout my time at Nazarbayev University. Special thanks to Dr. A. Mostovyi, Dr. S. Mykhailo, Dr. H. Parkhomenko and all other members of our research group for their invaluable assistance. For their direct or indirect assistance during my studies and research, I am grateful to the faculty and employees at the Department of Physics. Finally, I want to thank my parents for their help with this project.

Table of Contents

List of Figures

List of Tables

CHAPTER ONE

INTRODUCTION

1.1 Background and Motivation

Energy crises have continually become a major challenge in today's world [1]. The dependency on non-renewable energy sources are unreliable, this calls out to the maximum utilization of our renewable energy sources such as the solar, which is possible to be converted to usable energy (electricity) with the use of solar cells [2,3]. It is amazing how the usage of solar cells has increased gradually across the world yet still the electricity that is sourced from photovoltaics (PV) globally is less than 3% [4]. PVs are projected to be the promising component in the energy market as we seek to achieve carbon free electricity and focus on clean energy worldwide , which will influenced a new level of renewable technologies in the future [4–6]. Due to this increasing demand, the US Department of Solar Energy Technologies Office (SETO) targets to increase the usage of solar technologies to help achieve decarbonization goals set by the Government by 2035 [7].

Since the discovery of photoelectric effect by Alexandre-Edmond Becquerel in 1839 and invention of solar cells by Russel Ohl in 1946, it has been a ground breaking device and a major subject of focus in research till date [6,8,9]. It works on the following mechanism: It absorbs light (photons) from the solar spectrum to generate charge carriers (electrons and holes), these carriers are then separated and collected by their corresponding electrodes set up a potential difference across the p-n junction, and as a result of movement (mobility) of these charge carriers electricity is generated [8].

Solar cells can be categorized in to first (1^{st}), Second (2^{nd}) and third (3^{rd}) generations based on the different types of materials they are made from as shown in Figure 1 [10,11]. The 1^{st} generation of solar cells are based on silicon crystalline wafers; single/mono and poly/multi-

crystalline. The single/mono-crystalline is made from a single crystal of silicon and widely used in photovoltaic industry for mass production of solar cell due to their high efficiency ~27.6% and stability, whereas, poly/multi-crystalline are manufactured from two or more different crystals and are cheaper to fabricate but have low efficiency ~23.3% compared to the single crystalline [8,12]. Amorphous silicon (a-Si), cadmium-telluride (CdTe), Gallium Arsenide (GaAs) and copper indium gallium di-selenide (CIGS) are thin film solar cells which forms the 2nd generation of solar cells and could have a thickness of 1000nm [13,14]. The a-Si has low efficiency 14% but cheaper fabrication cost compared to crystalline silicon with efficiency range of 22.3 – 27.6% [15,16]. For the CdTe semiconductor, it absorbs light easier because of its direct band and have efficiency of 22.1%, but the Cd material is not environmentally friendly and hence this affects its usage and technology [11,17]. CIGS, just as the CdTe is also a direct band gap semiconductor with high efficiency ~23.4% and have along life span since it degrades slowly [18]. GaAs have a similar crystal structure just like that of silicon with much higher efficiency ~31.3% and high light absorption. The 3rd generation of solar cells consist of nano crystals, dye, concentration, and polymer based, and perovskite solar cells [8,19]. The nano crystal based solar cells have termed as Quantum dots [20]. For dye sensitized solar cells, dye molecules are placed in the middle of electrodes, they have easy processing methods but degrade at a faster rate when exposed to ultraviolet and infrared radiation [21,22]. Concentrated solar cells use optics to accumulate sunlight onto a small region of the solar cell to generate large amount of heat which is used be heat engines in power generators [8,23]. nanometers crystal and

tunable size mostly

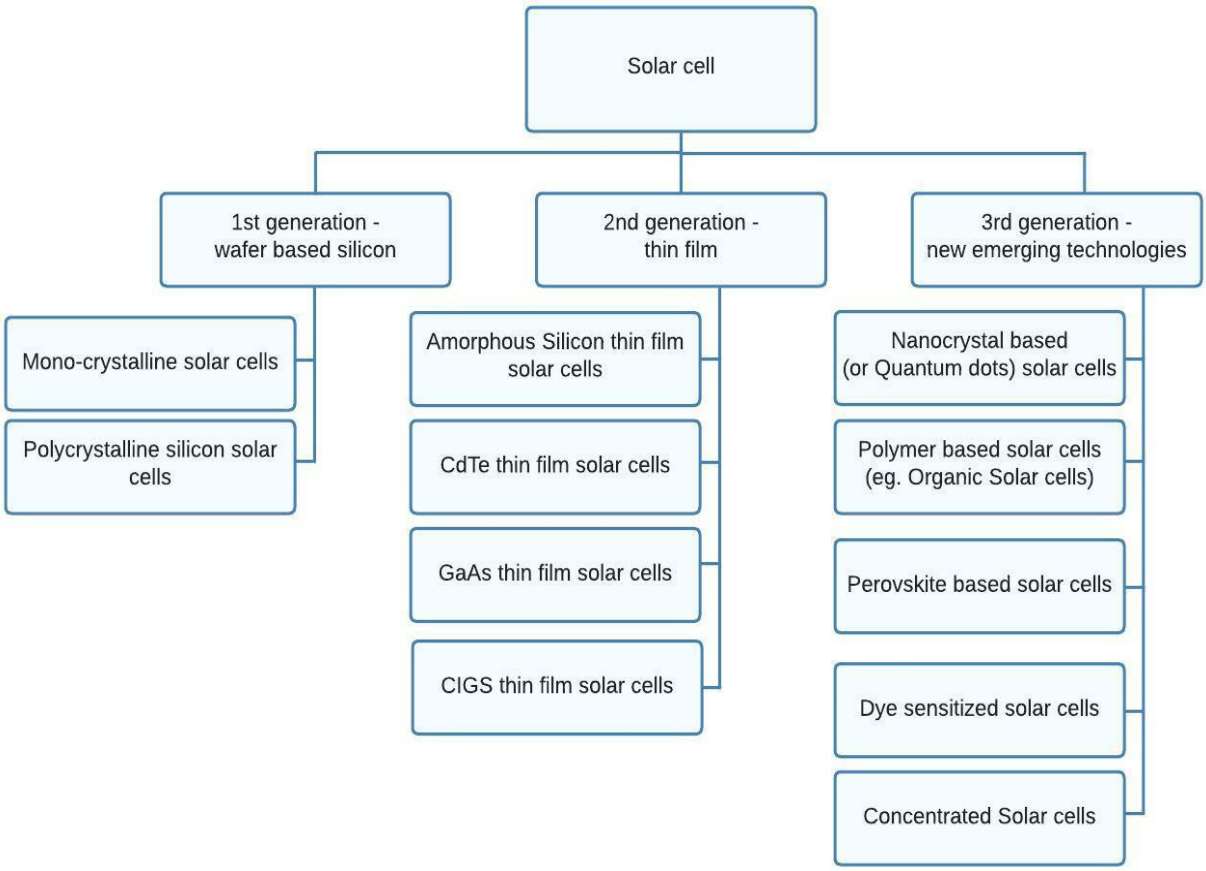

Figure 0.1:Types of solar cells and their trends of development [8,9,20].

termed as Quantum dots [20]. For dye sensitized solar cells, dye molecules are placed in the middle of electrodes, they have easy processing methods but degrade at a faster rate when exposed to ultraviolet and infrared radiation [21,22]. Concentrated solar cells use optics to accumulate sunlight onto a small region of the solar cell to generate large amount of heat which is used be heat engines in power generators [8,23]. The polymer solar cells also works on the photovoltaic effect and has huge applications in stretchable or flexible solar technology due to it polymer substrate [8,24–29]. Talking of generations of solar cells, perovskite solar cells just like

OSCs are one of the newest discovery with numerous advantages over the existing ones though it requires more research to commercialized it [30–32].

Improving the efficiency of solar cells is the major concern of researchers and manufacturing industries as it stands in the present day, this has led to the development of all kinds of device structures such as tandem, homo-tandem, and ternary solar cells. And this permits the optimization of semiconductor materials to improve the efficiency [3,33,34]. However, the pace at which single junction solar cells approaches the Shockley Queisser (SQ) limit is overwhelming, the good news is that tandem solar cells promises to exceed the SQ limit of single-junction solar cells [35–38]. This tandem solar cells assures a reduction in the two main fundamental losses of a single junction solar cells: Transmission loses due to unabsorbed incident photons, and thermalization loses due to electrons losing of excess energy and thermalizing to edge of the conduction band [33,35,39,40]. Though recombination and junction losses are types of losses in the solar cell, but the two main fundamental losses of a solar cell are the transmission(transparency) and thermalization losses since they contribute 55% of the total losses [37].

This has influenced our motivation to dive in to how to generate high generation rate and short circuit current for the whole tandem device by optimizing material properties and showing some fundamental design requirements for high efficiency.

1.2 Tandem Solar Cells

Tandem solar cells (TSCs) are classified based on how the junctions between the top and bottom cells in the device are electrically and optically coupled [41]. Types of TSCs includes: 2-terminal (2T) solar cells which are known as monolithic tandem solar cells, 4-terminal (4T) tandem solar cells known as mechanically stacked TSCs, and optically splitting TSCS [41–45].

1.2.1 2T Tandem Solar Cells (Monolithic Solar Cells)

The top and bottom cell of the 2T structure are fabricated directly on top of another with the aid of intermediate connecting layer (ICL) or intermediated recombination layer (IRL) under appropriate temperature conditions on the active layers as shown in Figure 2(a) [41,46]. Less conductive layers that are used in the device fabrication minimizes parasitic absorption and increases photocurrent generation [41]. This current obeys Kirchhoff's law but it is limited by material properties of the sub cells such as band gap energy and thickness, also, there is a voltage loss at the tunnel junction which reduces the overall voltage [46]. The 2T TSC is cost effective because it requires only one substrate and one external circuit in its device architecture. And the electron transport layer (ETL) is facilitated by inter-band tunnel junction [41].

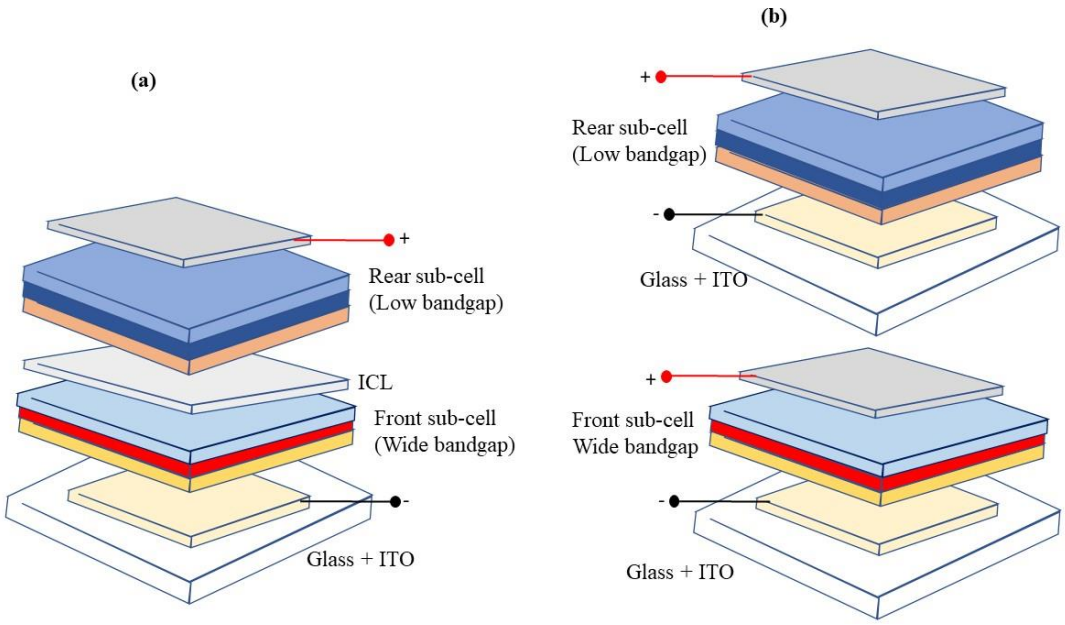

Figure 0.2:Graphical representation of (a) 2-Terminal (2T) Tandem solar cell. (b) 4-terminal (4T) tandem solar cell.

1.2.2 4T Tandem Solar Cells (Mechanically stacked tandem solar cells)

The top and bottom cells are fabricated separately and are stacked up on each other mechanically for the 4T TSCs as shown Figure 2(b) [3,35,41,46]. Due to the separate fabrication of the top and bottom cells of the 4T TSCs, the whole device is less affected by temperature, low level of disorderliness and minimized stress, and are more controllable [41,47–49]. A high power conversion efficiency (*PCE*) of 31.3% has been achieved with perovskite tandem structure, but theoretically it can achieve *PCE* of 46% [46,50].

1.3 Working Principles and Design Requirements for Polymer Tandem Solar Cells

Polymers are large molecules surrounded by electrons that occupies large number of sets of molecular orbitals (these molecular orbitals represent energy levels) [51]. The most important molecular orbitals of the polymer are the highest occupied molecular orbital (HOMO) and lowest unoccupied molecular orbital (LUMO). The highest energy molecular orbital occupied by electrons is the HOMO, whereas the LUMO is the next highest energy that are unoccupied by electrons (i.e., the next highest empty molecular orbital) [51,52]. Therefore, the energy difference between HOMU-LUMO is considered as energy gap (band gap), and this indicates the lowest energy to excite an electron in that polymer.

Polymer solar cells absorb light in an analogous manner as inorganic ones, but the charge generation is different. The carrier charges are generated through four stages: light absorption, exciton diffusion, charge separation and charge extraction. A photon is absorbed by the electron donating material promoting a valence electron to a conduction exciton [52]. Worth bearing in mind that these excitons are not just free charge carriers, there is a binding energy or force that binds the electron-hole (e-h) pair of the exciton together [52]. If the exciton is closer enough to donor-accepter (D-A) interface, then the exciton will encounter an electric field called built-in potential which will break the binding energy [52,53]. This causes the e-h pair to separate, and

electron to move into the acceptor and the hole to move into the Donor material. Each carrier will drift till the electron reach the cathode electrode and the hole to the anode, creating a current and producing a voltage as shown in Figure 3 [52,53].

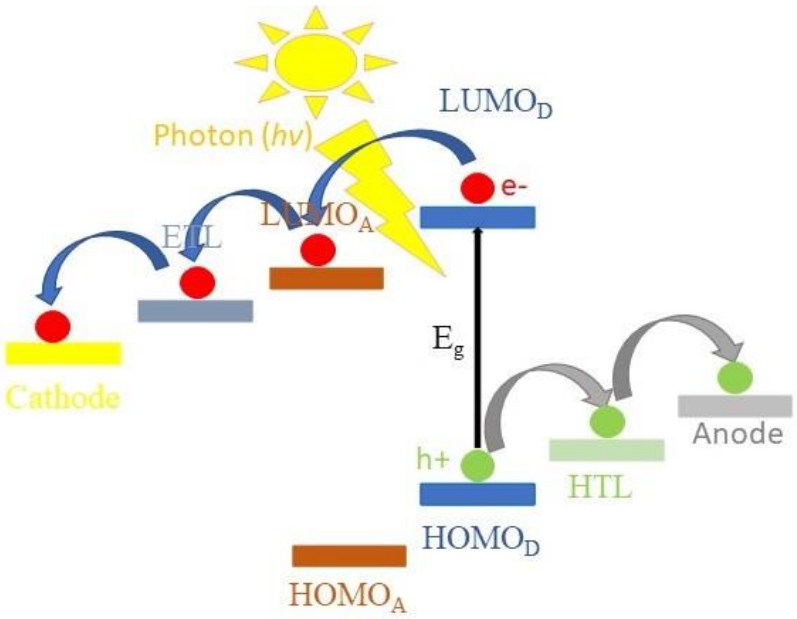

Figure 0.3:Energy diagram as well as charge transport process of inverted single BHJ solar cell.

It must be noted that the magnitude of the built-in potential is the energy difference between the LUMO of the donor and the LUMO of the acceptor material as shown in Fig.3. The magnitude of the open circuit voltage (V_{OC}) is affected by the energy difference between the HUMO of the Donor and the LUMO of the acceptor material. But experimentally, the equation of the V_{OC} is given as [54]:

$$V_{OC} = \frac{1}{e}\left(|E_{HOMO}^{Donor}| - |E_{LUMO}^{Acceptor}|\right) - 0.3\ eV \qquad (1.1)$$

It is reported that there is a loss of 0.3 eV from total V_{OC} that is calculated from the magnitude of the energy difference between the Donor and the LUMO of the acceptor material, though this additional loss reported is still under massive review [54]. Whereas the narrower the band gap

the higher short circuit density (J_{SC}), though it is affected by carrier mobility, intermolecular interaction and molecular chain packing [53]. Also, the donor and acceptor material must have different electron affinities and ionization potential.

In principle, tandem solar cells consist of two light-absorbing semiconductor active layers with different or the same band gap. When these two layers are the same, we have homo-tandem solar cells. The different active layers or sub cells enhances broader absorption of the solar spectrum and in effect reduces the absorption and thermal losses [55,56].

Tandem solar cells can be connected in series or parallel depending on the intermediate connecting layer (ICL) and Figure 1.4 shows how the sub-cells can be connected [55,57]. A key thing to note of the 2-terminal TSCs connected in series is the short circuit current density (J_{SC}) matching of the top and bottom sub-cells. J_{SC} of top and bottom cells of 2T TSCs connected in series must be the same since the current density of the whole device is limited by the minimum J_{SC} of the sub-cells[58]. Whiles the open circuit voltage (V_{OC}) of whole tandem device is the sum of the V_{OC} of the individual sub-cells [57,59–64]. The fill factor (*FF*) of the series connected device is also limited by the *FF* of the top cell. The *FF* of the whole device decreases when the *FF* of the top cell decreases and vice versa, however, the *FF* of the tandem device is higher than that of the top cell [65].

For parallel connected TSCs, V_{OC} of the whole tandem devices is limited by the V_{OC} of the minimum sub-cell, hence V_{OC} matching of the top and bottom cells are important, whiles the J_{SC} of the whole tandem device is the sum J_{SC} of the individual sub-cells [55,57,65,66]. Also, the *FF* of the parallel devices is the average of the *FF* of the subcells [65]. The ICL forms an integral part of the monolithic TSCs, it has major influence of the series and parallel connection. In a traditional TSCs structures, the quasi-fermi level that exists between the tandem solar cell.

The ICL forms an integral part of the monolithic TSCs, it has major influence of the series and parallel connection. In a traditional TSCs structures, the quasi-fermi level that exist between the donor in the top cell and the acceptor in the bottom cell needs to be aligned for a series connection, and for inverted structures there must be an alignment between the acceptor in the top cell and the donor in the bottom cell.

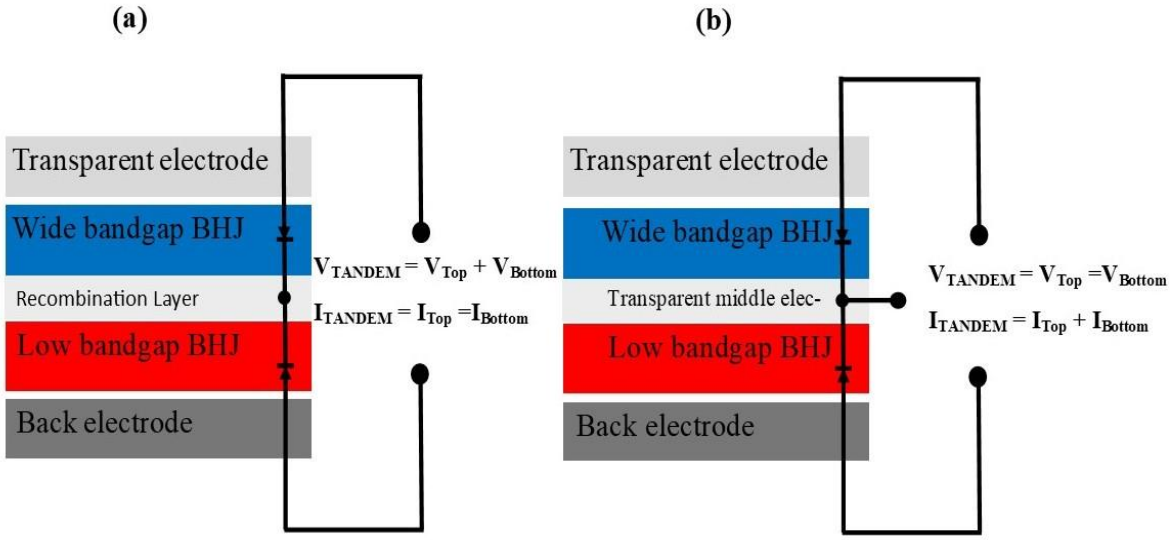

Figure 0.4:Schematic diagram of a). Series connected tandem solar cell b). Parallel connected.

The ICL in this series connected monolithic tandem devices in this case acts as a recombination layer, and its role is to counterbalance the recombination of the electrons extracted from one sub-cell with holes from the other the sub-cell [57]. The negative effect of the ICL is that it could absorb light that is supposed to reach the sub-cells there by increasing optical losses, therefore a highly transparent ICL is always recommended to reduce optical losses. It must be noted that, the carrier recombination zone of the ICL can enhances the lossless recombination of electrons and holes from their corresponding sub-cells and in general can reduce or avoid completely V_{OC} losses in the TSCs [57].

Compared to the parallel connected TSCs, the boundary of the two sub-cells at the junction of the ICL must have the same polarity, therefore, the ICL acts as an intermediate electrode (common electrode) to these sub-cells to compensate this design requirements [57,66]. The performance of the parallel TSCs hugely depends on this intermediate electrode since it must be highly transparent to reduce optical losses, low impedance to facilitate resistance loss, and at the same time it must be conductive to enough to interconnect the sub-cells for high efficiency of the tandem device [57,66,67]. Presently, it is difficult to fabricate an intermediate electrode that is highly conductive and transparent enough, by virtue of this, series connected configurations are by far highly efficient and mostly preferred than their parallel counterpart[57,67,68].

In general, it can be noted that the active layers of the TSCs must be good absorbing materials and should have different absorption spectra to reduce mutual parasitic absorption in the sub-cells [68]. *PCE* of the TCSs is strongly affected by changing the material or thickness of any of the active layers since these changes the top and bottom sub-cells alignment and the tandem J_{SC} [68].The active layers of the tandem solar cells can be grouped into three types depending on the bandgaps: wide, lower, and medium bandgap. Wide bandgap materials are semiconductors with band gaps higher than 1.70 eV, whereas lower bandgap materials have band gaps lower than 1.50 eV and materials with bandgap between 1.50 and 1.70 eV are medium bandgap [57].

CHAPTER TWO

2 LITERATURE REVIEW

2.1 Organic Tandem Solar Cells

Organic solar cells (OSCs) are classified as polymer or small molecule solar cells, their active layers are made up of donor and acceptor polymers as aforementioned. Tang's group was the first to report a bilayer structure in 1986, and in 1995, Yu et al inverted an internal donor-acceptor heterojunction called bulk heterojunction (BHJ) layer to improve the structure [69–71]. In the bilayer structure one layer is grown on the other, hence there is a small phase area between the donor and acceptor units. And this reduces charge separation causing charge carries to travel shorter distance (low diffusion length) between 10 to 40nm before reaching their respective electrodes [72–75]. Consequently, there is a high recombination process associated with bilayer structure because of the low diffusion length which hinders device performance. Unlike bilayer, a solution of donor and accepter materials are heterogeneously mixed in BHJ structures to create a more different phases aiding in ultrafast charge transfer due the their longer exciton diffusion length [72,76]. With all this improvement on active layer structure, generally, organic solar cells have low *PCE* and improving the device includes finding appropriate donor-acceptor material combination to produce the needed built-in potential for the exciton dissociation and increasing the optical absorption spectra of the active layer. The challenge regarding to this is to narrow the band gap without sacrificing the built-in potential and maximizing V_{OC} [72]. Although, increasing the thickness of the active layer improves its absorption spectral but increases recombination of charge carries due to low diffusion length of exciton of OSCs [72]. This requires that, for ultrafast charge transfer within the BHJ a thin or ultra-thin film layer is needed.

Therefore, a TSC designed with different thin top and bottom active layers is required to harvest different light spectrum to broaden the absorption spectra of the OSCs.

The conventional structure of 2T TSCs make use of indium tin oxide (ITO) as anode electrode and the top cathode electrode as a metal [77]. In 2007 a breakthrough of *PCE* of 6.5% was reported by Kim et al. where they incorporated this conventional structure and made use of titanium oxide (TiO_2) and PEDOT:PSS as ETL and HTL respectively [77,78]. Whereas the ITO electrode is used as the cathode and the top metal as the anode electrode [77]. In 2011 another breakthrough of PCE of 8.6% was reported by Dou et al. where they incorporated the inverted structure and made use of zinc oxide (ZnO) and PEDOT:PSS as the ETL and HTL respectively [77,79]. The inverted structures outmatches the conventional ones and are generally preferred because: the ETL materials have low work function and could decrease the stability of the cell if used on top of the active layer, due to film morphology of BHJ the ETL increases carrier generation efficiency when it first get into contact with the light, there is a higher built-in potential and there is a finer charge selectivity since HTL make use of MoO_3 in the inverted structure [77,80–83]. Also, the front cell of organic TSC make use of wide band gab active layer whiles the bottom cell make use of low bad gap absorbers [77].

The materials that are used as the donors and acceptors in the active layer OSCs varies. Within the last two decades fullerenes and their derivatives including phenyl-C_{61}-butyric acid methyl ester ($PC_{61}BM$) and phenyl-C_{71}-butyric acid methyl ester ($PC_{71}BM$) have dominated as electron acceptor materials because of their high electron affinities and better charge transport in BHJs. However, fullerene based OSCs have unprecedented challenges: weak absorption in the visible region, low morphological stability, fixed energy levels, and bad flexibility [84]. In a bid to increase the efficiency of OSCs, new materials such as non-fullerene (NFA) or small molecule

acceptors have been developed. They have diverse material configuration strategies, less parasitic absorption, and different methods of synthetization. With the use of NFA the *PCE* of the OSCs has increased from 12-20.2% [85]. Overall, the advantage that comes with OSCs is its solution processability.

As aforementioned, the tandem solar cell requires different narrow and wide band gap materials, hence there are state-of-the-art D-A materials based on their configuration that are used such as wide and narrow-bandgap polymer donors, wide and narrow-bandgap small molecule (oligomeric) donor and, wide and narrow-bandgap nonfullerene acceptors.

2.2 Review of some fullerene and non-fullerene polymer organic tandem solar cells

The first double-junction tandem polymer solar cells was reported by Hadipour et al. in 2006 with a high V_{OC} of 1.4 V and very low PCE ~ 0.57% [86]. Kim et al. in 2007 fabricated an OTSC with a *PCE* of 6.5%, where they used two polymer-fullerene BHJ layers; poly[2,6-(4,4-bis-(2-ethylhexyl)-4*H*-cyclopenta[2,1-b;3,4-b'] dithiophene)-*alt*-4,7-(2,1,3-benzothiadiazole)] (PCPDTBT) and [6,6]-phenyl-C_{61} butyric acid methyl ester (PCBM) as the front electrode, and poly(3-hexylthiophene) (P3HT) and [6,6]-phenyl-C_{71} butyric acid methyl ester ($PC_{70}BM$) as the back cell [78]. In this device they used TiO_x-PEDOT:PSS as the ICL and attained 1.24V and 7.8 mA/cm^2 as V_{OC} and J_{SC} respectively.

Hagemann et al. in 2008 reported all solution processed tandem polymer solar cell based on thermocleavable materials which was stable in air without any encapsulation [87]. The front cell consisted of a zinc oxide nanoparticles, a large band gap active layer based on a bulk heterojunction between zinc oxide and poly(3-carboxydithiophene) (P3CT) followed by a layer of PEDOT:PSS [87]. Whereas the bottom made use of a zinc oxide front cathode processed on top of the PEDOT:PSS layer from an organic solvent, a low band gap active layer based on a BHJ between zinc oxide and the novel poly(carboxyterthiophene-*co*-diphenylthienopyrazine)

(P3CTTP) followed by a layer of PEDOT:PSS again processed from water and finally a printed silver electrode [87]. The tandem device resulted in J_{SC} ~ -0.15 $mAcm^{-2}$,V_{OC} ~ 0.54 V, *FF* ~ 25.8 and *PCE* ~ 0.02 [87].

An homo tandem monolithic fullerene device consisting of BHJ poly(3-hexylthiophene) and 1-(3-methoxycarbonyl)-propyl-1-phenyl-(6,6)C61(6,6)C61 as active layer of the sub-cells was reported by Sun et al. in 2010 [88]. The device employed high transparent, low series resistance and effective recombination center ICL: ultrathin multiple metal layers of Ca/Al/Ag and metal oxide MoO_3 [88]. The device yielded a V_{OC} ~ 1.18 V, high *FF* ~ 61.88% and *PCE* ~ 2.78% under simulated 100 $mWcm^{-2}$ solar irradiation [88].

Sakai et al. reported BHJ fullerene tandem devices device with a novel transparent multi-film metal oxide LiF/indium tin oxide (ITO)/MoO3 as the ICL [89]. They employed P3HT:bis[60]PCBM as the top cell and P3HT:[70]PCBM as the bottom cell, where the the device achieved J_{SC} ~ 6.14 $mAcm^{-2}$, V_{OC} ~ 1.14 V , *FF* ~0.737 and *PCE* 5.16% [89].

In 2011, Chou et al. made an interesting progress by employing MoO_3/Al/ZnO a metal-oxide as the ICL for BHJs polymer tandem solar having an inverted structure [90]. The metal oxide ICL was stacked in between BHJ top cell poly[(4,4 ′ -bis(2-ethylhexyl)dithieno[3,2-b:2 ′ ,3 ′ -d] silole)-2,6-diyl-alt-(2,1,3-benzothiadiazole)-4,7-diyl] (PSBTBT) : $PC_{70}BM$ and a bottom cell made of BHJ poly(3-hexylthiophene) (P3HT): [6,6]-phenyl C 61 butyric acid methyl ester ($PC_{60}BM$) layer [90]. The absorption of the whole device including the MoO_3/Al/ZnO ICL exceeded 0.8 optical density (O.D.) in the range of 350-600 nm and extend to 0.3 O.D at 750 nm [90]. Due to high transmittance of the MoO_3/Al/ZnO layer exceeding 95%, there were less optical losses in the UV-visible-NIR region and it also served as a good charge recombination

center in the monolithic tandem device [90]. This device yielded a V_{OC} ~ 1.20 V, J_{SC} ~7.84 $mAcm^{-2}$, *FF* ~ 54.1%, *PCE* ~ 5.1 and a very low series resistance of 2.27 Ωcm^{-2} [90].

Dou et al. in 2012 employed a low-band gap conjugated polymer poly{2,6′-4,8-di(5-ethylhexylthienyl)benzo[1,2-*b*;3,4-b]dithiophene-alt-5-dibutyloctyl-3,6-bis(5-bromothiophen-2-yl)pyrrolo[3,4-*c*]pyrrole-1,4-dione} (PBDTT-DPP) with energy gap ~ 1.44 eV and absorption onset of 858nm in their novel TCS to increase the *PCE* of polymer solar cell to 8.26% [79].
In 2016 Zheng et al. achieved a *PCE* of 11.62% with polymer tandem solar cells, where they employed a low band gag polymer PDPP4T-2F (poly(2,5-bis(2-decyltetradecyl)- pyrrolo[3,4-c]pyrrole-1,4(2H,5H)-dione-3,6-diyl-*alt*-3″,4′-difluoro-2,2′:5′,2″:5″,2‴-quaterthiophene-5,5‴-diyl) donor with high absorption edge (900nm) for the sub-cells [91].

As aforementioned, fullerene based OSCs have weak absorption in the visible region, low morphological stability, fixed energy levels, and bad flexibility Hence fullerene free polymers offer a better solution due to their diverse material configuration strategies, less parasitic absorption, and different methods of synthetization.

In 2016 Liu et al. manufactured the first small-molecule fullerene free (nonfullerene-based) tandem OSCs where they employed poly(3-hexyl-thiophene) as the donor and spirobifluorene (SF) core with four benzene endcapped diketopyrrolopyrrole (DPP) arms positioned on it as the acceptor for the front cell and; (P3HT:SF(DPPB)4) and PTB7-Th:IEIC bulk heterojunctions as the front and back subcells respectively. *PCE* ~ 8.48% and an outrageous V_{OC} ~ 1.97 V was achieved [92]. In that same year Zhang et al. fabricated tandem OSCs that make use of oligomer-like small molecule donor as the front cell DR3TSBDT:$PC_{71}BM$ with high *PCE* ~ 11.47% [93].

Zuo et al. reported a high efficiency non-fullerene tandem organic solar cell with a parallel configuration in 2017, this device had an improved proton-to-electron response over a large spectra range (450 to 800nm). It had an improved fill factor due the recombination loss enhancement which resulted in high *PCE* of >10% [94]. In a bid to increase the efficiency of the tandem device, Chen and his group developed a tandem device that have thermal-treatment-free buffer layer by employing poly[(9,9-bis(3′-(*N*,*N*-dimethylamino)propyl)-2,7-fluorene)-*alt*-2,7-(9,9-dioctyl fluorene)] (PFN) for both front and bottom cell [95]. A high *PCE* ~ 10.79% was achieved due to the much improved *FF* ~72.44% [95]. Chen et al. also reported non-fullerene homo-tandem-device OSCs with solution processed RCL: diethyl zinc precursor-based ZnO layer processed on PEDOT:PSS with mild thermal annealing treatment~ 80°C [96]. The device has a *PCE* ~10.8% and with outrageous V_{OC} > 2.1V [96].

Zhang and his group achieved a remarkable *PCE* ~14.11% in 2018, by employing in both top and bottom cells high efficient NFAs: F-M and NOBDT with phenomenal absorption range from 300 to 900 nm blended with wide band gap polymerspoly[(2,6-(4,8-bis(5-(2-ethylhexyl)thiophen-2-yl)-benzo[1,2-b:4,5-b′]dithiophene))-*alt*-(5,5-(1′,3′-di-2-thienyl-5′,7′-bis(2-ethylhexyl)benzo[1′,2′-c:4′,5′-c′]dithiophene-4,8-dione))] (PBDB-T) and narrow bandgap polymer PTB7-Th, [97]. Guo et al. reported a high *PCE*~14.2% by combining sub cells of NFA; 2,2′-((2*Z*,2′*Z*)-(((4,4,9,9-tetrakis(4-hexylphenyl)-4,9-dihydro-*s*-indaceno[1,2-*b*:5,6-*b*′]dithiophene-2,7-diyl)bis(4-((2-ethylhexyl)oxy)thiophene-5,2-diyl))bis(methanylylidene))bis(5,6-difluoro-3-oxo-2,3-dihydro-1*H*-indene-2,1-diylidene))dimalononitrile (IEICO-4F) and fullerene acceptors;$PC_{71}BM$ for a tandem architecture [98]. A semitransparent tandem organic solar cell with broad absorption from 300 to 1000nm of *PCE*~10.5% and average transmittance 20% was reported by Chen et al. where they

made use for perylene diimide (PDI)-based non-fullerene active layer of P3TEA:FTTB-PDI_4 for the front cell, and narrow-bandgap SMA, IEICS-4F for the back cell [99]. An outrageous *PCE* of 17.36% was achieved by Meng et al by employing NFA: F-M in the front cell of 2T monolithic tandem device with a high V_{OC}~ 1.64V [100].

In 2019, Liu's reported a *PCE* of 15% for the organic tandem device where they employed a fluorine-substituted wide-bandgap nonfullerene acceptors: TfIF-4FIC with a core of fused nonacyclic unit and end capping groups of 2-(5,6-difluoro-3-oxo-2,3-dihydro-1*H*-inden-1-ylidene)malononitrile for the front cell [101]. There was a minimal energy lost since the device blended well with a bottom cell: PTB7-Th:PCDTBT:IEICO-4F. Meng et al. achieved high *PCE*~14.52% and V_{OC}~ 1.82V by using identical polymer donor: NNBDT for the tandem device [102]. A well reduced charge recombination tandem device was reported by Liu's group with *PCE* of 14.2% where they made use of NFA: Y1 for both sub cells with the same polymer donor, and having a high *FF*~ 77% [103].

In 2021, Tavakoli et al. reported an air-stable tandem device with well-enhanced transporting layers and reduced photovoltaic losses, by incorporating SnO_2 nano particles as the ETL for both sub cells and PEDOT:poly(styrenesulfonate) (PSS)/Ag (1 nm)/SnO_2 as a recombination layer [104]. A *PCE* of 15.2% was obtained from the NFA active layers; PM6:Y6 (top cell) and a polymer accepter (bottom cell) [104].

A groundbreaking record of OTSCs exceeding *PCE* > 20% was first reported by Zheng et al. by employing a well advanced ICL made of electron beam evaporated TiO_X (e-TiO_X)/ PEDOT:PSS, where the structure of the device made use of PBDB-TF:BTP-eC9 as the top cell and PBDB-TF:GS-ISO as the bottom cell [85]. *PCE* ~ 18.67% of a tandem device was reported

by Huang's group in 2022, consisting of a fluorene core NFA was employed as the wide band gap front cell: D18:F-ThBr, and the bottom cell made use of CH1007 acceptor [105].

Table 2.1: Optoelectronic properties of tandem devices.

Bottom Electrode	**Front active layer**	**ICL**	**Back active layer**	**Top electrode**	**J_{SC} [$mAcm^{-2}$]**	**V_{OC} [V]**	**FF [%]**	**PCE [%]**	**Ref.**
ITO/PEDOT	PFDTBT:PCBM	LIF/AL/Au/PEDOT	PTBEHT:PCPM	Al	9	1.4	55	0.57	[86]
ITO/PEDOT:PSS	PFTBT:$PC_{61}BM$	ZnO/n-PEDOT:PSS	pBBTDPP2:$PC_{61}BM$	LiF/Al	6.00	1.58	52.0	4.90	[106]
ITO/PEDOT:PSS	PBDB-T:F-M	ZnO/n-PEDOT:PSS	PTB7-Th:NOBDT	PDINO/Al	11.72	1.71	70	14.11	[97]
ITO/PEDOT:PSS	PBDB-T-2F:TfIF-4FIC	PF3N-2TNDI/Ag/PEDOT:PSS	PTB7-Th:PCDTBT:IEICO-4F	PF3N-2TNDI/Ag	13.6	1.60	69.0	15.00	[101]
ITO/PEDOT:PSS	P3HT:$PC_{71}BM$	ZnO/PEDOT:PSS	PSBTBT:$PC_{71}BM$	Al	6.93	1.45	63.71	6.38	[107]
ITO/PEDOT:PSS	BDT-ffBX-DT:SFPDI	PIF-PMIDE-N:PNDIT-F3N(4:1)/ Ag/PEDOT:PSS	BDT-ffBX-DT:SFPDI	PIF-PMIDE-N/Ag	5.00	2.39	55.0	6.50	[108]
ITO/PEDOT:PSS	PCDTBT:$PC_{71}BM$	ZnO/n-PEDOT:PSS	DT-PDPP2T-TT:$PC_{61}BM$	Al	7.30	1.53	67.0	7.40	[109]
ITO/PEDOT:PSS	PBDTTPD:$PC_{71}BM$	ZnO/Al/MoO_3	PBDTTPD:$PC_{71}BM$	Ca/Al	6.54	1.84	54.47	8.35	[110]
ITO/PEDOT:PSS	PBDB-T:ITCC-M	ZnO/PCP-Na	PBDTTT-E-T:IEICO	PFN-Br/Al	12.00	1.80	63.9	13.80	[111]
ITO/PEDOT:PSS	PBDD4T-2F:$PC_{71}BM$	ZnO/PCP-Na	PBDTTT-E-T:IEICO-4F	PFN-Br/Al	11.51	1.71	65	12.80	[112]
ITO/PEDOT:PSS	PBD1:PC71BM	ZnO/n-PEDOT:PSS	PTB7-Th:IEICO-4F	ZnO/Al	12.30	1.61	72	14.20	[98]
ITO/PEDOT:PSS	J52-2F:IT-M	ZnO/PCP-Na	PTB7-Th:IEICO-4F	PFN-Br/Al	13.30	1.65	68.0	14.90	[113]
ITO/ZnO	PDCBT:$PC_{71}BM$	MoOx/Ag/ZnO	PBDT-TS1:$PC_{61}BM$	MoOx/Al	11.65	1.60	54.47	10.16	[114]
ITO/ZnO	P3TEA:SF-PDI_2	PEDOT:PSS/ZnO	P3TEA:SF-PDI_2	V_2O_5/Al	8.21	2.13	60.9	10.8	[96]
ITO/ZnO	PBDTTBO:$PC_{71}BM$	MoO3/PEDOT:PSS/ZrAcac	PDTP-DFBT:$PC_{71}BM$	MoOx/Al	11.60	1.49	58.7	10.10	[115]
ITO/ZnO	P3HT:ICBA	PEDOT:PSS/ZnO	PDTP-DFBT:$PC_{61}BM$	MoOx/Ag	10.10	1.53	68.5	10.60	[116]
ITO/ZnO	PBDB-T:Y1	MoO_3/PEDOT:PSS/ZnO	PBDB-T:Y1	MoO_3/Ag	11.2	1.71	73.6	14.1	[103]
ITO/ZnO	PTZ1:$PC_{71}BM$	MoOx/Ag/PFN	PBDTTT-C-T:$PC_{71}BM$	MoOx/Al	9.60	1.65	66.0	10.30	[117]

Bottom Electrode	**Front active layer**	**ICL**	**Back active layer**	**Top electrode**	**J_{SC} [$mAcm^{-2}$]**	**V_{OC} [V]**	**FF [%]**	**PCE [%]**	**Ref.**
ITO/ZnO	GEN-2:PC61BM	PEDOT:PSS/ZnO/PEI	PTB7-Th:PCBM	MoOx/Ag	8.45	1.55	76.6	10.03	[118]
ITO/ZnO	PBDTFBZS:$PC_{71}BM$	PEDOT:PSS/ZnO	PNDTDPP:$PC_{71}BM$	MoOx/Ag	9.10	1.59	65.0	9.40	[119]
ITO/ZnO	P3HT:ICBA	PEDOT:PSS/ZnO	PBDTT-DPP:$PC_{71}BM$	MoOx/Ag	8.26	1.56	66.8	8.62	[79]
ITO/ZnO	PBDB-T:ITIC	MoOx/Ag/PFN	PTB7-Th:4TIC	MoOx/Ag	10.62	1.65	71	12.62	[120]
ITO/ZnO	PBDB-T:IT-M	MoOx/mix-PEDOT:PSS/ZnO	PTB7-Th:FOIC:F8IC	MoOx/Ag	10.60	1.62	67.7	13.30	[121]
ITO/ZnO	PBDB-TF:PTIC	MoOx/Ag/ZnO/PFN-Br	PTB7-Th:IEICO-4F	MoOx/Ag	12.76	1.61	68	13.97	[122]
ITO/ZnO	P3TEA:FTTB-PDI_4	PEDOT:PSS/ZnO	PTB7-Th:IEICS-4F	MoO_3/Au	9.83	1.72	61	10.5	[99]
ITO/ZnO	P3HT:ICBA	PEDOT:PSS/ZnO	PBDTT-FDPP:$PC_{71}BM$	MoOx/Ag	8.60	1.57	61	8.30	[123]
ITO/ZnO	PM6:IT-4F	HxMoO3/PEDOT:PSS/ZnO	PTB7-Th:IEICO-4F	MoOx/Ag	12.90	1.53	76.0	15.03	[124]
ITO/ZnO	P3HT:ICBA	PEDOT/AgNWs/ZnO	PTB7-Th:$PC_{71}BM$	MoOx/Ag	11.01	1.48	61	9.90	[125]
ITO/ZnO	PIDTT-BT:$PC_{71}BM$	MoO_3/Ni/ZnO:PEOz	PBDB-T:IT-M	MoOx/Ag	12.86	1.61	68.3	14.05	[126]
ITO/ZnO	PIDT-PhanQ:$PC_{61}BM$	MoO_3/Ag/PFN	PTB7:PC61BM	MoOx/Ag	9.95	1.60	68	10.98	[127]
ITO/ZnO/PFN	P3HT:$SF(DPPB)_4$	MoO3/Ag/PFN	PTB7-Th:IEIC	MoO_3/Ag	8.28	1.97	52	8.48	[92]
ITO/PFN	PBDDAT-2F:$PC_{61}BM$	MoO_3/Ag/PFN	PDPP4T-2F:$PC_{71}BM$	MoO_3/Al	11.29	1.68	61.30	11.62	[91]
ITO/PFN	PTB7:$PC_{71}BM$	MoO3/Ag/PFN	PTB7-Th:$PC_{71}BM$	MoO_3/Ag	10.17	1.55	68.60	10.79	[95]
ITO/ZnO/PFN-Br	PBDB-T:F-M	M-PEDOT/ZnO	PBDB-T:NNBDT	MoOx/Ag	10.68	1.82	74.7	14.52	[102]
ITO/ZnO/PFN-Br	PBDB-T:F-M	m-PEDOT:PSS/ZnO	PTB7-Th:O6T-4F:$PC_{71}BM$	MoOx/Ag	14.35	1.64	69	17.36	[100]
ITO/ZnO/PFN-Br	D18:F-ThBr	M-PEDOT/ZnO/P4VP	PM6:CH1007:$PC_{71}BM$	MoOx/Ag	13.99	1.88	70.88	18.67	[105]
ITO/ZnO/PFN	P3HT:SF(DPPB)4	MoOx/Ag/PFN	PTB7-Th:IEIC	MoOx/Ag	8.28	1.97	52	8.48	[92]
ITO/CuSCN	DRETSBDT	ZnO/n-PEDOT:PSS	n-PEDOT:PSS	MoO_3/Al	10.30	1.68	64.3	11.47	[93]
ITO/SnO_2	PV2000:PCBM	PEDOT:PSS/Ag/SnO_2	PM6:Y6	MoO_3/Ag	12.94	1.61	73	15.2	[104]
ITO/SnOx	PCDTBT:$PC_{71}BM$	MoOx/SnOx	PDPP3T:$PC_{61}BM$	MoOx/Ag	9.1	1.468	60	8.0	[128]
ITO/PEIE	P3HT:$IC_{60}BA$	m-PEDOT:PSS/PEIE	PTTBDT-FTT:$PC_{71}BM$	MoO_3/Ag	8.31	1.57	66	8.42	[129]

ITO/PEIE	PSEHTT:ICBA	PEDOT:PSS/PEIE	PSBTBT:$PC_{71}BM$	MoOx/Ag	8.73	1.52	67.15	8.91	[130]
ITO/GO	PSEHTT:ICBA	TiO2/GO/PEDOT:PSS	PSBTBT:$PC_{71}BM$	ZnO/Al	8.68	1.65	68	8.60	[131]
ITO/TIPD	PBDTBDD:$PC_{70}BM$	MoO_3/Ag/PFN-Br	PTB7-Th:IEICO-4F	MoOx/Al	11.59	1.50	76.6	9.51	[132]
ITO/MoO3	DTDCPB:C_{70}	BPhen:C60/Ag/PEDOT:PSS	PCE10:BT-CIC	TmPyPB/Ag	13.3	1.59	71.0	15.0	[133]

2.3 Main Performance limitations in OTSCs and Their Prospects for Further Development

Tandem organic solar cells are designed to improve the performance of organic solar cells by reducing thermalization and transmission loss by making use of wide and low band gap active layers in the front and bottom sub cells respectively [134]. One of the major challenges is the processing issue of OTSCs, fabrication of one layer over the other could wash out the lower layer and this retard steps to it commerciality [134]. Due to this, solvent selection for the active layers sub cells and ICL of the tandem device is of great importance. Nonpolar organic solvents including chlorobenzene and dichlorobenzene have been widely used as the solvents for the bottom cells, whereas low boiling point solvents like chloroform and methylene chloride have been used for active layers of the top cells so as to maintain stability of the bottom cells [134]. Polar solvents: IPA, ethanol and water have been used for the solvents of the ICL since it has less tendency of dissolving active layer of the bottom cells [134]. In cases where high boiling point solvent is used for the top cell then a more robust ICL that is high solvent resistant is required to shield and guard the bottom cell from demolishing[134]. It is worth mentioning that the efficiency of the tandem device is dependent on the absorption spectra of the active layers of top and bottom cell. The top cell and bottom cells require wide and narrow band gap materials respectively. The spectrum of the sun that reaches the earth ranges from 100nm to over 1000 nm (i.e from UV to Infrared), and more than 50% of this radiation is made of IR. Hence, fabricating a solar cell that can absorb most of IR-spectrum is much needed. Initially, the front cell active

layers that were viewed as wide bandgap materials were based on fullerene polymers have absorption edge around 700nm and energy gaps close to 1.75 eV. With the introduction of Nonfullerene acceptors which have broad absorption spectrum up to 1100nm, therefore active layers that have absorption around 700nm (about energy gap of 1.7 eV or more) or even more can be used as the narrower band gap active layer for the bottom cell. This makes the definition of narrow band gap and absorption band gap relative since per the device structure one can used a narrow band gap of 1.50 eV. To fully absorb and create more efficient tandem devices utilizing more than 90% of the sun's radiation, research must still focus on developing narrow band gap materials that could absorb deep IR regions such as 1100nm or more.

As aforementioned mentioned the *PCE* depends on the V_{OC}, J_{SC} and *FF* which solely affects device performance. Optimizing the thickness of all the layers included in the tandem device must not be overlooked since it has a great impact on device performance and its commercialization. Increasing the thickness of the active layers of the sub cells increases the J_{SC} and the absorption spectra of the cells, however there is excessive decrease of the *FF* which in turns decreases the *PCE* drastically [135]. With the use of transfer optical modeling Zang et al. concluded that, there is an increased in defect states whenever there is an increased in active layer thickness which causes *FF* to reduce respectively. Charge recombination increases with increasing states defects and thereby limiting collection of charge carrier which in effect reduces the performances. The optimized thickness of active layers is mostly in the range of 90nm to 120nm.

Voltage loss of the individual cells is one of the major challenges of the OTSCs, though series connected tandem devices manages to improve the V_{OC} since the V_{OC} of the whole device is a total sum of the V_{OC} of the individual sub cells, which could outperform the SQ limit.

Though the V_{OC} of the individual sub cells are affected by weak energy transfer radiative and nonradiative recombination, but the ICL that used in series monolithic (2T) tandem devices also limits the V_{OC} of the whole device [136]. The ICL contributes to optical losses by absorbing light that should reach the sub cells and hence decreases the V_{OC}. As aforementioned, the ICL also acts as an intermediate electrode (common electrode) in parallel connected OTCSs and might be of the same polarity at its junction with the subcells. To meet such a design requirement an ICL that has low impedance (to reduce resistance), highly optically transparent and conductive is needed. Since these requirements are difficult to meet for the ICL parallel monolithic devices, series connected tandem devices should be of much focus in the future in other to attain high performance tandem devices as confirmed by previous research works in Table 1 and 2. The good addition the ICL of the series connected device does is that it can enhances the lossless recombination of electrons and holes from their corresponding sub-cells and in general can reduce or avoid completely V_{OC} losses in the TSCs. As mentioned previously, the J_{SC} of the series connected tandem devices is limited by the lowest J_{SC} of the sub cells, but current matching of the sub cells is another big challenge in fabrication tandem devices. Current matching of the device depends on the absorption properties of the active layers of the sub cells, this requires the critical analyzes of the thin film optics of the devices [137].Optimization of the *FF* of the tandem device could be very challenging, the FF of the top cell series connected tandem device limits the *FF* of the whole device as mentioned earlier. For parallel devices the FF is the average of *FF* the two sub cells [65].

CHAPTER THREE

3 OPTICAL TRANSFER MATRIX-BASED SIMULATION, GENERATION RATE, EXTRACTION EFFICIENCY AND SHORT CIRCUIT CURRENT.

3.1 Optical Transfer Matrix-Based Simulation of the Tandem Solar Cell

Achieving unrevealing optoelectronic properties of the tandem device can be incredibly challenging since the performance of the whole tandem device depends on both the top and bottom organic solar cells. The three main components of organic solar cells are, the active layer, band alignment layer (ETL and HTL) and electrodes [138].Transfer matrix simulation is used to model a tandem device structure with bulk heterojunction active layers and optimize it by varying the thickness of the active layers.

The transfer matrix method is a way of calculating how a physical system transforms an input state into an output state. Many use it to explore how wave-like patterns, such as those seen with light or in quantum mechanics, change when they pass through barriers or different surfaces. A transfer matrix is an arrangement of data in the form of a square matrix that connects the state of the system on one side of the interface to the state on the other side [139]. Creating the transfer matrix requires the use of the relevant mathematical operators on the state vector of the system, which depicts the amplitude and phase of the wave at every location. A variety of issues in physics and engineering can be solved using the transfer matrix technique, such as the spread of electromagnetic waves in optical apparatuses, the scattering of particles in quantum mechanics, and the dynamics of liquid movements in intricate shapes [139]. It offers a strong mathematical framework for analyzing and forecasting the behavior of complex physical systems.

Photovoltaic or solar cells are electronic devices that basically convert sunlight into electricity, hence light management in the device plays a crucial role in designing and manufacturing highly efficient solar cells. The photoactive material absorbs high energy photons equal greater than its band gap; charge carriers are then generated as result of excitation of electrons from lower energy level to higher energy level. The amount of charge carriers generated depends on the amount of light that reaches the photoactive absorber, which in turn determines the current density of the solar cell. The TMM describes the matrix connected to the amplitudes of the incident light and the transmitted light on both sides of the thin film structures [139].

In this simulation, the theoretical generation rate G(x) and short circuit current J_{SC} of the single and multi-junction of our solar cells structure have been investigated. The TMM simulation considers all the optical constants and thicknesses of the six layers, Glass/ITO/ETL/Active layer/HTL/electrode of the organic solar cell which are numerically computed. The amount of light that is reflected, transmitted, absorbed by each layer is calculated till it reaches the photoactive layer which then generates the charge carriers depending on the material properties. The transmitted light through the cell can be calculated, and in the case of tandem solar cells, this transmitted light through the first cell becomes an incident light for the bottom cell and the same process continues. The simulations have been carried out by using the Python software.

Finite Difference Time Domain and Transfer Matrix method have been the most common numerical methods used in the investigation of the behavior of incident light through complex solar cells or waveguide structures [139–141]. We implement the TMM to correctly calculate the optical electric field amplitude and create a vivid graphical representation of our results.

3.2 Sunlight

In the photovoltaic industry one major factor is the availability of sunlight. The spectral distribution of sunlight determines the generation rate and how much electrical current can be produced by the photovoltaic cell. The specific portion of light that can be absorbed by the top and bottom cell of the organic tandem device depends on the unique band gap features each active layer. For efficient current collection of a tandem solar cell, the absorption spectrum active layers of the top and bottom cell should be in the high intensity and low intensity of the solar spectrum. Therefore, for the advancement and design of photovoltaic devices, terrestrial solar spectrum data is needed. Time of the day, atmospheric condition, and angle at which the sun rays reach the ground determine the solar spectral irradiance, therefore a standard representation showing the distribution of the spectral solar irradiance is required [142]. The American Society for Testing (ASTM) has developed different irradiance standards; AM 1, AM 1.5, AM 2, etc. for this reason [142]. The airmass, AM 1.5, represents the amount of atmosphere the light has passed through to reach the surface of the earth at angle of 37° [143]. For countries such as Kazakhstan with geographical location of 48° latitude AM 1.5 is the best standard spectral solar irradiance to use. The AM 1.5 solar irradiance spectrum used in this work is shown in Figure 3.1.

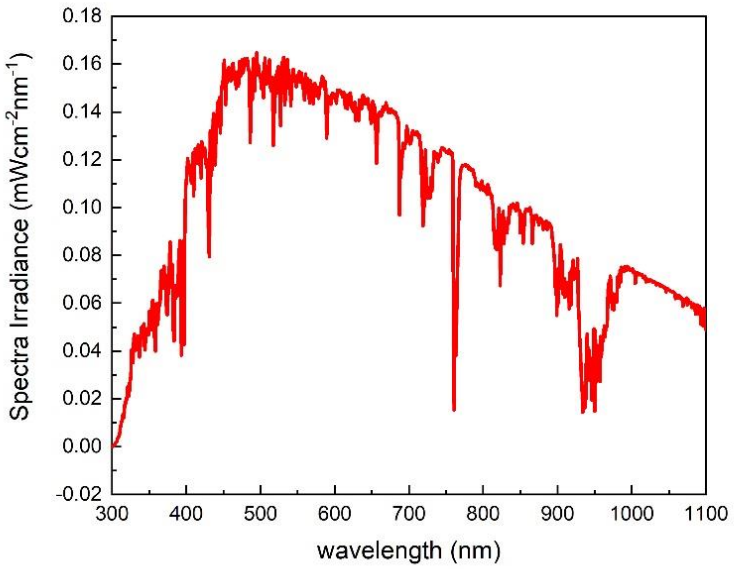

Figure 3.1:Standard AM 1.5 solar irradiance spectrum *[142,143]*.

3.3 Charge generation

The transparent electrode ITO allows light to pass through and strike the organic material (photoactive layer). ITO has a low reflection coefficient; most of the light transmits through it and then incidents on the subsequent layers. Excitons are produced when light interacts with the photoactive layer; these excitons diffuse through the active layer and split into free charges, electrons, and holes when they reach the donor/acceptor interface. The electrons and holes diffuse through the bulk heterojunction active layer to the anode and cathode respectively due to a built-in electric field caused by the difference in work functions of the electrodes, in our case Ag, and ITO, producing photocurrent. The bulk heterojunction consists of interpenetrating networks of the donor and acceptor components, creating a very large interface and makes the excitons very close to this interface –This large interface and its proximity to the exciton accommodates the short diffusion length of the excitons, and hence more electrons and holes have clear path to get to the cathode and anode respectively [144,145]. The electron transport

layer ETL serves as hole blocking layer whereas hole transport layer serves as the electron block layer, also these transport layers serve as good band alignment for the charge carries to reach the electrodes. Since excitons are short lived particles, they need to reach the donor acceptor interface before they decay. Therefore, the thickness of the photoactive layer needs to be well chosen considering the exciton diffusion length and for efficient charge carrier generation rate.

Though bandgap of the photoactive materials is another limiting factor of the photocurrent generation. Exciton is generated only if the photoactive material is excited by photons of energy higher than its band gap. The available wavelengths are set by the solar spectrum: therefore, appropriate materials must be chosen to increase the probability of exciton generation.

3.4 Generation rate $G(x)$, charge carrier extraction probability η and short circuit current density J_{SC} of tandem devices

The tandem devices considered in this research were series connected and hence current matching of the sub-cells is important, the sub-cell with the least J_{SC} limits the total J_{SC} of the whole device. Whereas the V_{OC} of the whole tandem device is the sum of the V_{OC} of the individual sub-cells, and the FF of the top cell directly affects the FF of the tandem device though they are not numerically equal. The Performance of a solar cell is described by the power conversion efficiency (PCE) of the device which is given as[146–148]:

$$PCE = \frac{V_{OC} \times J_{SC} \times FF}{P_{int}} \tag{3.1}$$

Where the P_{int} represents the input power intensity. Also, the thickness of each layer of the cell affects the performance of the cell. Defects states in the active layer increases with increasing thickness of the active layer, this in turn increases carrier recombination rate and thereby decreasing generation rate of the cell [149–152]. Therefore, to achieve highly efficient single

junction or tandem device, transfer matrix simulation is deployed to calculate the ideal theoretical performance parameters and ideal optoelectronic properties.

When light hits the cell, photons are absorbed by the donor material, creating excited states called excitons. For the solar cell to generate electrical power, these excitons must be separated into positive and negative charges, which can then be extracted from the device. The extraction process of these photogenerated charge carriers involves several steps. First, the excitons must diffuse through the donor material until they reach the donor-acceptor interface. Once at the interface, the excitons dissociate into free electrons and holes, which are then transferred to the respective electrodes (usually made of transparent conductive oxide and metal).

3.4.1 Generation rate G(x)

Generation rate is an important parameter of a solar cell that depends greatly on optical constants of the materials involved in the device architecture and the light intensity. Generation rate is the number of charge carriers that are generated per one second in one cubic meter of the active layer [153]. The $G(x, \lambda)$ is influenced by the depth of the active layer (x) and the intensity of the incident photon (proportional to λ).

The numerical simulation that were conducted based on all the devices were based on; three main equations: Poison equation (Eq 3.2), carrier continuity equation (Eq 3.3), and drift-diffusion equation (3.4) as follows [154,155]:

$$\frac{\partial^2 \varphi}{\partial x^2} = \frac{q}{\varepsilon}(n - p) \tag{3.2}$$

$$\frac{\partial n}{\partial t} = \frac{1}{q}\frac{\partial J_n}{\partial x} + G - R \frac{\partial p}{\partial x} = -\frac{1}{q}\frac{\partial J_p}{\partial x} + G - R \tag{3.3}$$

$$J_n = qD_n \frac{\partial_n}{\partial x} - q\mu_n \frac{\partial_p}{\partial x} J_P = -qD_P \frac{\partial_n}{\partial x} - q\mu_p \frac{\partial_\varphi}{\partial x} \tag{3.4}$$

Where φ is the electric potential, q is the electron charge, ε is the dielectric constant, n is the electron concentration, p is the hole concentration, J_n is the electron current density, J_p is the hole current density, D_n is the electron diffusion coefficient, D_p is the hole diffusion coefficient, μ_n is the electron mobility, μ_p is the hole mobility, G is the carrier generation rate, and R is the carrier recombination rate. Shockley-Read-Hall (SRH), band-to-band, and Auger recombination were considered under the recombination rate. The optical electric field is obtained as $|E(x)|^2$, this is electric field that TMM simulation calculates using the optical constants of the all the layers of the model device. Hence from equation 3.5 and equation 3.6 the charge carrier generation rate can be derived as [154]:

$$Q(x,\lambda) = \frac{2\pi c \varepsilon_o kn|E(x)|^2}{\lambda} \tag{3.5}$$

$$G(x) = \int_{\lambda_i}^{\lambda_f} \frac{\lambda}{hc} Q(x,\lambda) d\lambda \tag{3.6}$$

In this case, ε_o is the vacuum permittivity, c is the speed of light, k is the imaginary part of the refractive index, n is the real part of the refractive index, h is plank constant and λ is the wavelength.

3.4.2 Charge Carrier Extraction Probability η

Extraction of photogenerated carriers is critical for determining cell efficiency. Charge carrier extraction can be defined as the process of separating these electron-hole pairs and extracting the charges as electrical current [156,157]. This is accomplished in a solar cell by creating a built-in electric field within the semiconductor material, which causes electrons and holes to be separated and move towards opposing cell contacts [158,159]. The negative contact

(cathode) collects electrons, while the positive contact collects holes (anode). The flow of electrons from the negative to positive contact produces the electrical current that can be used to power devices. It is critical to maximize the efficiency of a solar cell, making sure the charge carrier extraction process is as effective as feasible is crucial [160]. One major hindrance to carrier extraction is carrier recombination. To decrease charge carrier recombination and increase collection efficiency, this entails improving the material properties, device structure, and electrode design.

However, several variables, including the energy levels and mobility of the charge carriers, the morphology of the donor-acceptor interface, and the caliber of the electrodes, affect the extraction of the generated charge carriers. High power conversion efficiency in organic solar cells requires effective charge carrier extraction. The active layer's shape can be changed by combining the materials used for the donor and acceptor layers to form bulk heterojunctions, which can increase the efficiency of charge carrier extraction or adding effective interfacial layers to improve carrier charge transport [161]. The process of extracting charge carriers can also be improved by optimizing the electrodes and the design of the entire device [161–163].

Charge carrier extraction probability η is one of the important figures of merit (FOM) that plays a fundamental role in describing efficiency of the OSCs. The spatial dependent extraction probability is the sum of the individual extraction probability of electrons $\eta_n(x)$ and holes $\eta_p(x)$ as composed in equations 3.8-3.10 (Hetch equations) [153,164]. Here x represents the position in the active layer with respect to the extraction probability, that is $x = 0$ indicates the position at the interface of the active layer and the front electrode [164]. For this purpose, the main influence of the charge carrier extraction probabilities are the thickness of the active layer L and the mean free path w. As aforementioned, the total extraction probability is given as [164]:

$$\eta(x) = \eta_n(x) + \eta_p(x) \tag{3.7}$$

Where the individual extraction probabilities are expressed as [164]:

$$\eta_n(x) = \frac{w}{L}\left[1 - \exp\left(\frac{-L - x}{w}\right)\right] \tag{3.8}$$

$$\eta_p(x) = \frac{w}{L}\left[1 - \exp\left(\frac{-x}{w}\right)\right] \tag{3.9}$$

The mean free path *w* describes the average distance the charge carriers can travel. It depends solely on effective carrier mobility μ which tells how fast the photogenerated charges can travel; recombination lifetime τ which quantifies the time taken for recombination processes to take place; built in voltage V_{bi}; and the thickness of the active layer. It is mathematically given as [164]:

$$w = \frac{\mu\tau V_{bi}}{L} \tag{3.10}$$

Germinate and non-germinate recombination are the two main recombination mechanisms that affect carrier extraction of organic solar cells. Germinate recombination is the result exciton-charge annihilation whereas the non-germinate recombination is characterized by two processes: bimolecular and trap-assisted recombination. Band-to-band recombination process is what we termed as the bimolecular recombination, and it is an inevitable/fundamental recombination process in organic solar cells. Factors such as impurities, tiny pores created by deposition of metal electrodes, water-oxygen complexes and water clusters create localized sub-gap states within the bang gap causing trap-assisted recombination [165–167]. However, the trap assisted recombination can further be grouped in two different categories: bulk trap-assisted and surface trap-assisted recombination process. Bulk trap-assisted states are created in the bulk active layer whiles surface trap-assisted states are created at the electrode/active layer interface surface [164]. Charge carrier's lifetime is inversely related to the bimolecular k_{bm}, bulk trap-

assisted k_{bulk} and surface trap-assisted k_{sf} recombination coefficients which is given as [164,168]:

$$\tau = \frac{1}{k_{bm}+k_{bulk}+k_{sf}n_{Jsc}} \tag{3.11}$$

Where n_{Jsc} denotes charge carrier density under short circuit conditions, and the non-germinate recombination coefficients are formulated as [164]:

$$k_{bm} = \frac{2q\mu_{eff}}{\varepsilon\varepsilon_0} \tag{3.12}$$

$$k_{bulk} = \frac{q\mu_{eff}N_{bulk}}{\varepsilon\varepsilon_0} \tag{3.13}$$

$$k_{sf} = \frac{q\mu_{eff}N_{surf}}{L\varepsilon\varepsilon_0} e^{-q\frac{V_{bi}-V_{OC}}{k_BT}} \tag{3.14}$$

And where q is elementary charge, ε is the static dielectric constant, ε_0 is permittivity, μ_{eff} is effective mobility of the blend, N_{bulk} is density of bulktraps, N_{surf} density of surface traps, and k_B is Boltzmann constant. It may be not that, bimolecular (radiative) recombination is assumed to be dominant recombination process in BHJ solar cells just like in inorganic solar cells [169,170].

3.4.3 Short Circuit Current, J_{SC}

In simply put, the short circuit current density (*Jsc*) measures a solar cell's ability to generate current when exposed to sunlight under short circuit conditions. When a cell is short circuited, the voltage across the cell is zero, so the entire current flowing through the cell is shorted. It is commonly expressed in units of amperes per square centimeter (A/cm^2). The short circuit current density of a solar cell represents its maximum capacity to produce current when no external load is connected to it. *Jsc* is an important parameter for assessing the performance of a solar cell, since it indicates the amount of current the cell can generate under ideal

conditions. In general, the higher the *Jsc*, the more efficient the solar cell is at converting sunlight to electricity. In line with equation 3.6 the J_{SC} is calculated in equation 3.15 as [164]:

$$\mathrm{J_{SC}} = \mathrm{q} \cdot P_g \int_{\lambda_i}^{\lambda_f} \int_{x_0}^{x_f} G(x)\eta(x)dxd\lambda \tag{3.15}$$

Where P_g is geminate recombination prefactor and this equation shows a clear linear dependance of current density J_{SC} on generation rate G(x), optical electric field intensity, recombination prefactor, depth of the active layer and extraction efficiency of the organic blend material. Most of these parameters are material properties of the photoactive layer, therefore, to increase the optoelectronic properties of the material we can adjust the active layer thickness till we achieve an optimized level. This idea of the optimization of the thickness of the active layers is implemented in this simulation.

Table 3.1 shows all the parameters that were used in the modeling and deduction of the generation rate, extraction efficiency and short circuit current of our devices used in this simulation. The band gap E_g and the built-in voltage V_{bi} of the organic material were determined experimentally whereas the rest of the parameters were obtained from literature [164].

Table 3.1: Device parameters based on the study of the reported PM6:o-IDTBR and PM2:COTIC-4F used in this simulation *[164]*.

Parameters	**Value**
Bandgap E_g of PM6:o-IDTBR	1.75 eV
Bandgap E_g of PM2:COTIC-4F	1.10 eV
Permittivity of free space	1×10^{-2}
Dielectric constant ε	3
Effective density of states N_C	2.5×10^{19} cm^{-3}
Density of bulk traps $N_{t.bulk}$	10×10^{15} cm^{-3}
Density of surface traps $N_{t.surf}$	10^{12} cm^{-3}
Geminate recombination prefactor P_g	0.95
Effective mobility μ_{eff} of PM6:o-IDTBR	5×10^{-5} $cm^2V^{-1}s^{-1}$
Effective mobility μ_{eff} of PM2:COTIC-4F	5×10^{-5} $cm^2V^{-1}s^{-1}$
Temperature T	298 K
Built-in voltage V_{bi} PM6:o-IDTBR	1.14 V
Built-in voltage V_{bi} PM2:COTIC-4F	0.78 V
Langevin prefactor for bimolecular recombination χ	0.005

CHAPTER FOUR

4 RESULTS AND DISCUSSIONS

4.1 Optical constants of all the layers of the organic tandem solar cells.

The amount of solar irradiance that is reflected, transmitted, and absorbed by the organic tandem solar cells depends solely on the optical constants, refractive index n(λ) and extinction coefficient k(λ) of each layer involved. The values of the optical properties: refractive index n(λ), which dictates the portion of light transmitted or reflected at the interface of each layer; and the extinction coefficient k(λ), which determines the kind of wavelength that will be absorbed at each layer in the tandem architecture are determined [153]. Also, the thickness of each layer affects the transmitted light intensity since it contributes to the attenuation of the transmitted light. The design of the device architecture and these optical properties determines exciton generation G(x,λ) rate of the active layers [153].

To begin with, the experimental procedure followed three steps: material preparation, spin coating of active layers and the measurements of the optical constants with the use of UV-Nis NIR spectrometer. The WBG photoactive layer PM6:o-IDTBR was synthesized by missing the donor material PM6 with the non-fullerene acceptor in the ratio of 1:1 in a viar (small glass bottle) with the help of chlorobenzene (CB) and Diiodoethane (DIO) as solvents. In the same way the NBG photoactive absorber PM2:COTIC-4F was also synthesized by missing the donor material PM2 with the non-fullerene acceptor COTIC-4F in the ratio 1:1.5 respectively in a viar using CB and DIO as solvents. These solvents addition was done in a glove box to protect the chemicals from air and water (or oxygen). These samples were placed on a heater at a temperature of 53 °C and with the help of magnetic bars the chemicals were stirred at a spin speed of 120 rpm for 12hrs.

The glass substrates were cleaned with soap plus deionized water (DIW), acetone, and isopropanol each for 15 mins. The substrates were dried with nitrogen air and annealed at 90 °C for 15mins, and it further undergone UV ozone treatment for 15 minutes. These glass substrates were transferred into the glove box. The photoactive absorbers were spin coated on the glass substrates at constant volume of 35 µL at different spin speed of 1000, 1500 and 2000 rpm.

With the use of the UV-Nis NIR spectrometer the transmittance and reflectance spectra of the photoactive layer was measured as shown in figure 4.1.

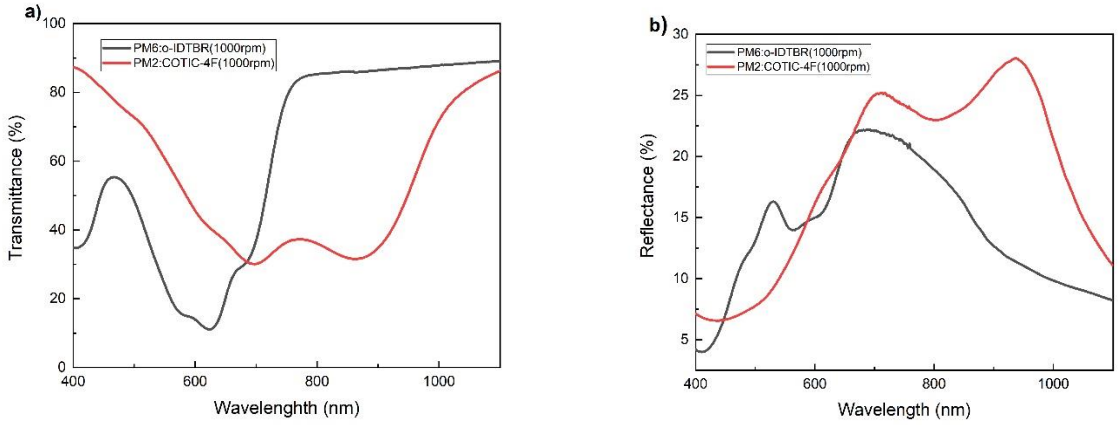

Figure 4.1 : (a) Transmittance and (b) reflectance spectra of PM6:o-IDTBR and PM2:COTIC-4F.

The thickness of the photoactive absorbers was measured, and it was observed that for the PM6:o-IDTBR the spin speed of 1000rpm generated a thickness of 100nm and for the PM2: COTIC-4F at 1000rpm we had a thickness 47nm. We had different other thickness with the other spin coating speed, but this thickness reported are the ideal thickness generated by the TMM simulation. With these obtained transmission and reflectance values, the corresponding refractive index n(λ) and extinction coefficient (λ) of each layer well calculated according to following equations [153]:

$$n = \frac{1+\sqrt{R}}{1-\sqrt{R}} \tag{4.1}$$

$$\alpha = \frac{1}{d}\ln\left[\frac{(1-R)^2}{2T} + \sqrt{\frac{(1-R)^4}{4T^2} + R^2}\right] \tag{4.2}$$

$$k = \frac{\lambda\alpha}{4\pi} \tag{4.3}$$

Where α is absorption, n is refractive index, k is extinction coefficient, R is reflection and T is transmission. The n and k of these photoactive layers were plotted based on these calculated values as shown in Figure 4.2.

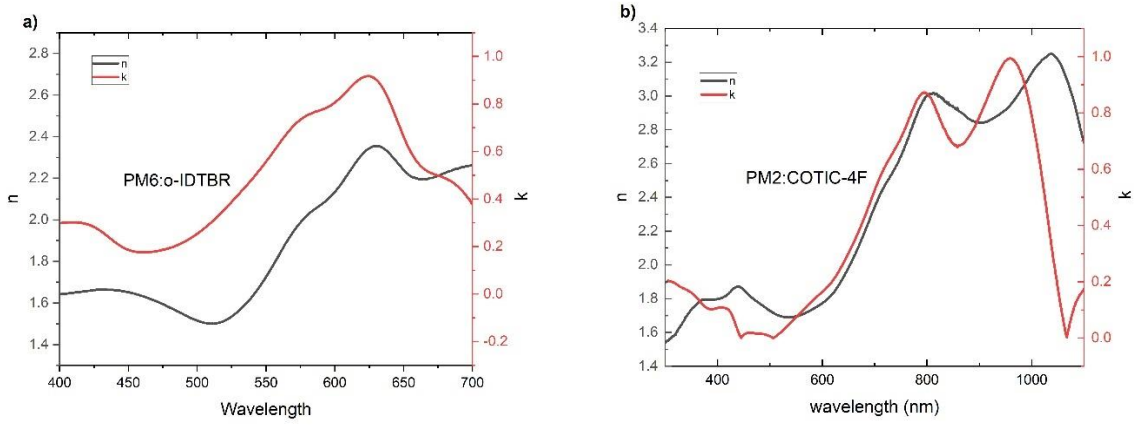

Figure 4.2:Refractive index and extinction coefficient of (a) PM6:o-IDTBR and (b) PM2:COTIC-4F.

The refractive index of both wide and narrow band gap organic active layers are in the range of 1.5 – 3.2 which is close to the general assumption that maximum n values of most organic semiconductors is ≈ 2 [153]. The refractive index of all the other layers involved in this work

ranges from 0 - 2.6 from ultraviolet (UV) to infrared (IR) spectrum, which is good reducing the attenuation of transmission light before reaching the active layers. The highest extinction coefficient ≈ 0.8 of PM6:o-IDTBR peaks around 624 nm, and it broadens in the visible spectrum contributing to less transparency of the tandem cell. And that of PM2:COTIC-4F with k ≈ 1 occurring around 960 nm, this high absorption in the IR-region is due the NFA COTIC-4F confirming it ultra-narrow band gap properties [171].

From the absorption coefficient values obtained from equation 4.2 with the experimental values of the reflection, transmission and the thickness, the spectra od the photoactive layers was plotted as shown in figure 4.3.

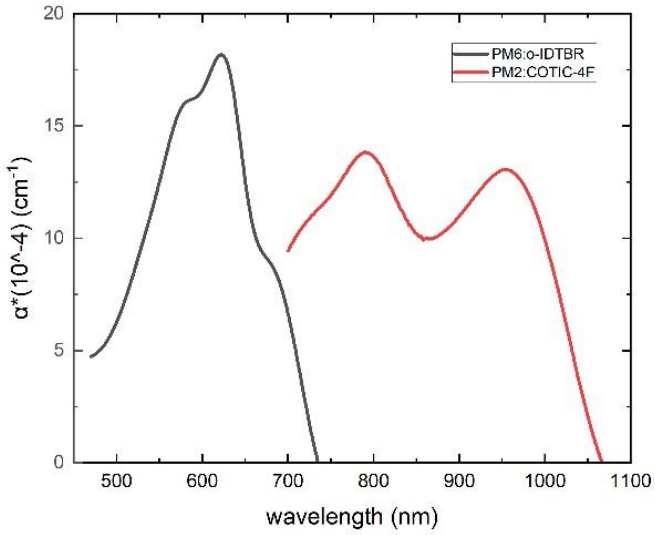

Figure 4.3:Absorption coefficient of PM6:o-IDTBR and PM2:COTIC-4F.

The top and bottom subcells of the tandem device should harvest different light spectrums and for this purpose we expect the selected organic active layers to show high absorption at low and high intensities of the light respectively. Figure 4.3 shows the absorption spectrum of the PM6:o-IDTBR and PM2:COTIC-4F. The WBG PM6:o-IDTBR harvest light in the visible spectrum

whereas the PM2:COTIC-4F harvest NIR spectrum. This is a clear indication of active layers for a tandem solar cell.

It must be noted that, except the optical constant of the photoactive absorbers PM6:o-ITDBR and PM2:COTIC-4F, the optical constants of the other layers used in this work were obtained from literature**.** From the device structure that was considered, glass is used as the substrate for both the top and bottom cell. The *n* and *k* values of the glass is shown in Figure 4.4, It is observed that the n values from the ultraviolet (UV) to the Infrared region lies within 1.5-1.54 which is very ideal for high transparency, and it could also be seen from the extremely low k values indicating less light absorption in that layer.

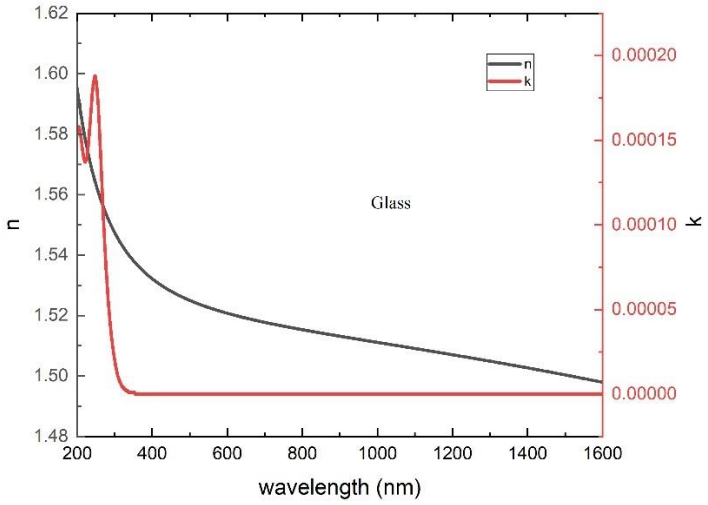

Figure 4.4: Refractive index and extinction coefficient of the glass.

The *n* and *k* values of the metal oxides such as ITO which serves as the cathode electrode and lies on top of the glass, followed by the ZnO which serves as ETL and the MoO_X which lies on top of the active layers are shown in figure 4.5. The *n* values of the ITO decrease with increasing wavelength, and it has very weak absorption properties. The ZnO also have weak absorption

properties but have *n* almost the same as the glass. Among the metal oxides, MoO_X have the highest n and k values, and this is a high indication that intensity of the light from 400-1100nm would be reduced at this layer. However, these are standard optical constants of metal oxides which will help us to calculate near accurate theoretical results.

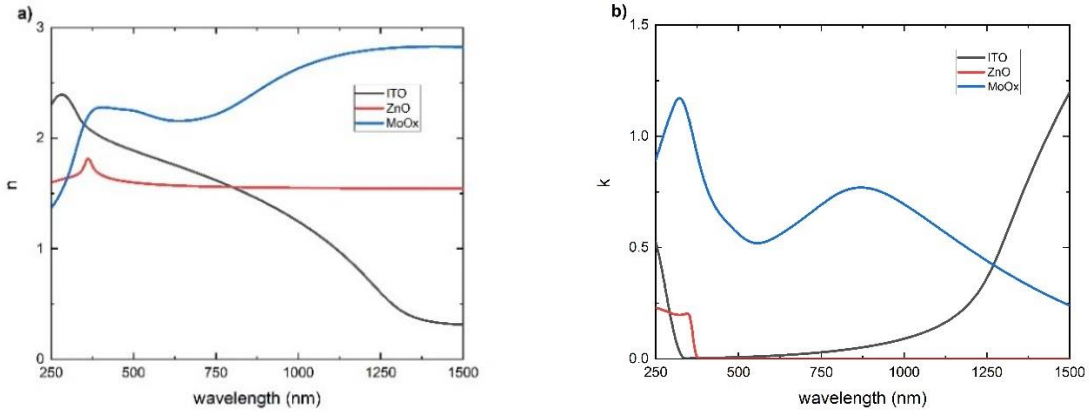

Figure 4.5: (a) Refractive index and (b) extinction coefficient of the metal oxides.

The back contacts electrode that was used in this simulation are Ag and Al. Figure 4.6 shows the n and k values of these two electrodes. Transparency and absorption have been one of the main issues of back electrodes, they are mostly opaque. Though Ag has very low n values, it has extremely high absorption coefficient just like Al. This makes fabrication of 4T tandem solar cells difficult, the back electrode of the top cell blocks much of the light from reaching to bottom cell due to its high absorption properties.

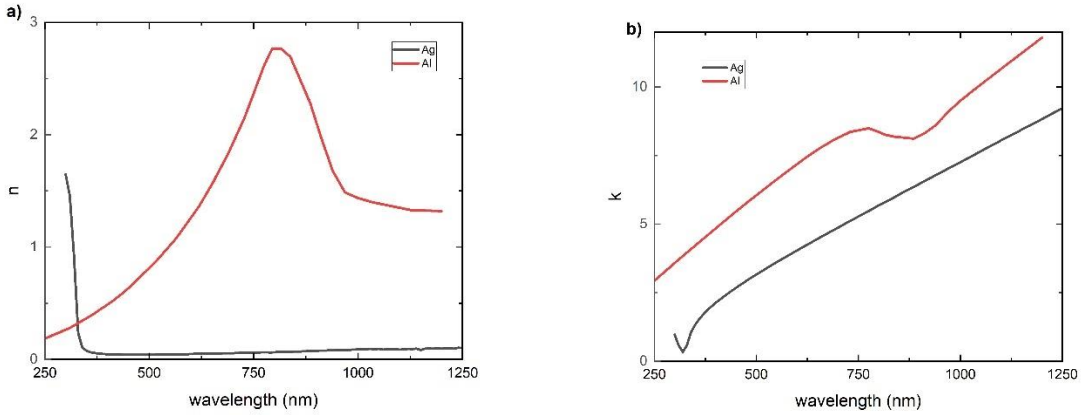

Figure 4.6: (a) Refractive index and (b) extinction coefficient of Silver (Ag) and Aluminum (Al).

4.2 Illumination of individual single junction devices under 1 Sun

To theoretically determine the G(x) and J_{SC} of the tandem device, first, we make use of the optical transfer matrix-based software we simulate the G(x) and J_{SC} of the individual devices involved in the tandem architecture separately from the obtained optical constants under the illumination of 100 $mWcm^{-2}$ AM 1.5 G (1 Sun) as shown in Figure 4.7 .The spectra irradiance (F), that is the power density at a particular wavelength of 1 Sun used in this simulation is shown in Figure 2.1.

4.2.1 Illumination of first device: Ultra NBG device Glass/ITO/ZnO/PM2:COTIC-4F/MoOx/Ag

In the first single junction device, we simulate our model device that make use of bulk heterojunction NBG photoactive absorber PM2:COTIC-4F with an inverted architecture deploying ITO as the top electrode and ZnO as ETL for efficient band alignment; the back metallic electrode, cathode we employ Ag and MoOx as the HTL as shown Figure 4.7. With an optimized thickness of each single layer involved, most importantly the optimized thickness of the photoactive layer PM2:COTIC-4F, 50nm.

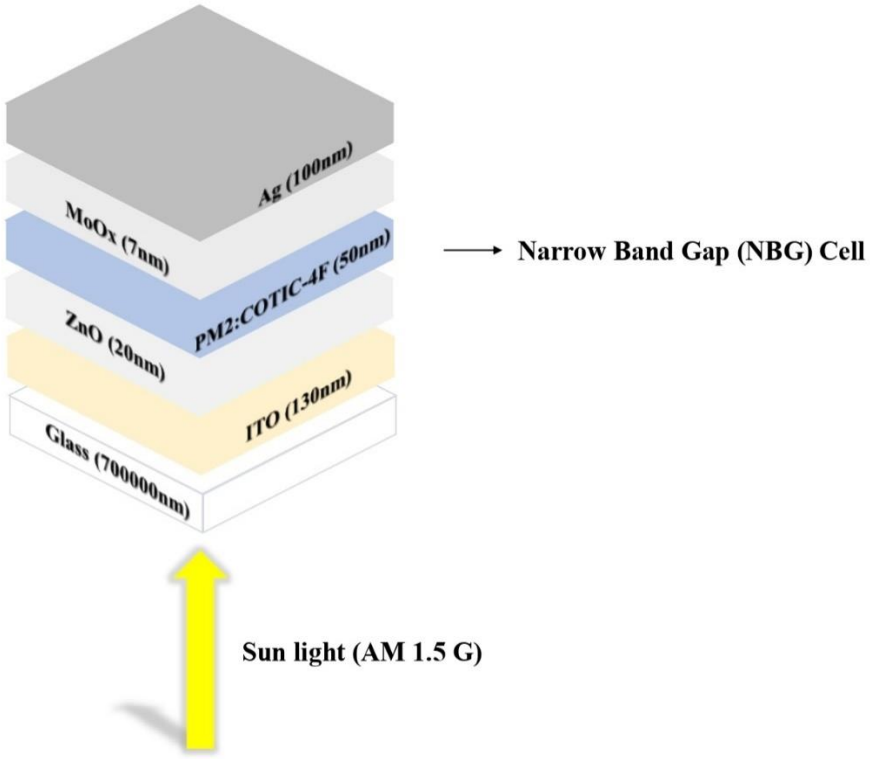

Figure 4.7: Schematic representation of single junction narrow bandgap cell.

We observed that as light is first incident on the highly transparent glass substrate as shown in Figure 4.8, most of the light is transmitted through to the efficient transparent ITO and the ETL ZnO. High fraction of light that reaches the PM2:COTIC-4F is absorbed by the from 700 -1050nm indicating how ultra-narrow the band gap of this organic compound is.

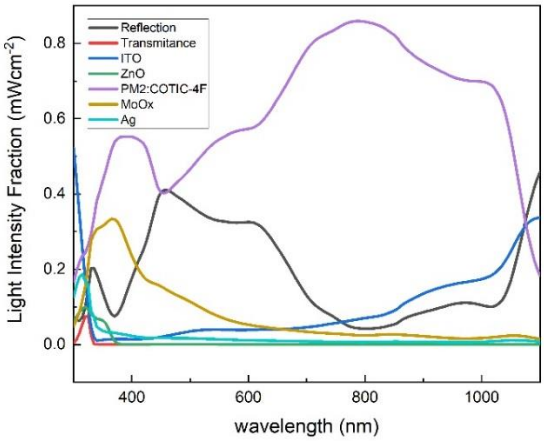

Figure 4.8: Light Absorption of all the layers involved in the device architecture of PM2:COTIC-4F.

It is worth knowing that for organic solar cells, charge carriers are only generated in the photoactive layer. Figure 4.9 shows the generation rate at each instant in the device, it is clearly seen that the charge carrier generation started right at the surface of the photoactive layer, PM2:COTIC-4F. The generation rate started to decrease as the light travels through the PM2:COTIC-4F and stopped at the bottom of the material, and no carriers were generated afterwards.

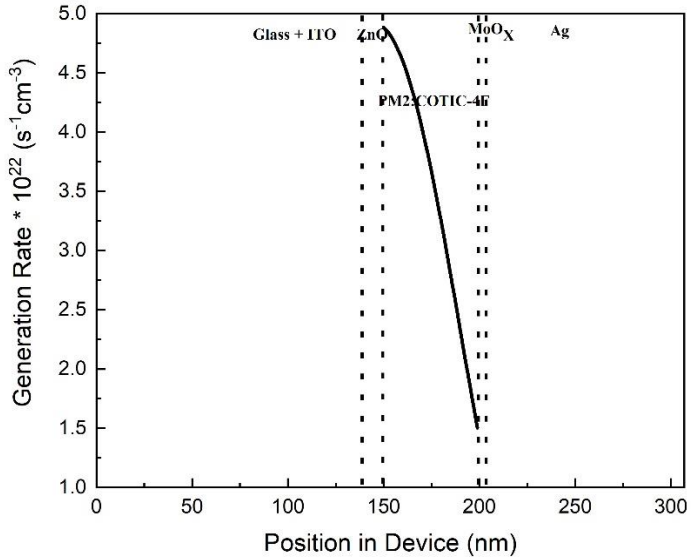

Figure 4.9*:* Generation at each position in the NBG single junction device.

The generation rate G(x) of the whole device is 17.59 x10^{23} $cm^{-3}s^{-1}$, it peaks at the surface of the active layer (PM2:COTIC-4F) and start to decrease as the depth of the material increases, this is as a result of the decrease of the photon intensity as it moves across the material as shown in figure 4.10 (a&b). The major contributing light intensity to the generation rate is from 650 - 1000nm, less carries are generated beyond this light boundary and at around 800nm the generation rate is at its maximum. At a critical look at the thickness of the photoactive material and generation rate, charge carriers are highly generated from the surface to some few nanometers, 25nm. Beyond 25nm to 50nm the G(x) decreased immensely. Therefore, a further increase of the thickness of the active layer beyond 50nm will yield no efficient generation rate. Fig 4.10b delineates perfectly how the generation rate are distributed withing the thickness of the photoactive material.

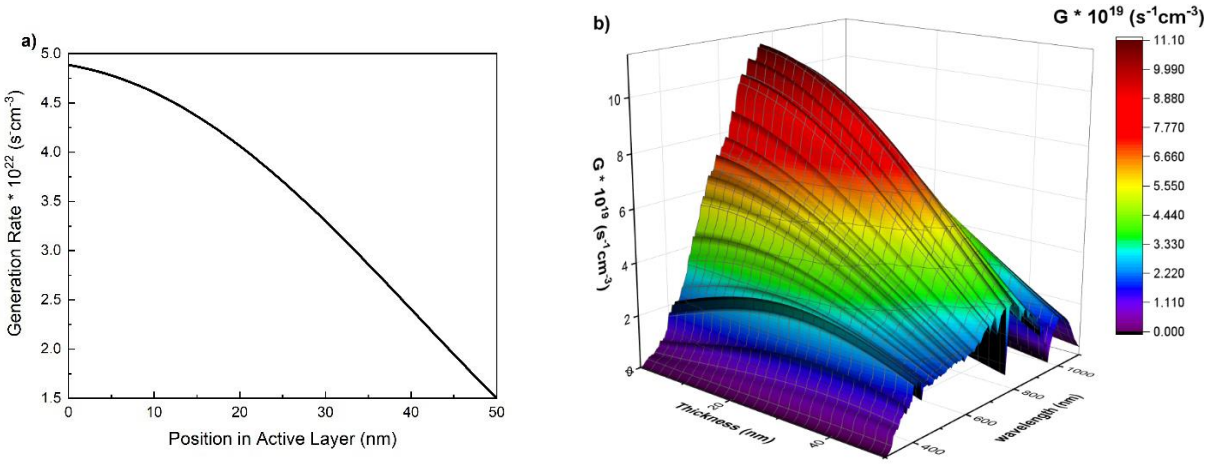

Figure 4.10: (a)Position of generation rate in active layer (b) 3-dimensional view of the generation rate versus its thickness of active layer and wavelength of the NBG single junction device.

Electrons and holes are the main source of charge carriers, efficient extraction of these generated carriers would lead to high yield of generation rate. The extraction efficiency of electron and holes are ≈ 0.8 whereas the total extraction efficiency of both charge carries is ≈ 0.9 which is extremely high as shown in figure 4.11. That is about 90% of the charge carriers that are generated would be extracted and losing the other 10% to recombination effects.

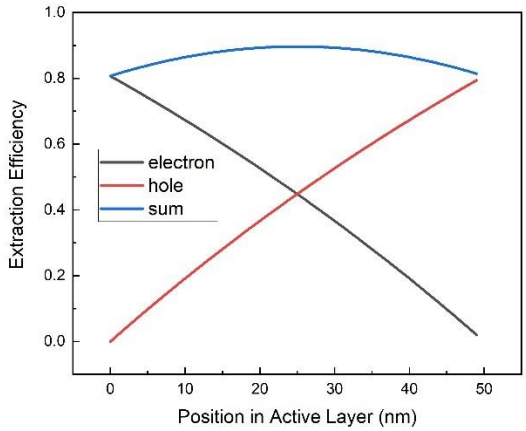

Figure 4.11: Extraction efficiency of electrons and holes of NBG PM2:COTIC-4F.

The Figure 4.12 shows the J_{SC} for a given depth of the active layer. It must be worth mentioning that this figure does not delineate how the J_{SC} behaves across the active layer, but it shows the J_{SC} that can be produced for a given thickness. For a 50nm depth of the PM2:COTIC-4F and based on the optical constants of all the layers included in the design architecture, the device yielded the highest possible J_{SC} of 28.189 $mAcm^{-2}$. Therefore, such a high J_{SC} indicates that the device is efficient in converting incident low energy sunlight to electrical power.

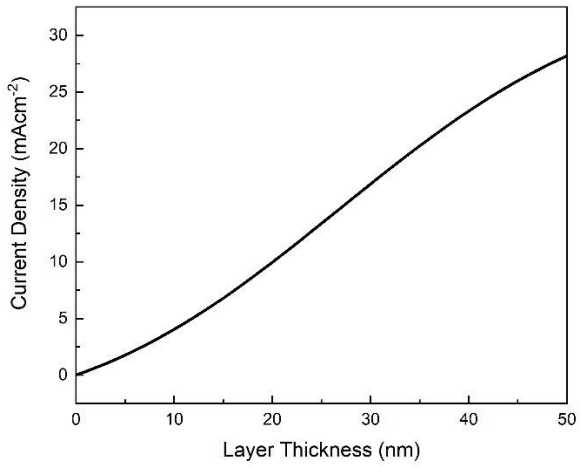

Figure 4.12: Current density for a given thickness of the PM2:COTIC-4F.

4.2.2 Illumination of second device: WBG device Glass/ITO/ZnO/PM6:o-IDTBR/MoOx/Ag

For the second single junction device, we simulate our model device that make use of bulk heterojunction WBG photoactive absorber PM6:o-IDTBR with an inverted architecture deploying ITO as the top electrode and ZnO as ETL for efficient band alignment; the back electrode, cathode we employ Ag and MoOx as the HTL. We optimized the thickness of each single layer involved, most importantly the optimized thickness of the photoactive layer PM6:o-IDTBR is 100nm as shown Figure 4.13.

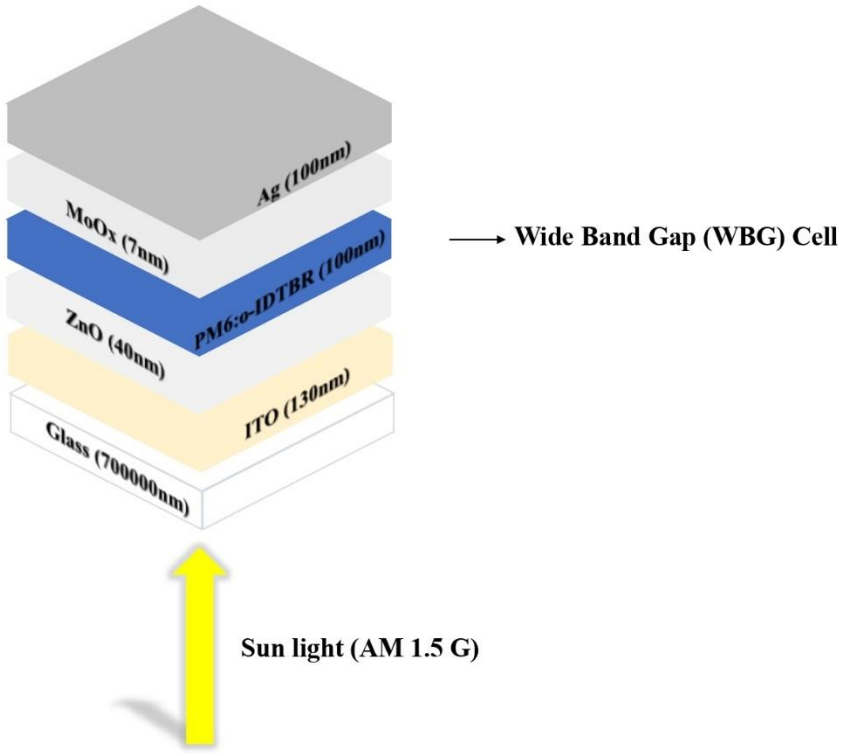

Figure 4.13: Schematic representation of single junction wide bandgap cell.

We observed that as light is first incident on the highly transparent glass substrate, most of the light is transmitted through to the efficient transparent ITO and the ETL ZnO as shown in Figure 4.14. High fraction of light that reaches the PM6:o-IDTBR is absorbed within the range of 300 -740nm indicating high wide bandgap absorption properties of this organic compound is.

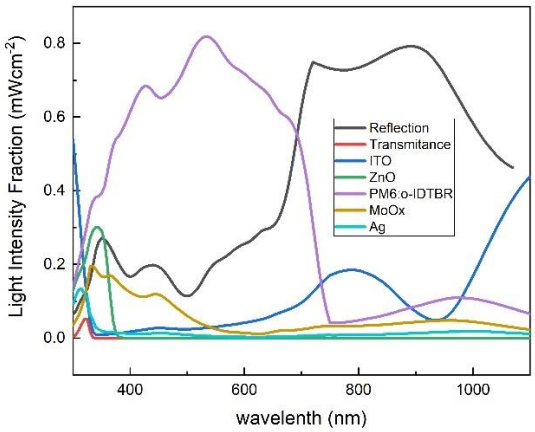

Figure 4.14: Light Absorption of all the layers involved in the device architecture of PM6:o-IDTBR.

Figure 4.15 shows the position of the generation rate at each layer in the whole device. It is interesting to note that the G(x) peaks in the middle of the device and decreases at the surface and bottom of the PM6:o-IDTBR active layer. Again, we see that charge carrier generation only happens in the photoactive absorber.

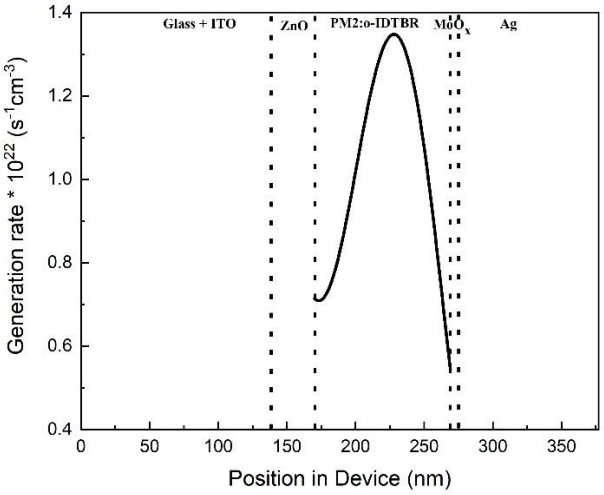

Figure 4.15: Generation at each position in the WBG single junction device.

From the beginning of the surface of the active layer, the G(x) values were low, but as it gets into the middle of the device from 40nm to 80nm the G(x) increased abruptly as shown Figure 4.16a. For this reason, the thickness of the PM6:o-IDTBR should not be below 100nm for efficient charge carrier generation. This is one of the reasons why the thickness of the WBG device is twice higher than that of the NBG device. As a result, the device yielded a lower generation rate of 10.24 x10^{23} $cm^{-3}s^{-1}$ for active layer depth of 100nm. PM6:o-IDTBR harvested as harvested high light intensity from the far UV to near IR, i.e., from 350 -780nm as shown in Fig. 4.16b. Increasing the thickness beyond 100nm would let much lesser generation rate, since more defect states are expected to be created, whiles there be minimal G(x) at these depths.

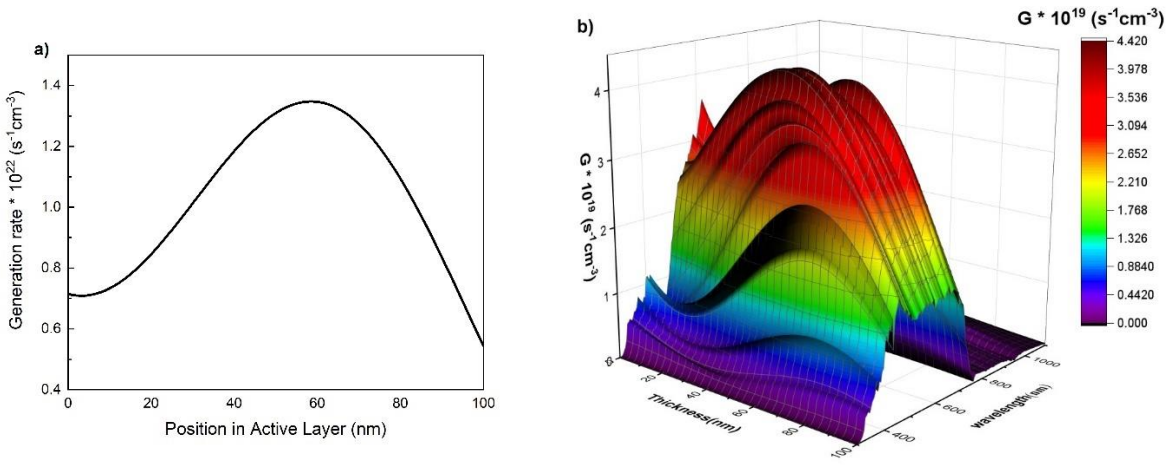

Figure 4.16: (a)Position of generation rate in active layer (b) 3-dimensional view of the generation rate versus its thickness of PM6:o-IDTBR active layer and wavelength.

The individual extraction efficiency for both holes and electrons are ≈ 0.55 whereas the total extraction efficiency of the whole charge carriers is WBG device ≈ 0.7. That is, out of the whole charges that are generated in the photoactive layer only 70% can contribute to photocurrent generation as shown Figure 4.17. Hence NBG device can extract more of the generated charge carries than that of WBG.

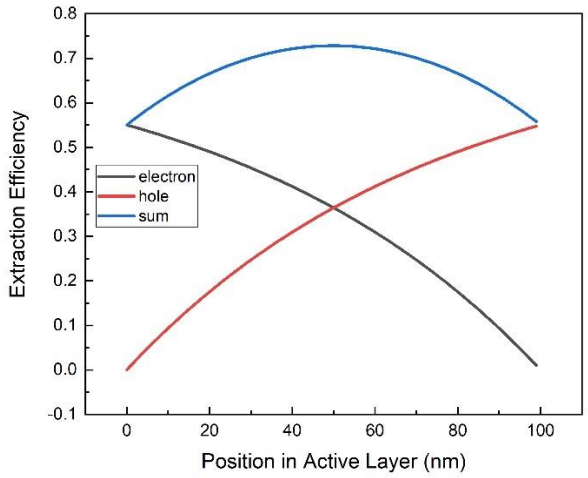

Figure 4.17: Extraction efficiency of electrons and holes of WBG PM6:o-IDTBR.

The WBG device yielded a much lower J_{SC} of 16.413 $mAcm^{-2}$ as compared to NBG device, this because of its low G(x). The J_{SC} increases with increasing thickness but as the thickness gets close to 100nm the JSC starts to decrease as shown Figure 4.18.

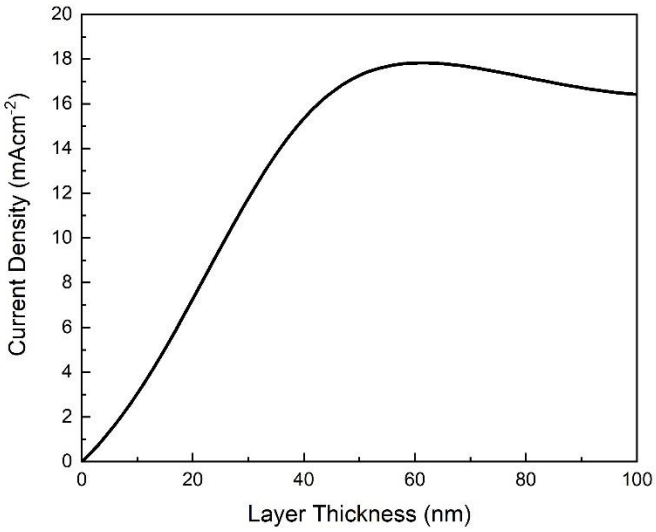

Figure 4.18: Current density for a given thickness of the PM6:o-IDTBR.

4.3 Illumination of the normal tandem devices.

4.3.1 Top cell: WBG Glass/ITO/ZnO/PM6:o-IDTBR/MoOx/ITO device

As aforementioned, tandem devices are new generation device structures that have been introduced in response to increasing the efficiency of solar cells. It is designed to break the SQ efficiency limit of single junction solar cells. Tandem devices consist of two or more sub cells that are stacked together to make a single device. The 2-Terminal and 4-Terminal are the most common structures of tandem devices, and both require a good optimization of the top and bottom cells to achieve high efficiency. For a series connected tandem solar cell, the total short circuit current density J_{SC} is the least J_{SC} among the subcells, whereas the total V_{OC} is the sum of the individual V_{OC} of the subcells, whiles the total fill factor FF depends on the FF of the top cell. Parallel tandem devices is limited by the least V_{OC} of the sub cells, whereas as the total J_{SC} is the sum of the individual J_{SC} of the subcells and the FF is the average FF of the individual subcells. In this part of the simulation our focus is to generate high J_{SC} from the tandem cell by optimizing the thickness of both active layers. Figure 4.19 shows a schematic model of our normal tandem device: WBG top cell and NBG bottom cell with optimized thicknesses of the active layers used in this simulation.

We model a normal 4T tandem device which employes two subcells connected in series and having different photoactive absorbers in each cell. A normal tandem device is a device that makes use of WBG cell as the top cell and NBG cell as the bottom cell. In the first tandem architecture, we made use of a WBG cell Glass/ITO/ZnO/PM6:o-IDTBR/MoOx/ITO as the top cell and Glass/ITO/ZnO/PM2:COTIC-4F/MoOx/Ag as the bottom cell show in Figure 4.19. As noted, a 4T tandem device should have four terminal (two terminals on each device), but here in Fig 4.19, we substitute Ag with ITO for the anode terminal of the top cell. This is because the

ITO is more transparent, have less values of n(λ) and k(λ), and hence it will make light easier to reach the bottom cell whiles Ag will block the light instead.

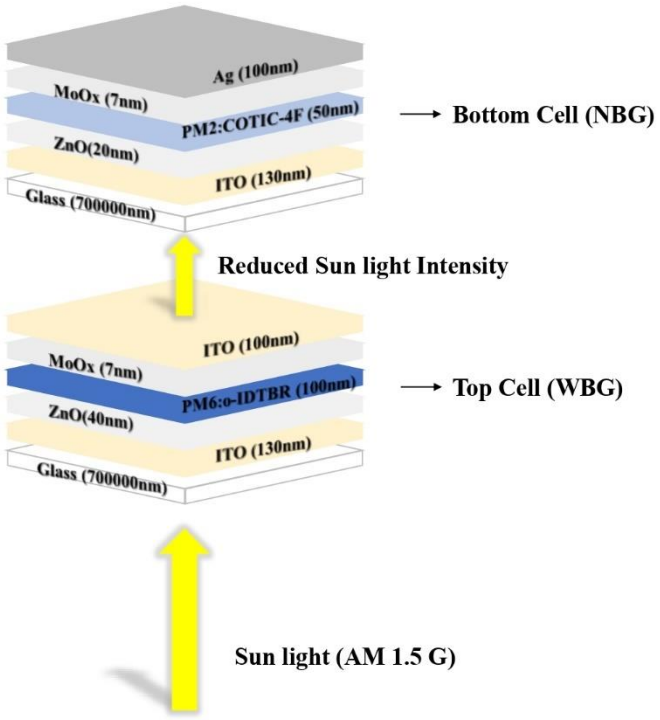

Figure 4.19: A schematic model of our normal tandem device: WBG top cell and NBG bottom cell.

Since it is a series connected tandem device, the current matching of the top and bottom cell is very important, we need to simulate the top and bottom cells such that they have high and almost equal amount of current at same time. To achieve this, we adjust the thickness of all the layers involved until we obtain an optimized thickness.

To begin with the WBG top cell, after careful adjustment of all the layers, the most optimized thicknesses are considered; ITO is 130nm; ZnO is 40nm; PM6:o-IDTBR is 100nm; $MoO_{X\ is}$ 7nm; and Ag is 100nm. We simulate the top WBG cell under illumination of 1 Sun AM 1.5 G, as light is first incident on the highly transparent glass substrate as shown in Figure 4.20, more than 90% of the light from 350 -1050nm is transmitted through to the efficient transparent

ITO and the ETL ZnO. Approximately 60% of the high intensity part of the light that reaches the PM2:COTIC-4F is absorbed from far UV – Visible (350-750 nm) spectrum. The rest of the light called reduced light intensity in this work is transmitted through the MoOx and the top ITO acting as the anode becomes the incident light to the bottom NBG cell as shown Fig 4.19.

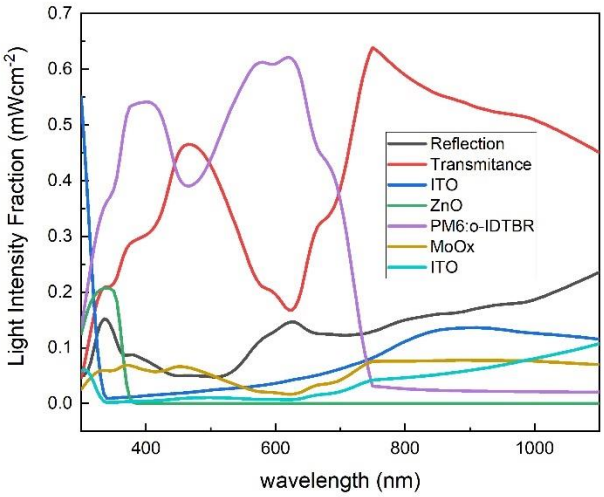

Figure 4.20: Light Absorption of all the layers involved in the top WBG cell architecture.

The behavior of the charge carrier generation rate in the active layer of the top WBG device is completely different from its single junction counter part. The G(x) is maximum at the surface of the PM6:o-IDTBR photoactive layer, and starts to decrease within the layer as the thickness increases. Figure 4.21 shows the G(x) in the active layer whole device, and as usual the charge carrier generation begins and end in the photoactive absorber.

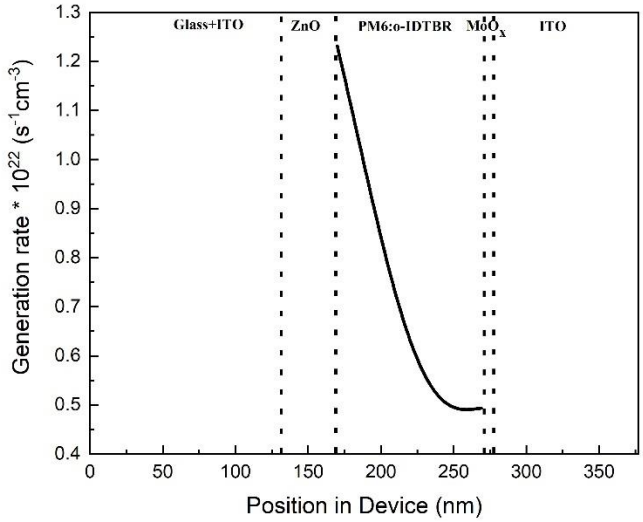

Figure 4.21: Generation at each position in the top WBG device.

The top WBG device yielded a G(x) of 7.227 x10^{23} $cm^{-3}s^{-1}$ which is quite different from its single junction counterpart, this is due to the less light absorption of the photoactive layer in the high intensity region. It absorbs ≈60% of light from UV to end of the visible spectrum whiles its single junction counterpart absorbs ≈80%, this accounts for its low carrier generation rate since G(x) have linear dependance on the absorbed light.

Figure 4.22a depicts the behavior of G(x) in the active layer, further increasing the thickness beyond 100nm would cause G(x) to decline heavily. Fig. 4.22b shows a vivid 3D image of what is happening in the active layer per each wavelength. We observe that clearly at the surface and 40nm deep inside the active layer the G(x) is high and peaks around 600nm and far UV light contributes less to G(x) throughout the thickness. After a depth of 50nm inside the active layer the G(x) became constant at a very low value ≈ 0.0002 x10^{23} $cm^{-3}s^{-1}$. All the light from ≈ 780 -1050nm were transparent and hence could not generate any charge carriers.

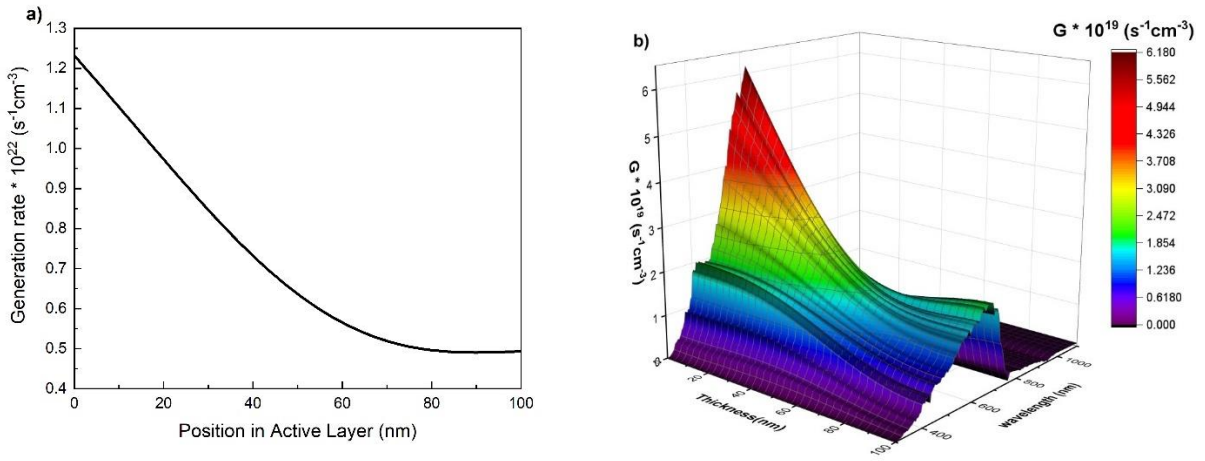

Figure 4.22: (a)Position of generation rate in active layer of the WBG top cell (b) 3-dimensional view of the generation rate versus its thickness of PM6:o-IDTBR active layer and wavelength.

From this low G(x) of the top WBG cell, only ≈75% of the charge carriers that are generated can be extracted as shown in figure 4.23. The individual extraction efficiency of a electron holes is ≈ 60%, which is very low and hence will lead low current generation.

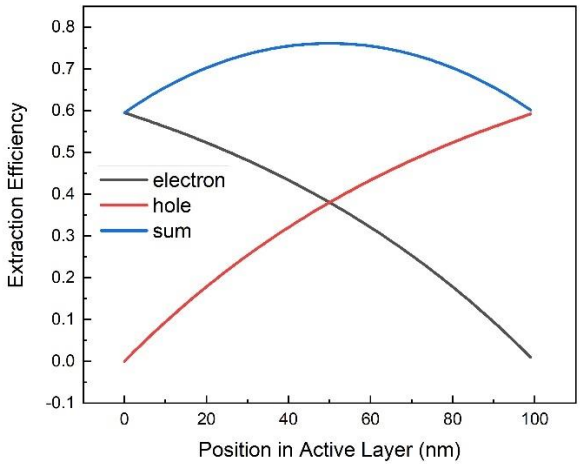

Figure 4.23: Extraction efficiency of electrons and holes of the top WBG cell.

The top WBG cell yielded a low J_{SC} of 11.579 $mAcm^{-2}$ due to reduction in the G(x)~ 7.227 $x10^{23}$ $cm^{-3}s^{-1}$ of the active layer. Though, after the optimization of the active layer and

considering current matching of the bottom cell, this is the maximum current it can generate. However, this J_{SC} is far below its single junction counterpart but considering all the parameters put in place, it is a good J_{SC} now.

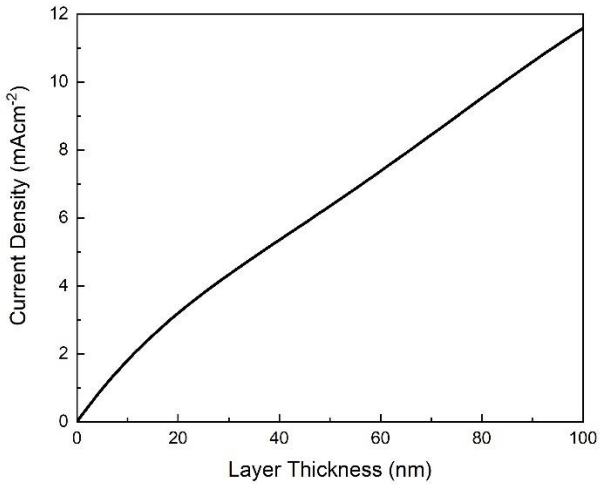

Figure 4.24: Current density for a given thickness of the photoactive layer of the WBG top cell.

Since the top cell is WBG cell there is no charge carrier generation after 760nm through to the IR- spectrum as shown in fig. 5f, hence there is enough spectra irradiance to harvest the bottom cell.

4.3.2 Bottom cell: ultra NBG Glass/ITO/ZnO/PM2:COTIC-4F/MoOx/Ag device

For the bottom cell of the tandem device we employed ultra-NBG photoactive layer PM2:COTIC-4F; ITO as the cathode; ZnO and MoOx as the ETL and HTL respectively; and Ag as the anode. Ag was used this time as a back electrode because we do not have any subcells. The bottom cell is then illuminated by the reduced sun light as shown in Fig. 2.19, the spectra irradiance of this reduced sun intensity was calculated as $F(\lambda) = \Phi E \times (1/\lambda)$. Where $F(\lambda)$ is the solar spectra irradiance; Φ is transmitted photons after topcell; E is energy of photons *and* λ is wavelength of transmitted photons. Hence, this is further plotted as the reduced sun intensity as

shown in Figure 2.19. Figure 4.25 shows the spectra irradiance AM 1.5 G of the sunlight that was illuminated on the top WBG cell and the reduced sunlight that was transmitted and illuminated on the bottom NBG cell.

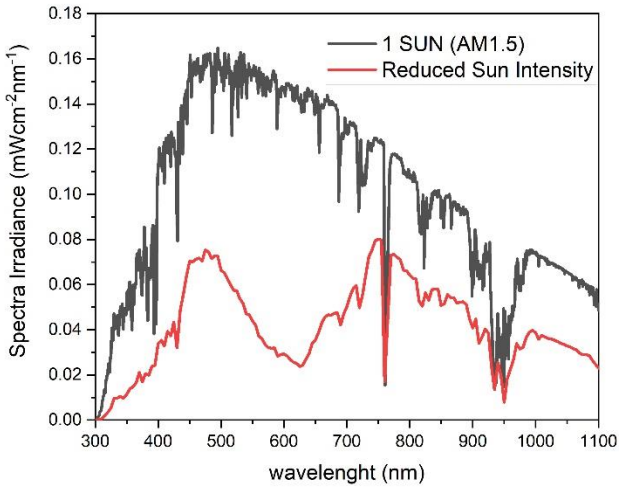

Figure 4.25: Standard AM 1.5 G solar irradiance spectrum and the reduced sun light Intensity of normal tandem device.

Here the main aim is to achieve a J_{SC} which is equal or almost the same as the that of the top cell. As aforementioned, one of the main limitations of a series tandem solar cell is the current matching of the top and bottom cell, and in other to do that we have to carefully adjust the the thickness of the photoactive layer and all the other layers of the bottom cell. The most optimized thickness considered; ITO is 130nm; ZnO is 40nm; PM6:o-IDTBR is 100nm; MoO_X is 7nm; and Ag is 100nm. We simulate the bottom NBG cell under illumination of the reduced sunlight intensity, as light is first incident on the highly transparent bottom glass substrate as shown in Figure 2.20, approximately 100% of the light from 350 -700nm is transmitted and 10-30% is absorbed 800-1100nm by the transparent ITO. 90% of the incident light on the ETL ZnO is tansmitted. Approximately 50-80% of the low intensity part of the light that reaches the PM2:COTIC-4F is absorbed from far 680-1050 nm, i.e is most of the IR spectrum is harvested.

The MoOx is transparent to the rest of the light that is transmitted through the photoactive layer, but the back metal electrode Ag absorbs 90% of this light as shown Figure 4.26.

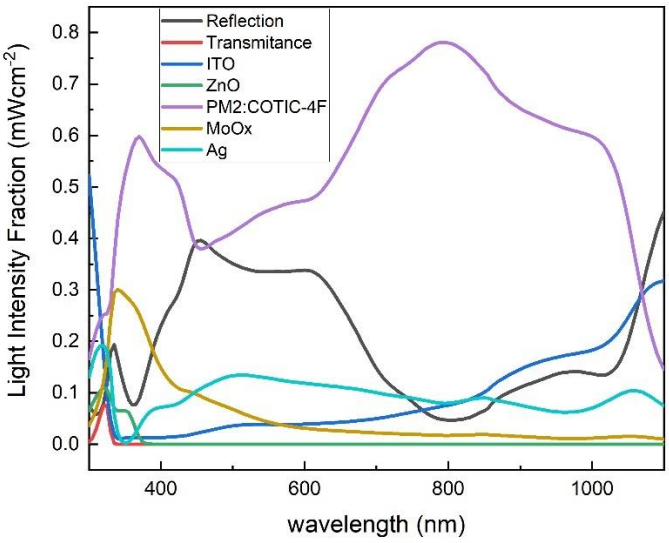

Figure 4.26: Light Absorption of all the layers involved in the bottom NBG cell architecture.

Figure 4.27 shows the behavior of the G(x) through the whole bottom NBG cell. The G(x) begins at a highest level in the PM2:COTIC-4F starts to decline linearly throughout the whole thickness till it reaches the bottom. This behavior is almost the same as its single junction and also similar to the G(x) behavior of the top WBG cell.

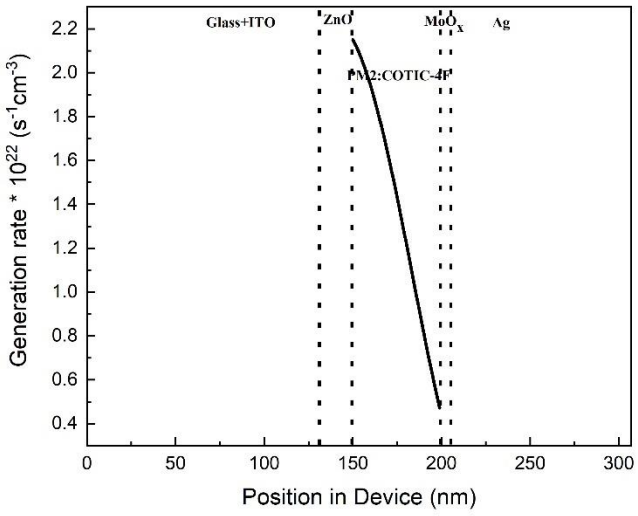

Figure 4.27: Generation at each position in the bottom NBG device.

The bottom NBG device yielded a G(x)~ 6.998 x10^{23} $cm^{-3}s^{-1}$ which is quite lower than the top cell and its single junction counterpart, this is due to the less light absorption of the photoactive layer of the reduced sunlight intensities. It absorbs ≈50-80% of light from some part of the visible spectrum to the whole of IR spectrum, whereas its single junction counterpart absorbs ≈90% of it. This accounts for the low carrier generation rate of the bottom cell since G(x) has linear dependance on the absorbed light. Figure 2.28a depicts the behavior of G(x) in the active layer as aforementioned, further increasing the thickness beyond 50nm would cause G(x) to decline heavily and no carriers would be generated at a point. Fig. 2.28b shows a clear 3D image of what is happening in the active layer per each wavelength. It is clearly seen that at the surface of the PM2:COTIC-4F and 30nm deep inside the active layer the G(x) is high and peaks around 900nm, however we recorded extremely low G(x) from 980 -1050 nm (far IR spectrum) throughout the whole thickness. And after a depth of 40nm inside the active layer the

G(x) became constant at a very low value ≈ 0.00015 x10^{23} $cm^{-3}s^{-1}$. Also, all the light from ≈ 350 -630nm contributed with a G(x) below ≈ 0.0002 x10^{23} $cm^{-3}s^{-1}$.

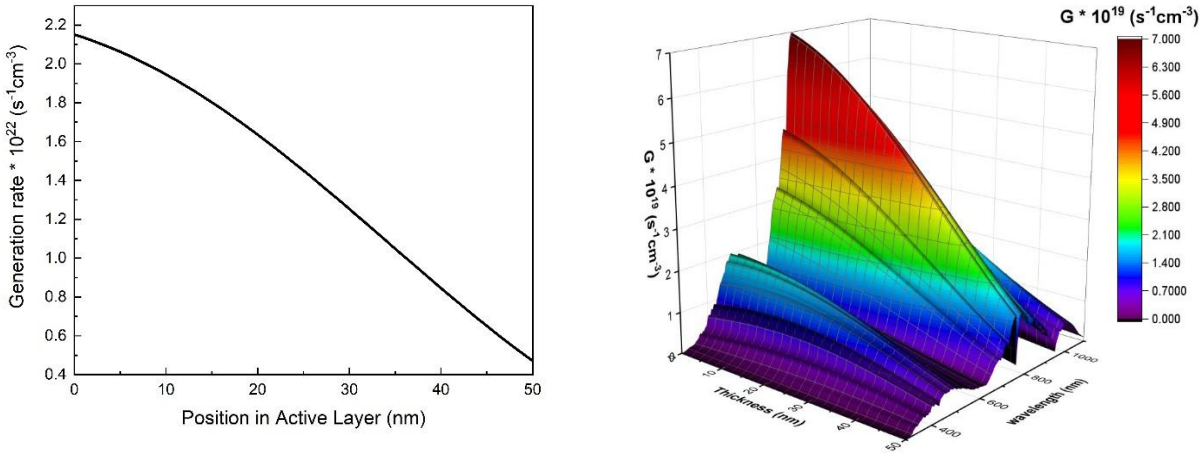

Figure 4.28: (a)Position of generation rate in active layer of the NBG bottom cell (b) 3-dimensional view of the generation rate versus its thickness of PM2:COTIC-4F active layer and wavelength.

The G(x) of the bottom NBG cell is low, however it could extract ≈90% of the charge carriers that are generated as shown in figure 4.29. There are no changes of the extraction efficiency of the bottom NBG cell and its single junction counterpart, this high efficiency could help extract the few charges that are generated by the NBG cell.

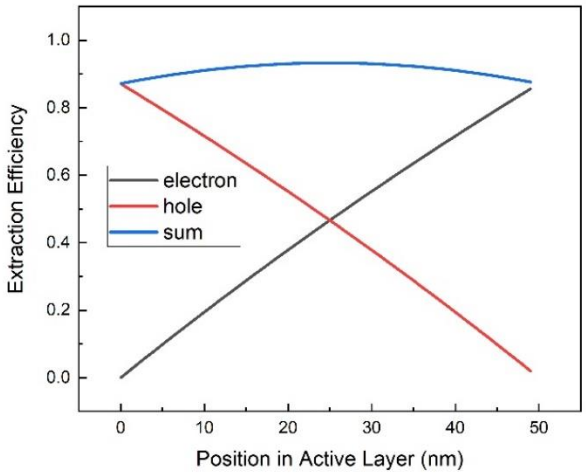

Figure 4.29: Extraction efficiency of electrons and holes of the bottom NBG cell.

The NBG cell yielded a low J_{SC} of 11.213 $mAcm^{-2}$ due to massive reduction in the G(x)~ 6.998 $x10^{23}$ $cm^{-3}s^{-1}$ of the active layer. Though, after the optimization of the active layer and considering current matching of the bottom cell, this is the maximum current it can generate. The main goal was to generate a high but equal or almost the same J_{SC} of the top and bottom cell. However, this J_{SC} is far below its single junction counterpart but matches with the J_{SC} ~ 11.579 $mAcm^{-2}$ of the top cell. The J_{SC} of the series tandem device attains the lowest J_{SC} of the sub cells for this reason, the theoretical J_{SC} of our model tandem device will be 11.213 $mAcm^{-2}$.

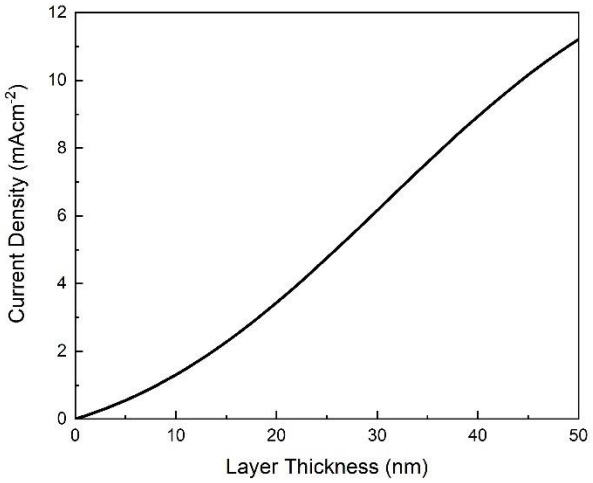

Figure 4.30: Current density for a given thickness of the photoactive layer of the NBG bottom cell.

4.4 Illumination of the flipped tandem devices

4.4.1 Top cell: ultra NBG Glass/ITO/ZnO/PM2:COTIC-4F/MoOx/Ag device.

We model another tandem device, this time we flip the position of the top and bottom cell, that is the bottom cell of the normal tandem device becomes the top cell whereas the top cell becomes the bottom cell. This ability to flip the tandem device is because of the unique properties of organic semiconductors, this makes them more distinct and make their usage less cumbersome unlike other semiconductors materials. The series connected subcells of the tandem device is interchanged, where the ultra-NBG cell that makes use of COTIC-4F as the photoactive absorber becomes the top cell and the WBG cell that employes PM6:o-IDTBR becomes the bottom cell. The top device with the architecture Glass/ITO/ZnO/PM2:COTIC-4F/MoOx/ITO and bottom device employs Glass/ITO/ZnO/PM6:o-IDTBR/MoOx/Ag. The top NBG device makes use of transparent ITO at anode contact to allow light to reach the bottom cell whereas the bottom WBG makes use of a metal electrode as the cathode, Ag. This is a series connected tandem device, and hence it is very necessary to match the current of the top and bottom cell.

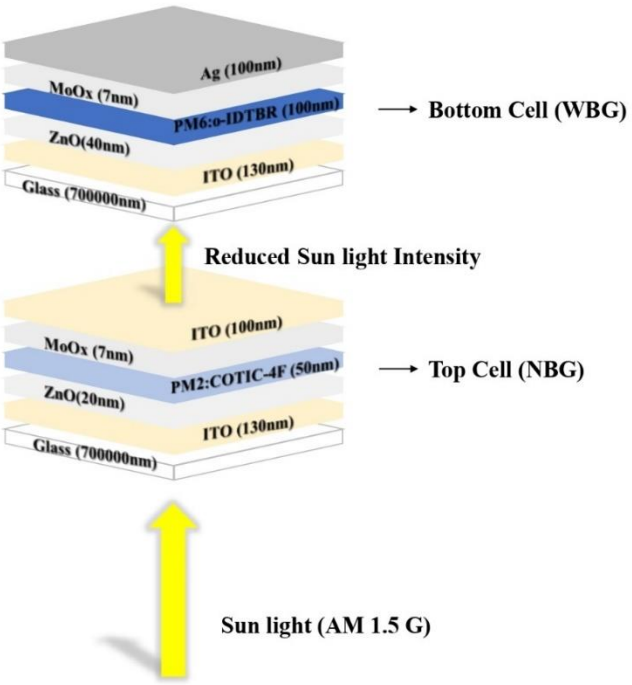

Figure 4.31: A schematic model of our normal tandem device: NBG top cell and WBG bottom cell.

To start with the NBG top cell, this time we maintain the already obtained optimized thicknesses used in the normal tandem device; ITO is 130nm; ZnO is 20nm; PM2:COTIC-4F is 50nm; MoO_X is 7nm; and ITO is 100nm. We simulate the top NBG cell under illumination of 1 Sun AM 1.5 G, as light is first incident on the highly transparent glass substrate as shown in Figure 4.31, approximately 99% of the light from 350 -1050nm is transmitted through the ITO. 100% the light incident on the ETL ZnO is transmitted. This time there is a very low about 20-35% of the low intensity part of the light that reaches the PM2:COTIC-4F is absorbed from 600-1050 nm, still harvesting some part of the visible spectrum and the IR spectrum. The rest of the light called reduced light intensity in this work is transmitted through the MoO_X and the top ITO acting as the anode becomes the incident light to the bottom WBG cell as shown in Fig 4.31.

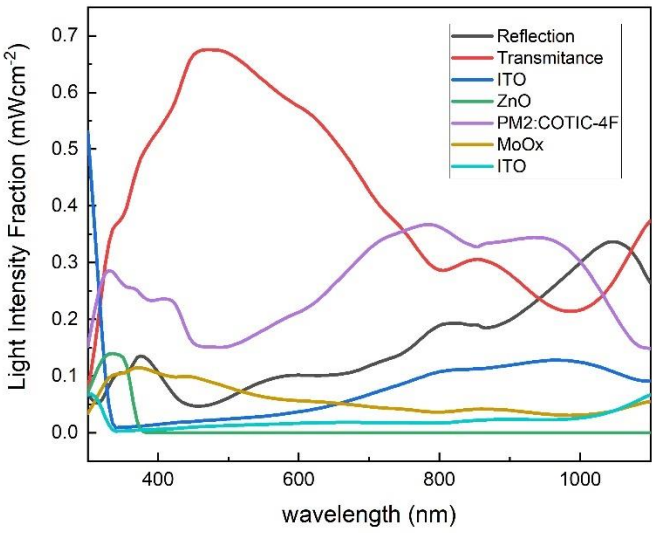

Figure 4.32: Extraction efficiency of electrons and holes of the top NBG cell.

Unlike the single junction counterpart of the NBG top cell, the behavior of the generation rate in this device is parabolic. The G(x) is at its maximum at the surface of the active layer and declines abruptly about ≈25nm into the device and starts to increase again to 0.147 $x10^{22}$ $cm^{-3}s^{-1}$ after another 25nm, bottom of the active layer as shown in Figure 4.32.

The NBG top device yielded a G(x)~ $7.227x10^{23}$ $cm^{-3}s^{-1}$ which is comparatively lower than its single junction counterpart , however, this G(x) is bigger than this same device used as the bottom cell as shown the normal tandem device. This is because it absorbs ≈20-40% of light from some part of the visible spectrum to the whole of IR spectrum, whereas its single junction counterpart absorbs ≈90% of it, this accounts for the low carrier generation rate of the NBG top cell as accounts. Figure 4.34a shows the behavior of G(x) in the active layer as aforementioned, further increasing the thickness beyond 50nm would cause G(x) to decline heavily and less carriers would be generated at a point as stated earlier.

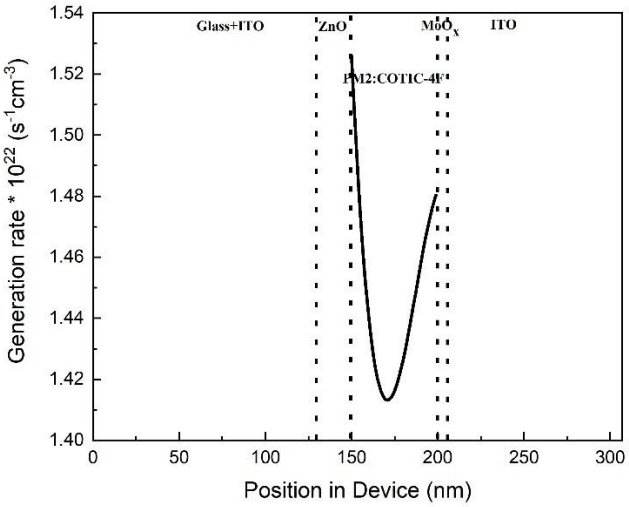

Figure 4.33: Generation at each position in the bottom NBG device.

The NBG top device yielded a G(x)~ 7.227x10^{23} $cm^{-3}s^{-1}$ which is comparatively lower than its single junction counterpart , however, this G(x) is bigger than this same device used as the bottom cell as shown the normal tandem device. This is because it absorbs ≈20-40% of light from some part of the visible spectrum to the whole of IR spectrum, whereas its single junction counterpart absorbs ≈90% of it, this accounts for the low carrier generation rate of the NBG top cell as accounts. Figure 4.34a shows the behavior of G(x) in the active layer as aforementioned, further increasing the thickness beyond 50nm would cause G(x) to decline heavily and less carriers would be generated at a point as stated earlier. Fig. 4.34b shows a vivid 3D image of what is happening in the active layer per each wavelength. It could clearly be seen that at from the surface of the PM2:COTIC-4F to the bottom, the G(x) yield values within 00025 -00035 x 10^{23} $cm^{-3}s^{-1}$ is at it at high wavelength ranges and yield extremely low G(x) at low wavelength ranges.

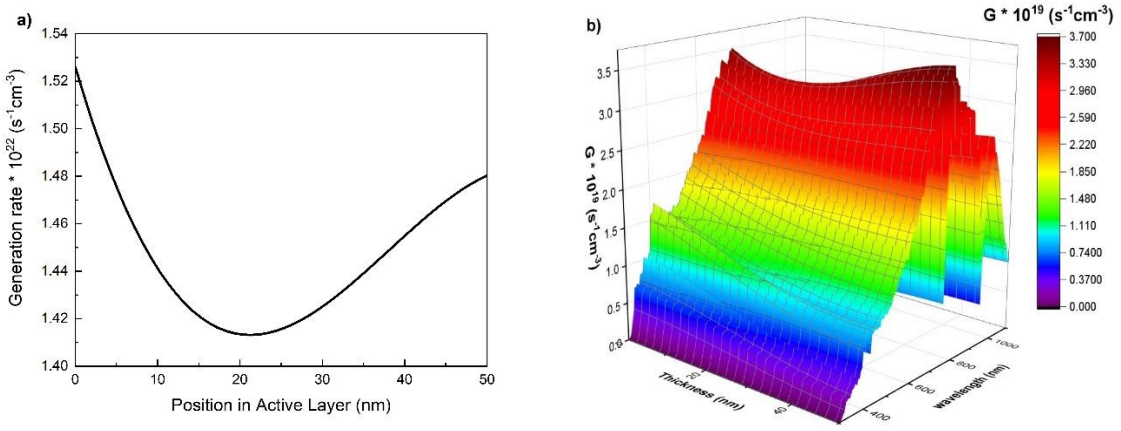

Figure 4.34: (a)Position of generation rate in active layer of the NBG bottom cell (b) 3-dimensional view of the generation rate versus its thickness of PM2:COTIC-4F active layer and wavelength.

The G(x) of the top NBG cell is moderately low, however it could extract ≈90% of the charge carriers that are generated as shown in figure 4.35 same as when its used bottom cell. Also, there are no changes of the extraction efficiency of the bottom NBG cell and its single junction counterpart, this is good news since most of the few chargers that are generated can be extracted to contribute to high current.

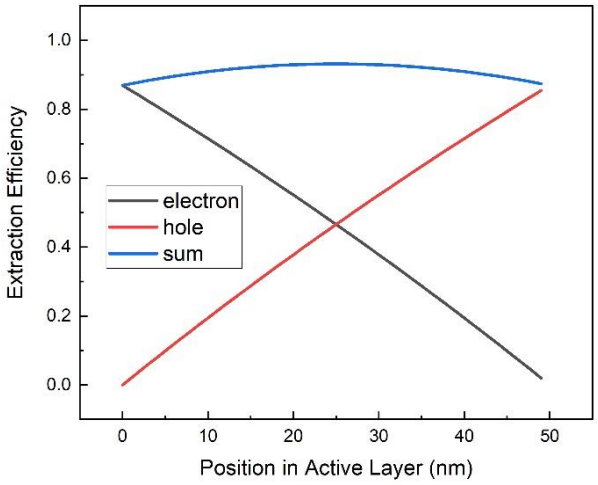

Figure 4.35: Extraction efficiency of electrons and holes of the top NBG cell.

For this flipped tandem device, the top NBG cell yielded a higher J_{SC} of 11.213 $mAcm^{-2}$ shown in Figure 4.36 compared to when it is integrated in tandem architecture as a bottom cell. However, it is immensely lower than its single junction counterpart obviously due to the massive reduction in the G(x)~ 7.227 $x10^{23}$ $cm^{-3}s^{-1}$ of the active layer. It is worth knowing that, optimized thickness of the active PM2:COTIC-4F layer used in the normal tandem device was maintained and this is the highest J_{SC} it can generate.

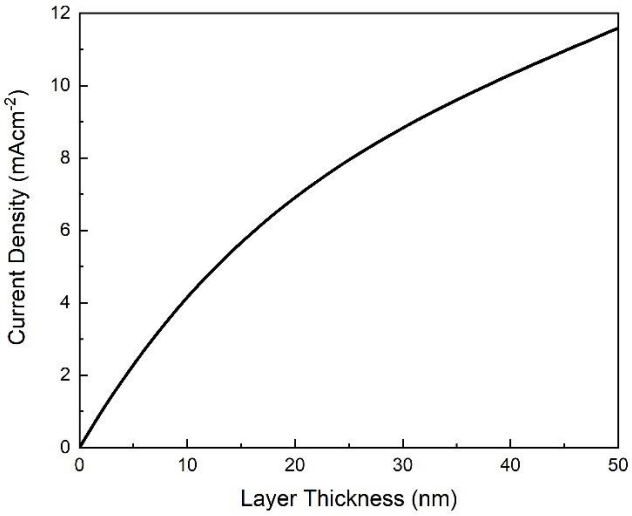

Figure 4.36: Current density for a given thickness of the photoactive layer of the NBG top cell.

4.4.2 Bottom cell: WBG Glass/ITO/ZnO/PM6:o-IDTBR/MoOx/ITO device.

This time the bottom cell of the tandem device we employe WBG photoactive layer PM6:o-IDTBR; ITO as the cathode; ZnO and MoOx as the ETL and HTL respectively; and Ag as the anode. The bottom cell again is then illuminated by the reduced sun light as shown in Fig. 4.31, the spectra irradiance of this reduced sun intensity was calculated as $F(\lambda) = \Phi E \times (1/\lambda)$. Where $F(\lambda)$ is the solar spectra irradiance; Φ is transmitted photons after topcell; E is energy of photons *and* λ is wavelength of transmitted photons. Hence, this is further plotted as the reduced sun intensity as shown in Figure 4.37. Figure 4.37 shows the spectra irradiance AM 1.5 G of the

sunlight that was illuminated on the top NBG cell and the reduced sunlight that was transmitted and illuminated on the bottom WBG cell.

One of the main limitations of a series tandem solar cell is the current matching of the top and bottom cell as aforementioned, maintaining the already optimized with the aim to achieve a J_{SC} which is equal or almost the same as the that of the top cell. The already optimized thickness of the cell is considered; ITO is 130nm; ZnO is 40nm; PM6:o-IDTBR is 100nm; MoO_X is 7nm; and Ag is 100nm. We simulate the bottom WBG cell under illumination of the reduced sunlight intensity, as light is first incident on the highly transparent bottom glass substrate as shown in Figure 4.31, approximately 100% of the light from 350 - 1050nm is transmitted and 10-15% is absorbed by the transparent ITO. About 85% of the light that incident on the ETL ZnO is transmitted.

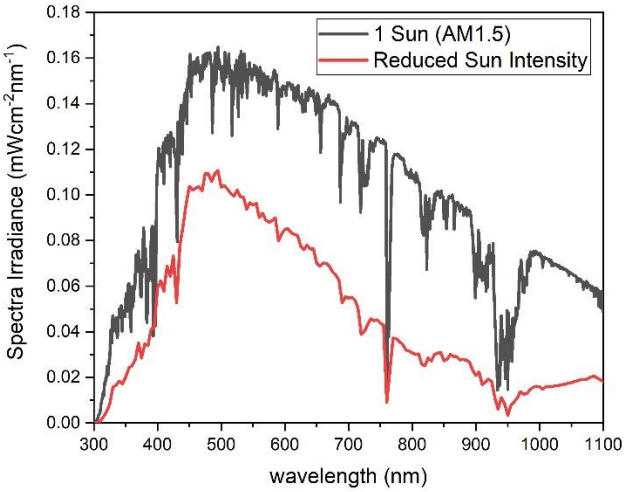

Figure 4.37: Standard AM 1.5 G solar irradiance spectrum and the reduced sun light Intensity of the flipped tandem device.

Approximately 50-80% of the high intensity part of the light that reaches the PM6:o-IDTBR is absorbed from far 350-680nm, that is from far UV and some part of the visible light

spectrum is harvested. The MoOx is transparent to the rest of the light that is transmitted through the photoactive layer, but the back metal electrode Ag absorbs 90% of this light as shown Figure 4.38.

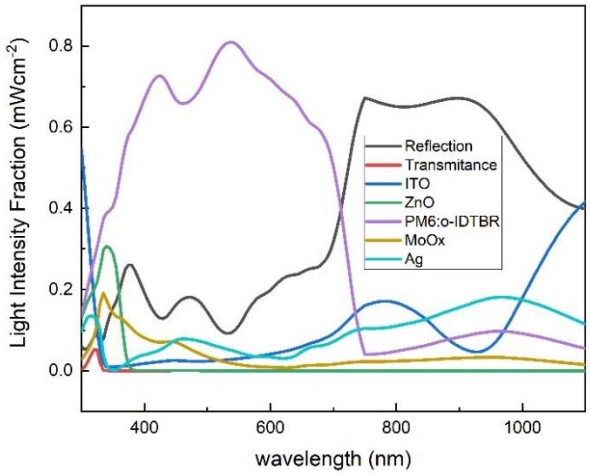

Figure 4.38: Extraction efficiency of electrons and holes of the top NBG cell.

The behavior of the charge carrier generation rate in the active layer of the top WBG device is also parabolic just as the top cell but this the G(x) peaks in the middle ≈50nm in the active layer, howerver it is completely different from its single junction counter part. The G(x) is modeteraly low at the surface of the PM6:o-IDTBR photoactive layer, and starts to increase within the layer as the thickness increases. Figure 4.39 shows the G(x) in the active layer whole device, and as usual the charge carrier generation begins and end in the photoactive absorber.

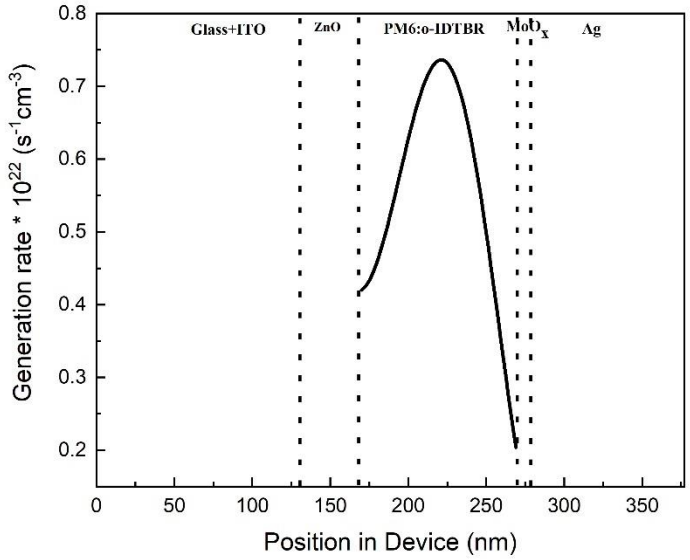

Figure 4.39: Generation at each position in the bottom WBG device.

Flipping the WBG device as a bottom device yielded the lowest G(x) of 5.574 x10^{23} $cm^{-3}s^{-1}$ of all the devices involved in this tandem simulation. This is due to the less absorption of the reduced sun light that incidents on the bottom cell, the photoactive layer can only absorbs ≈40% of light from far UV and 60-80% of the visible spectrum. For this reason, the device generated low amount of charge carrier since G(x) have linear dependance on the absorbed light. Figure 4.22a depicts the behavior of G(x) in the active layer, further increasing the thickness beyond 100nm will create more defect states increasing carrier recombination process as usual contributing to the decline G(x). Fig. 4.22b shows a vivid 3D image of what is happening in the active layer per each wavelength. We observe that clearly at the surface and 40nm deep inside the active layer the G(x) is high and peaks around 600nm and far UV light contributes less to G(x) throughout the thickness. After a depth of 50nm inside the active layer the G(x) became constant at a very low value ≈ 0.0002 x10^{23} $cm^{-3}s^{-1}$, all the light from ≈ 780 -1050nm were transparent and hence could not generate any charge carriers.

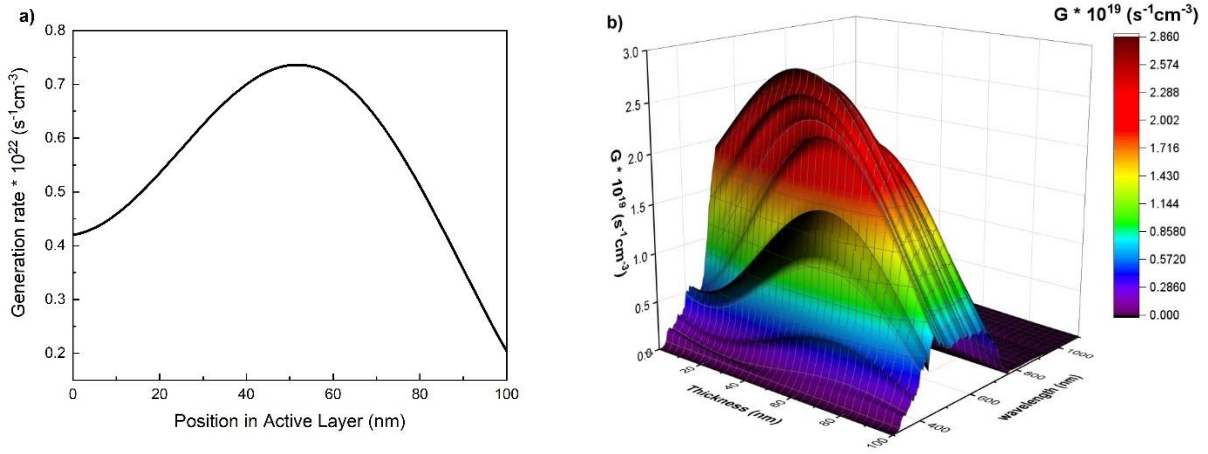

Figure 4.40: (a)Position of generation rate in active layer of the WBG bottom cell (b) 3-dimensional view of the generation rate versus its thickness of PM6:o-IDTBR active layer and wavelength.

Throughout this TM simulation, carrier extraction efficiency is one of the parameters that remains the same irrespective of the position of the cell. The total extraction efficiency is still ≈75% in the middle of the PM6:o-IDTBR, bottom WBG cell just as when it is used as Top cell or as single junction solar cell. Extraction of electrons and holes are vice versa, electrons ~62% are higher at the surface and decline to 0 at the bottom of the thickness~ 100nm, whereas the holes follow the opposite process as shown in Figure 4.41. This is all because of the position of the electrodes, ETL and HTL.

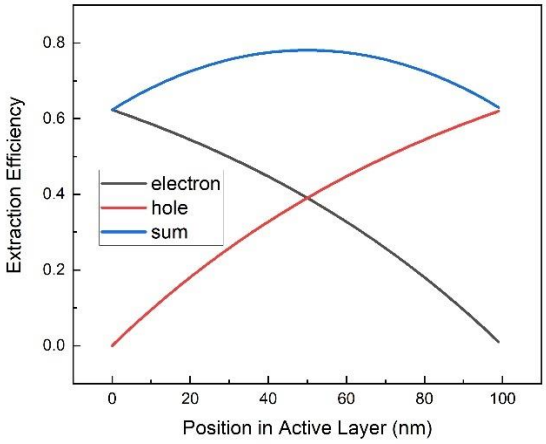

Figure 4.41: Extraction efficiency of electrons and holes of the bottom WBG cell.

The bottom WBG cell yielded a low J_{SC} of 8.931 $mAcm^{-2}$ as shown in Figure 2.42 due to its low G(x)~ 5.574 $x10^{23}$ $cm^{-3}s^{-1}$. In comparison with the high J_{SC} ~11.213 $mAcm^{-2}$ the top NBG cell, the J_{SC} of these subcells do not match. Therefore, the J_{SC} of the whole tandem cell will attain the least J_{SC} of the subcells, which is that of the bottom WBG cell. However, this tandem cell is still enough to be considered as a good device though its optoelectronic properties would fall short compared to its normal tandem counterpart.

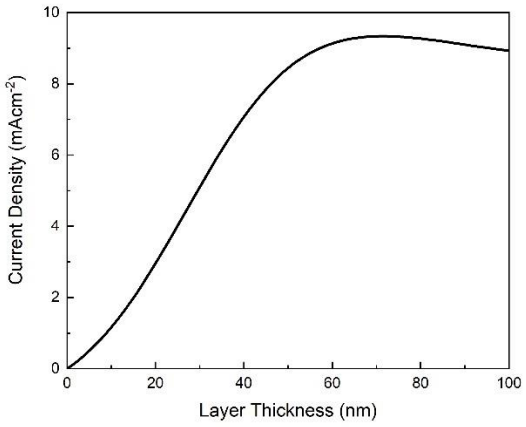

Figure 4.42: Generation at each position in the bottom WBG device.

Based on the optimized thicknesses of he photoactive layers, the results generated from our studies have been tabulated in table 4.1.

Table 4.1. Optoelectronic properties of simulated devices.

Device Structure	**Active layer**	**Thickness [nm]**	**G(x) [$cm^{-3}s^{-1}$]**	***η(x)***	**JSC [$mAcm^{-2}$]**
Single junction					
Inverted NBG	PM2:COTIC-4F	50	17.59e+23	0.75	28.189
Inverted WBG	PM6:o-IDTBR	100	10.24e+23	0.9	16.43
Normal tandem device					
Top cell	PM6:o-IDTBR	100	7.227	0.75	11.579
Bottom cell	PM2:COTIC-4F	50	6.99	0.9	11.213
Flipped tandem device					
Top cell	PM2:COTIC-4F	50	7.232	0.9	11.587
Bottom cell	PM6:o-IDTBR	100	5.574	0.75	8.931

CHAPTER 5

5 SUMMARY AND CONCLUSION

In this work we investigated the generation rate and short circuit current of organic tandem solar cells considering the optical properties of all the layers with optical-based transfer matrix simulation. The normal tandem devices consisted of a top cell that made use of PM6:o-IDTBR wide band gap (WBG) photoactive absorber whereas the bottom device consisted of PM2:COTIC-4F narrow band gap photoactive absorber. The second tandem device considered is what we called the flipped tandem device which makes use of PM2:COTIC-4F NBG as the top cell and PM6:o-IDTBR as the bottom cell. The structure of the individual cells was inverted form, where ITO/ZnO are used as the front electrode and MoO_X/Ag as back contact electrode.

Since Generation rate and short circuit current highly depend on the thicknesses of the photoactive absorbers, the optimized thicknesses of these layers that we could be possibly achieved for PM6: o-IDTBR and PM2:COTIC-4F are 100nm and 50nm. Our results show that the normal tandem device yielded a generation rate with a corresponding short circuit current (J_{SC}) of 11.213 $mAcm^{-2}$, whereas the flipped tandem device yielded a lower $J_{SC} \sim 8.931$.

The series connected 4T tandem device is a complicated structure, preferably the theoretical results show the structure should consist of a well optimized thicker WBG top cell and ultra-NBG bottom cell to fully achieve high device performance; and good current matching of the top and bottom cell to yield a high short circuit current.

Bibliography

1. Dyer-Smith, C.; Nelson, J.; Li, Y. Chapter I-5-B - Organic Solar Cells. In *McEvoy's Handbook of Photovoltaics (Third Edition)*; Kalogirou, S.A., Ed.; Academic Press, 2018; pp. 567–597 ISBN 978-0-12-809921-6.
2. Elsmani, M.I.; Fatima, N.; Jallorina, M.P.A.; Sepeai, S.; Su'ait, M.S.; Ahmad Ludin, N.; Mat Teridi, M.A.; Sopian, K.; Ibrahim, M.A. Recent Issues and Configuration Factors in Perovskite-Silicon Tandem Solar Cells towards Large Scaling Production. *Nanomaterials* **2021**, *11*, 3186.
3. Salim, M.B.; Nekovei, R.; Jeyakumar, R. Organic Tandem Solar Cells with 18.6% Efficiency. *Solar Energy* **2020**, *198*, 160–166.
4. Jošt, M.; Kegelmann, L.; Korte, L.; Albrecht, S. Monolithic Perovskite Tandem Solar Cells: A Review of the Present Status and Advanced Characterization Methods toward 30% Efficiency. *Advanced Energy Materials* **2020**, *10*, 1904102.
5. Eperon, G.E.; Hörantner, M.T.; Snaith, H.J. Metal Halide Perovskite Tandem and Multiple-Junction Photovoltaics. *Nature Reviews Chemistry* **2017**, *1*, 1–18.
6. Ameri, T.; Li, N.; Brabec, C.J. Highly Efficient Organic Tandem Solar Cells: A Follow up Review. *Energy & Environmental Science* **2013**, *6*, 2390–2413.
7. Goals of the Solar Energy Technologies Office Available online: https://www.energy.gov/eere/solar/goals-solar-energy-technologies-office (accessed on 20 August 2022).
8. Sharma, S.; Jain, K.K.; Sharma, A. Solar Cells: In Research and Applications—a Review. *Materials Sciences and Applications* **2015**, *6*, 1145.
9. Castellano, R.N. *Solar Panel Processing*; Archives contemporaines, 2010;

10. McEvoy, A.; Castaner, L.; Markvart, T. *Solar Cells: Materials, Manufacture and Operation*; Academic Press, 2012;

11. Bagher, A.M.; Vahid, M.M.A.; Mohsen, M. Types of Solar Cells and Application. *American Journal of optics and Photonics* **2015**, *3*, 94–113.

12. Verma, A.S.; Singh, S. Investigation and Multi-Objective Optimization of Monocrystalline Silicon Wafering Using Wire Electro-Discharge Machining. *Proceedings of the Institution of Mechanical Engineers, Part C: Journal of Mechanical Engineering Science* **2022**, 09544062221077635.

13. Chopra, K.L.; Paulson, P.D.; Dutta, V. Thin-Film Solar Cells: An Overview. *Progress in Photovoltaics: Research and applications* **2004**, *12*, 69–92.

14. Efaz, E.T.; Rhaman, M.M.; Al Imam, S.; Bashar, K.L.; Kabir, F.; Sakib, S.N.; Mourtaza, M.E. A Review of Major Technologies of Thin-Film Solar Cells. *Engineering Research Express* **2021**.

15. Maehlum, M.A. Energy Informative the Homeowner's Guide to Solar Panels, Best Thin Film Solar Panels—Amorphous, Cadmium Telluride or CIGS. *Last updated* **2015**, *6*.

16. Kang, H. Crystalline Silicon vs. Amorphous Silicon: The Significance of Structural Differences in Photovoltaic Applications. In Proceedings of the IOP Conference Series: Earth and Environmental Science; IOP Publishing, 2021; Vol. 726, p. 012001.

17. Solovan, M.M.; Mostovyi, A.I.; Parkhomenko, H.P.; Kaikanov, M.; Schopp, N.; Asare, E.A.; Kovaliuk, T.; Veřtát, P.; Ulyanytsky, K.S.; Korbutyak, D.V.; et al. A High-Detectivity, Fast-Response, and Radiation-Resistant TiN/CdZnTe Heterojunction Photodiode (Advanced Optical Materials 2/2023). *Advanced Optical Materials* **2023**, *11*, 2370005, doi:10.1002/adom.202370005.

18. Violas, A.F.; Oliveira, A.J.N.; Teixeira, J.P.; Lopes, T.S.; Barbosa, J.R.S.; Fernandes, P.A.; Salomé, P.M.P. Will Ultrathin CIGS Solar Cells Overtake the Champion Thin-Film Cells? Updated SCAPS Baseline Models Reveal Main Differences between Ultrathin and Standard CIGS. *Solar Energy Materials and Solar Cells* **2022**, *243*, 111792, doi:10.1016/j.solmat.2022.111792.

19. Third Generation Solar Cells. *III-Vs Review* **2003**, *16*, 53–55, doi:10.1016/S0961-1290(03)00792-0.

20. Zhao, Z.; Carpenter, M.A.; Petrukhina, M.A. 9 - Semiconductor Quantum Dots for Photoluminescence-Based Gas Sensing. In *Semiconductor Gas Sensors*; Jaaniso, R., Tan, O.K., Eds.; Woodhead Publishing Series in Electronic and Optical Materials; Woodhead Publishing, 2013; pp. 316–355 ISBN 978-0-85709-236-6.

21. Suhaimi, S.; Shahimin, M.M.; Alahmed, Z.A.; Chyskỳ, J.; Reshak, A.H. Materials for Enhanced Dye-Sensitized Solar Cell Performance: Electrochemical Application. *Int. J. Electrochem. Sci* **2015**, *10*, 2859–2871.

22. Sharma, K.; Sharma, V.; Sharma, S.S. Dye-Sensitized Solar Cells: Fundamentals and Current Status. *Nanoscale research letters* **2018**, *13*, 1–46.

23. Bertolli, M. Solar Cell Materials. Course: Solid State II. *Department of Physics, University of Tennessee* **2008**.

24. Choubey, P.C.; Oudhia, A.; Dewangan, R. A Review: Solar Cell Current Scenario and Future Trends. *Recent Research in Science and Technology* **2012**, *4*.

25. Wudl, F.; Srdanov, G. Conducting Polymer Formed of Poly (2-Methoxy, 5-(2'-Ethyl-Hexyloxy)-p-Phenylenevinylene) 1993.

26. Brabec, C.J.; Shaheen, S.E.; Winder, C.; Sariciftci, N.S.; Denk, P. Effect of LiF/Metal Electrodes on the Performance of Plastic Solar Cells. *Applied physics letters* **2002**, *80*, 1288–1290.

27. Zhu, R.; Kumar, A.; Yang, Y. Polarizing Organic Photovoltaics. *Advanced Materials* **2011**, *23*, 4193–4198.

28. Schopp, N.; Brus, V.V. A Review on the Materials Science and Device Physics of Semitransparent Organic Photovoltaics. *Energies* **2022**, *15*, 4639, doi:10.3390/en15134639.

29. Brus, V.V.; Lee, J.; Luginbuhl, B.R.; Ko, S.-J.; Bazan, G.C.; Nguyen, T.-Q. Hall of Fame Article: Solution-Processed Semitransparent Organic Photovoltaics: From Molecular Design to Device Performance (Adv. Mater. 30/2019). *Advanced Materials* **2019**, *31*, 1970219, doi:10.1002/adma.201970219.

30. Zuo, C.; Bolink, H.J.; Han, H.; Huang, J.; Cahen, D.; Ding, L. Advances in Perovskite Solar Cells. *Advanced Science* **2016**, *3*, 1500324.

31. Wang, D.; Wright, M.; Elumalai, N.K.; Uddin, A. Stability of Perovskite Solar Cells. *Solar Energy Materials and Solar Cells* **2016**, *147*, 255–275.

32. Li, N.; Niu, X.; Chen, Q.; Zhou, H. Towards Commercialization: The Operational Stability of Perovskite Solar Cells. *Chemical Society Reviews* **2020**, *49*, 8235–8286.

33. Li, H.; Zhang, W. Perovskite Tandem Solar Cells: From Fundamentals to Commercial Deployment. *Chemical Reviews* **2020**, *120*, 9835–9950.

34. Solovan, M.M.; Mostovyi, A.I.; Aidarkhanov, D.; Parkhomenko, H.P.; Akhtanova, G.; Schopp, N.; Asare, E.A.; Nauruzbayev, D.; Kaikanov, M.; Ng, A.; et al. Extreme Radiation Resistance of Self-Powered High-Performance

Cs0.04Rb0.04(FA0.65MA0.35)0.92Pb(I0.85Br0.14Cl0.01)3 Perovskite Photodiodes. *Advanced Optical Materials n/a*, 2203001, doi:10.1002/adom.202203001.

35. Zheng, X.; Alsalloum, A.Y.; Hou, Y.; Sargent, E.H.; Bakr, O.M. All-Perovskite Tandem Solar Cells: A Roadmap to Uniting High Efficiency with High Stability. *Accounts of Materials Research* **2020**, *1*, 63–76.
36. Hamadani, B.H. Understanding Photovoltaic Energy Losses under Indoor Lighting Conditions. *Appl Phys Lett* **2020**, *117*, 10.1063/5.0017890, doi:10.1063/5.0017890.
37. Heidarzadeh, H.; Rostami, A.; Dolatyari, M. Management of Losses (Thermalization-Transmission) in the Si-QDs inside 3C–SiC to Design an Ultra-High-Efficiency Solar Cell. *Materials Science in Semiconductor Processing* **2020**, *109*, 104936, doi:10.1016/j.mssp.2020.104936.
38. Andersson, O.; Kemerink, M. Enhancing Open-Circuit Voltage in Gradient Organic Solar Cells by Rectifying Thermalization Losses. *Solar RRL* **2020**, *4*, 2000400, doi:10.1002/solr.202000400.
39. Luo, X.; Wu, T.; Wang, Y.; Lin, X.; Su, H.; Han, Q.; Han, L. Progress of All-Perovskite Tandem Solar Cells: The Role of Narrow-Bandgap Absorbers. *Science China Chemistry* **2021**, *64*, 218–227.
40. Ho-Baillie, A.W.; Zheng, J.; Mahmud, M.A.; Ma, F.-J.; McKenzie, D.R.; Green, M.A. Recent Progress and Future Prospects of Perovskite Tandem Solar Cells. *Applied Physics Reviews* **2021**, *8*, 041307.
41. Wali, Q.; Elumalai, N.K.; Iqbal, Y.; Uddin, A.; Jose, R. Tandem Perovskite Solar Cells. *Renewable and Sustainable Energy Reviews* **2018**, *84*, 89–110.

42. Wahad, F.; Abid, Z.; Gulzar, S.; Aslam, M.S.; Rafique, S.; Shahid, M.; Altaf, M.; Ashraf, R.S. Semitransparent Perovskite Solar Cells. *Fundamentals of Solar Cell Design* **2021**, 461–503.

43. Akhil, S.; Akash, S.; Pasha, A.; Kulkarni, B.; Jalalah, M.; Alsaiari, M.; Harraz, F.A.; Balakrishna, R.G. Review on Perovskite Silicon Tandem Solar Cells: Status and Prospects 2T, 3T and 4T for Real World Conditions. *Materials & Design* **2021**, *211*, 110138.

44. Khan, F.; Rezgui, B.D.; Khan, M.T.; Al-Sulaiman, F. Perovskite-Based Tandem Solar Cells: Device Architecture, Stability, and Economic Perspectives. *Renewable and Sustainable Energy Reviews* **2022**, 112553.

45. Karani, A.H. Materials, Photophysics and Device Designs for High Efficiency Photovoltaics. PhD Thesis, University of Cambridge, 2019.

46. Wang, Z.; Song, Z.; Yan, Y.; Liu, S.; Yang, D. Perovskite—a Perfect Top Cell for Tandem Devices to Break the S–Q Limit. *Advanced Science* **2019**, *6*, 1801704.

47. Lang, K.; Guo, Q.; He, Z.; Bai, Y.; Yao, J.; Wakeel, M.; Alhodaly, M.S.; Hayat, T.; Tan, Z. High Performance Tandem Solar Cells with Inorganic Perovskite and Organic Conjugated Molecules to Realize Complementary Absorption. *The Journal of Physical Chemistry Letters* **2020**, *11*, 9596–9604.

48. Rossi, D.; Forberich, K.; Matteocci, F.; Auf der Maur, M.; Egelhaaf, H.-J.; Brabec, C.J.; Di Carlo, A. Design of Highly Efficient Semitransparent Perovskite/Organic Tandem Solar Cells. *Solar RRL* **2022**, 2200242.

49. Löper, P.; Niesen, B.; Moon, S.-J.; De Nicolas, S.M.; Holovsky, J.; Remes, Z.; Ledinsky, M.; Haug, F.-J.; Yum, J.-H.; De Wolf, S. Organic–Inorganic Halide Perovskites:

Perspectives for Silicon-Based Tandem Solar Cells. *IEEE Journal of Photovoltaics* **2014**, *4*, 1545–1551.

50. Abbasiyan, A.; Noori, M.; Baghban, H. A Highly Efficient 4-Terminal Perovskite/Silicon Tandem Solar Cells Using QIBC and IBC Configurations in Top and Bottom Cells, Respectively. *Materials Today Energy* **2022**, 101055.
51. HOMO/LUMO Available online: http://ch301.cm.utexas.edu/imfs/#mo/homo-lumo.html (accessed on 4 October 2022).
52. Iskander, A. Polymer Solar Cells. **2019**, *2*, 9.
53. Li, G.; Zhu, R.; Yang, Y. Polymer Solar Cells. *Nature Photon* **2012**, *6*, 153–161, doi:10.1038/nphoton.2012.11.
54. Ameri, T.; Dennler, G.; Lungenschmied, C.; J. Brabec, C. Organic Tandem Solar Cells: A Review. *Energy & Environmental Science* **2009**, *2*, 347–363, doi:10.1039/B817952B.
55. Tomar, A.; Johari, R. *Polymer Tandem Solar Cell: An Overview*; 2018; p. 95;.
56. Sista, S.; Hong, Z.; Chen, L.-M.; Yang, Y. Tandem Polymer Photovoltaic Cells—Current Status, Challenges and Future Outlook. *Energy & Environmental Science* **2011**, *4*, 1606–1620, doi:10.1039/C0EE00754D.
57. Shi, Z.; Bai, Y.; Chen, X.; Zeng, R.; Tan, Z. Tandem Structure: A Breakthrough in Power Conversion Efficiency for Highly Efficient Polymer Solar Cells. *Sustainable Energy & Fuels* **2019**, *3*, 910–934, doi:10.1039/C8SE00601F.
58. Köhnen, E.; Jošt, M.; Belen Morales-Vilches, A.; Tockhorn, P.; Al-Ashouri, A.; Macco, B.; Kegelmann, L.; Korte, L.; Rech, B.; Schlatmann, R.; et al. Highly Efficient Monolithic Perovskite Silicon Tandem Solar Cells: Analyzing the Influence of Current Mismatch on

Device Performance. *Sustainable Energy & Fuels* **2019**, *3*, 1995–2005, doi:10.1039/C9SE00120D.

59. Li, T.-T.; Yang, Y.-B.; Li, G.-R.; Chen, P.; Gao, X.-P. Two-Terminal Perovskite-Based Tandem Solar Cells for Energy Conversion and Storage. *Small* **2021**, *17*, 2006145, doi:10.1002/smll.202006145.

60. Du, D.; Gao, C.; Wang, H.; Shen, W. Photovoltaic Performance of Bifacial Perovskite/c-Si Tandem Solar Cells. *Journal of Power Sources* **2022**, *540*, 231622, doi:10.1016/j.jpowsour.2022.231622.

61. Predicted Power Output of Silicon-Based Bifacial Tandem Photovoltaic Systems | Elsevier Enhanced Reader Available online: https://reader.elsevier.com/reader/sd/pii/S2542435119306324?token=D64244BC04A6ECD6B5998FEFDA90EC62E0FA0806921C1CB00D0BB6D95CD11708E89BBA7A3EF0F9978B2D7FD6F39F3B7C&originRegion=eu-west-1&originCreation=20221004105744 (accessed on 4 October 2022).

62. Energy Yield of Bifacial Textured Perovskite/Silicon Tandem Photovoltaic Modules | Elsevier Enhanced Reader Available online: https://reader.elsevier.com/reader/sd/pii/S0927024819306932?token=2D8D6B93D63CC6355B2F082E6F9CD1BCF551A5D271B2C42584BDB0A0326266280B46FA4ADD69F7D84C1758905127E5D9&originRegion=eu-west-1&originCreation=20221004105857 (accessed on 4 October 2022).

63. Jacobs, D.A.; Langenhorst, M.; Sahli, F.; Richards, B.S.; White, T.P.; Ballif, C.; Catchpole, K.R.; Paetzold, U.W. Light Management: A Key Concept in High-Efficiency

Perovskite/Silicon Tandem Photovoltaics. *The journal of physical chemistry letters* **2019**, *10*, 3159–3170.

64. Qarony, W.; Hossain, M.I.; Jovanov, V.; Salleo, A.; Knipp, D.; Tsang, Y.H. Influence of Perovskite Interface Morphology on the Photon Management in Perovskite/Silicon Tandem Solar Cells. *ACS Appl. Mater. Interfaces* **2020**, *12*, 15080–15086, doi:10.1021/acsami.9b21985.

65. Hadipour, A.; de Boer, B.; Blom, P.W.M. Device Operation of Organic Tandem Solar Cells. *Organic Electronics* **2008**, *9*, 617–624, doi:10.1016/j.orgel.2008.03.009.

66. Guo, X.; Liu, F.; Yue, W.; Xie, Z.; Geng, Y.; Wang, L. Efficient Tandem Polymer Photovoltaic Cells with Two Subcells in Parallel Connection. *Organic Electronics* **2009**, *10*, 1174–1177, doi:10.1016/j.orgel.2009.06.010.

67. Tanaka, S.; Mielczarek, K.; Ovalle-Robles, R.; Wang, B.; Hsu, D.; Zakhidov, A.A. Monolithic Parallel Tandem Organic Photovoltaic Cell with Transparent Carbon Nanotube Interlayer. *Appl. Phys. Lett.* **2009**, *94*, 113506, doi:10.1063/1.3095594.

68. Glaser, K.; Pütz, A.; Mescher, J.; Bahro, D.; Colsmann, A. Organic Tandem Solar Cells. In *Organic Photovoltaics*; John Wiley & Sons, Ltd, 2014; pp. 445–464 ISBN 978-3-527-65691-2.

69. Tang, C.W. Two-layer Organic Photovoltaic Cell. *Appl. Phys. Lett.* **1986**, *48*, 183–185, doi:10.1063/1.96937.

70. Yu, G.; Gao, J.; Hummelen, J.C.; Wudl, F.; Heeger, A.J. Polymer Photovoltaic Cells: Enhanced Efficiencies via a Network of Internal Donor-Acceptor Heterojunctions. *Science* **1995**, *270*, 1789–1791.

71. Schopp, N.; Akhtanova, G.; Panoy, P.; Arbuz, A.; Chae, S.; Yi, A.; Kim, H.J.; Promarak, V.; Nguyen, T.-Q.; Brus, V.V. Unraveling Device Physics of Dilute-Donor Narrow-Bandgap Organic Solar Cells with Highly Transparent Active Layers. *Advanced Materials* **2022**, *34*, 2203796, doi:10.1002/adma.202203796.

72. Amollo, T.A.; Mola, G.T.; Nyamori, V.O. Organic Solar Cells: Materials and Prospects of Graphene for Active and Interfacial Layers. *Critical Reviews in Solid State and Materials Sciences* **2020**, *45*, 261–288, doi:10.1080/10408436.2019.1632791.

73. Halls: Exciton Diffusion and Dissociation in a Poly... - Google Scholar Available online: https://scholar.google.com/scholar_lookup?hl=en&volume=68&publication_year=1996&pages=3120-3122&issue=22&author=J.+J.+Halls&author=K.+Pichler&author=R.+H.+Friend&author=S.+Moratti&author=A.+Holmes&title=Exciton+diffusion+and+dissociation+in+a+poly+%28p%E2%80%90phenylenevinylene%29%2FC60+heterojunction+photovoltaic+cell (accessed on 6 October 2022).

74. Halls: The Photovoltaic Effect in a Poly (p-Phenyleneviny... - Google Scholar Available online: https://scholar.google.com/scholar_lookup?hl=en&volume=85&publication_year=1997&pages=1307-1308&issue=1-3&author=J.+Halls&author=R.+Friend&title=The+photovoltaic+effect+in+a+poly+%28p-phenylenevinylene%29%2Fperylene+heterojunction (accessed on 6 October 2022).

75. Kerp: Exciton Transport in Organic Dye Layers for... - Google Scholar Available online: https://scholar.google.com/scholar_lookup?hl=en&volume=298&publication_year=1998&pages=302-

308&issue=4%E2%80%936&author=H.+Kerp&author=H.+Donker&author=R.+Koehorst&author=T.+Schaafsma&author=E.+Van+Faassen&title=Exciton+transport+in+organic+dye+layers+for+photovoltaic+applications (accessed on 6 October 2022).

76. Landerer, D.; Sprau, C.; Ebenhoch, B.; Colsmann, A. 9 - New Directions for Organic Thin-Film Solar Cells: Stability and Performance. In *Advanced Micro- and Nanomaterials for Photovoltaics*; Ginley, D., Fix, T., Eds.; Micro and Nano Technologies; Elsevier, 2019; pp. 195–244 ISBN 978-0-12-814501-2.

77. Chen, C.-C. Organic Tandem Solar Cells: Design and Formation. Ph.D., University of California, Los Angeles: United States -- California.

78. Kim, J.Y.; Lee, K.; Coates, N.E.; Moses, D.; Nguyen, T.-Q.; Dante, M.; Heeger, A.J. Efficient Tandem Polymer Solar Cells Fabricated by All-Solution Processing. *Science* **2007**, *317*, 222–225.

79. Dou, L.; You, J.; Yang, J.; Chen, C.-C.; He, Y.; Murase, S.; Moriarty, T.; Emery, K.; Li, G.; Yang, Y. Tandem Polymer Solar Cells Featuring a Spectrally Matched Low-Bandgap Polymer. *Nature Photonics* **2012**, *6*, 180–185.

80. Zhou, Y.; Fuentes-Hernandez, C.; Shim, J.; Meyer, J.; Giordano, A.J.; Li, H.; Winget, P.; Papadopoulos, T.; Cheun, H.; Kim, J. A Universal Method to Produce Low–Work Function Electrodes for Organic Electronics. *Science* **2012**, *336*, 327–332.

81. Tress, W.; Merten, A.; Furno, M.; Hein, M.; Leo, K.; Riede, M. Correlation of Absorption Profile and Fill Factor in Organic Solar Cells: The Role of Mobility Imbalance. *Advanced Energy Materials* **2013**, *3*, 631–638.

82. Boix, P.P.; Ajuria, J.; Etxebarria, I.; Pacios, R.; Garcia-Belmonte, G.; Bisquert, J. Role of ZnO Electron-Selective Layers in Regular and Inverted Bulk Heterojunction Solar Cells. *The Journal of Physical Chemistry Letters* **2011**, *2*, 407–411.

83. Murase, S.; Yang, Y. Solution Processed MoO3 Interfacial Layer for Organic Photovoltaics Prepared by a Facile Synthesis Method. *Advanced materials* **2012**, *24*, 2459–2462.

84. Xu, X.; Yu, L.; Peng, Q. Recent Advances in Wide Bandgap Polymer Donors and Their Applications in Organic Solar Cells. *Chinese Journal of Chemistry* **2021**, *39*, 243–254, doi:10.1002/cjoc.202000451.

85. Zheng, Z.; Wang, J.; Bi, P.; Ren, J.; Wang, Y.; Yang, Y.; Liu, X.; Zhang, S.; Hou, J. Tandem Organic Solar Cell with 20.2% Efficiency. *Joule* **2022**, *6*, 171–184, doi:10.1016/j.joule.2021.12.017.

86. Hadipour, A.; de Boer, B.; Wildeman, J.; Kooistra, F.B.; Hummelen, J.C.; Turbiez, M.G.R.; Wienk, M.M.; Janssen, R. a. J.; Blom, P.W.M. Solution-Processed Organic Tandem Solar Cells. *Advanced Functional Materials* **2006**, *16*, 1897–1903, doi:10.1002/adfm.200600138.

87. Hagemann, O.; Bjerring, M.; Nielsen, N.Chr.; Krebs, F.C. All Solution Processed Tandem Polymer Solar Cells Based on Thermocleavable Materials☆. *Solar Energy Materials and Solar Cells* **2008**, *92*, 1327–1335, doi:10.1016/j.solmat.2008.05.005.

88. Sun, X.W.; Zhao, D.W.; Ke, L.; Kyaw, A.K.K.; Lo, G.Q.; Kwong, D.L. Inverted Tandem Organic Solar Cells with a MoO3/Ag/Al/Ca Intermediate Layer. *Appl. Phys. Lett.* **2010**, *97*, 053303, doi:10.1063/1.3469928.

89. Sakai, J.; Kawano, K.; Yamanari, T.; Taima, T.; Yoshida, Y.; Fujii, A.; Ozaki, M. Efficient Organic Photovoltaic Tandem Cells with Novel Transparent Conductive Oxide Interlayer and Poly (3-Hexylthiophene): Fullerene Active Layers. *Solar Energy Materials and Solar Cells* **2010**, *94*, 376–380, doi:10.1016/j.solmat.2009.08.008.

90. Chou, C.-H.; Kwan, W.L.; Hong, Z.; Chen, L.-M.; Yang, Y. A Metal-Oxide Interconnection Layer for Polymer Tandem Solar Cells with an Inverted Architecture. *Adv. Mater.* **2011**, *23*, 1282–1286, doi:10.1002/adma.201001033.

91. Zheng, Z.; Zhang, S.; Zhang, J.; Qin, Y.; Li, W.; Yu, R.; Wei, Z.; Hou, J. Over 11% Efficiency in Tandem Polymer Solar Cells Featured by a Low-Band-Gap Polymer with Fine-Tuned Properties. *Advanced Materials* **2016**, *28*, 5133–5138, doi:10.1002/adma.201600373.

92. Liu, W.; Li, S.; Huang, J.; Yang, S.; Chen, J.; Zuo, L.; Shi, M.; Zhan, X.; Li, C.-Z.; Chen, H. Nonfullerene Tandem Organic Solar Cells with High Open-Circuit Voltage of 1.97 V. *Advanced Materials* **2016**, *28*, 9729–9734, doi:10.1002/adma.201603518.

93. Zhang, Q.; Wan, X.; Liu, F.; Kan, B.; Li, M.; Feng, H.; Zhang, H.; Russell, T.P.; Chen, Y. Evaluation of Small Molecules as Front Cell Donor Materials for High-Efficiency Tandem Solar Cells. *Advanced Materials* **2016**, *28*, 7008–7012, doi:10.1002/adma.201601435.

94. Zuo, L.; Yu, J.; Shi, X.; Lin, F.; Tang, W.; Jen, A.K.-Y. High-Efficiency Nonfullerene Organic Solar Cells with a Parallel Tandem Configuration. *Advanced Materials* **2017**, *29*, 1702547, doi:10.1002/adma.201702547.

95. Chen, S.-C.; Zheng, Q.; Yin, Z.; Cai, D.; Ma, Y. High Performance Thermal-Treatment-Free Tandem Polymer Solar Cells with High Fill Factors. *Organic Electronics* **2017**, *47*, 79–84, doi:10.1016/j.orgel.2017.05.008.

96. Chen, S.; Zhang, G.; Liu, J.; Yao, H.; Zhang, J.; Ma, T.; Li, Z.; Yan, H. An All-Solution Processed Recombination Layer with Mild Post-Treatment Enabling Efficient Homo-Tandem Non-Fullerene Organic Solar Cells. *Advanced Materials* **2017**, *29*, 1604231, doi:10.1002/adma.201604231.

97. Zhang, Y.; Kan, B.; Sun, Y.; Wang, Y.; Xia, R.; Ke, X.; Yi, Y.-Q.-Q.; Li, C.; Yip, H.-L.; Wan, X.; et al. Nonfullerene Tandem Organic Solar Cells with High Performance of 14.11%. *Advanced Materials* **2018**, *30*, 1707508, doi:10.1002/adma.201707508.

98. Guo, B.; Li, W.; Luo, G.; Guo, X.; Yao, H.; Zhang, M.; Hou, J.; Li, Y.; Wong, W.-Y. Exceeding 14% Efficiency for Solution-Processed Tandem Organic Solar Cells Combining Fullerene- and Nonfullerene-Based Subcells with Complementary Absorption. *ACS Energy Lett.* **2018**, *3*, 2566–2572, doi:10.1021/acsenergylett.8b01448.

99. Chen, S.; Yao, H.; Hu, B.; Zhang, G.; Arunagiri, L.; Ma, L.-K.; Huang, J.; Zhang, J.; Zhu, Z.; Bai, F.; et al. A Nonfullerene Semitransparent Tandem Organic Solar Cell with 10.5% Power Conversion Efficiency. *Advanced Energy Materials* **2018**, *8*, 1800529, doi:10.1002/aenm.201800529.

100. Meng, L.; Zhang, Y.; Wan, X.; Li, C.; Zhang, X.; Wang, Y.; Ke, X.; Xiao, Z.; Ding, L.; Xia, R.; et al. Organic and Solution-Processed Tandem Solar Cells with 17.3% Efficiency. *Science* **2018**, *361*, 1094–1098, doi:10.1126/science.aat2612.

101. Liu, G.; Jia, J.; Zhang, K.; Jia, X.; Yin, Q.; Zhong, W.; Li, L.; Huang, F.; Cao, Y. 15% Efficiency Tandem Organic Solar Cell Based on a Novel Highly Efficient Wide-Bandgap Nonfullerene Acceptor with Low Energy Loss. *Advanced Energy Materials* **2019**, *9*, 1803657, doi:10.1002/aenm.201803657.

102. Meng, L.; Yi, Y.-Q.-Q.; Wan, X.; Zhang, Y.; Ke, X.; Kan, B.; Wang, Y.; Xia, R.; Yip, H.-L.; Li, C.; et al. A Tandem Organic Solar Cell with PCE of 14.52% Employing Subcells with the Same Polymer Donor and Two Absorption Complementary Acceptors. *Advanced Materials* **2019**, *31*, 1804723, doi:10.1002/adma.201804723.

103. Liu, Y.; Cheng, P.; Yuan, J.; Huang, T.; Wang, R.; Meng, D.; Ndefru, B.; Zou, Y.; Sun, B.; Yang, Y. Enabling Efficient Tandem Organic Photovoltaics with High Fill Factor via Reduced Charge Recombination. *ACS Energy Lett.* **2019**, *4*, 1535–1540, doi:10.1021/acsenergylett.9b00896.

104. Tavakoli, M.M.; Si, H.; Kong, J. Suppression of Photovoltaic Losses in Efficient Tandem Organic Solar Cells (15.2%) with Efficient Transporting Layers and Light Management Approach. *Energy Technology* **2021**, *9*, 2000751, doi:10.1002/ente.202000751.

105. Huang, Y.; Meng, L.; Liang, H.; Li, M.; Chen, H.; Jiang, C.; Zhang, K.; Huang, F.; Yao, Z.; Li, C.; et al. Tandem Organic Solar Cells with 18.67% Efficiency via Careful Subcell Design and Selection. *J. Mater. Chem. A* **2022**, *10*, 11238–11245, doi:10.1039/D2TA01592G.

106. Gilot, J.; Wienk, M.M.; Janssen, R.A.J. Optimizing Polymer Tandem Solar Cells. *Advanced Materials* **2010**, *22*, E67–E71, doi:10.1002/adma.200902398.

107. Yusoff, Abd.R. bin M.; Kim, H.P.; Jang, J. All-Solution-Processed Tandem Solar Cells. *Energy Technology* **2013**, *1*, 212–216, doi:10.1002/ente.201300012.

108. Yin, Q.; Zhang, K.; Zhang, L.; Jia, J.; Zhang, X.; Pang, S.; Xu, Q.-H.; Duan, C.; Huang, F.; Cao, Y. An Efficient Binary Cathode Interlayer for Large-Bandgap Non-Fullerene Organic Solar Cells. *Journal of Materials Chemistry A* **2019**, *7*, 12426–12433, doi:10.1039/C9TA02844G.

109. Wang, D.H.; Kyaw, A.K.K.; Park, J.H. Enhanced Fill Factor of Tandem Organic Solar Cells Incorporating a Diketopyrrolopyrrole-Based Low-Bandgap Polymer and Optimized Interlayer. *ChemSusChem* **2015**, *8*, 331–336.

110. Gao, Y.; Le Corre, V.M.; Gaïtis, A.; Neophytou, M.; Hamid, M.A.; Takanabe, K.; Beaujuge, P.M. Homo-Tandem Polymer Solar Cells with VOC >1.8 V for Efficient PV-Driven Water Splitting. *Advanced Materials* **2016**, *28*, 3366–3373, doi:10.1002/adma.201504633.

111. Cui, Y.; Yao, H.; Gao, B.; Qin, Y.; Zhang, S.; Yang, B.; He, C.; Xu, B.; Hou, J. Fine-Tuned Photoactive and Interconnection Layers for Achieving over 13% Efficiency in a Fullerene-Free Tandem Organic Solar Cell. *Journal of the American Chemical Society* **2017**, *139*, 7302–7309.

112. Peng, R.; Liu, Z.; Guan, Q.; Hong, L.; Song, W.; Wei, Q.; Gao, P.; Huang, J.; Fan, X.; Wang, M.; et al. Highly Efficient Non-Fullerene Polymer Solar Cells Enabled by Novel Non-Conjugated Small-Molecule Cathode Interlayers. *Journal of Materials Chemistry A* **2018**, *6*, 6327–6334, doi:10.1039/C8TA00881G.

113. Cui, Y.; Yao, H.; Yang, C.; Zhang, S.; Hou, J. Organic Solar Cells with an Efficiency Approaching 15%. *Acta Polymerica Sinica* **2018**, 223–230.

114. Zheng, Z.; Zhang, S.; Zhang, M.; Zhao, K.; Ye, L.; Chen, Y.; Yang, B.; Hou, J. Highly Efficient Tandem Polymer Solar Cells with a Photovoltaic Response in the Visible Light Range. *Advanced Materials* **2015**, *27*, 1189–1194.

115. Chang, S.-Y.; Lin, Y.-C.; Sun, P.; Hsieh, Y.-T.; Meng, L.; Bae, S.-H.; Su, Y.-W.; Huang, W.; Zhu, C.; Li, G. High-Efficiency Organic Tandem Solar Cells With Effective Transition Metal Chelates Interconnecting Layer. *Solar RRL* **2017**, *1*, 1700139.

116. You, J.; Dou, L.; Yoshimura, K.; Kato, T.; Ohya, K.; Moriarty, T.; Emery, K.; Chen, C.-C.; Gao, J.; Li, G. A Polymer Tandem Solar Cell with 10.6% Power Conversion Efficiency. *Nature communications* **2013**, *4*, 1–10.

117. Guo, B.; Guo, X.; Li, W.; Meng, X.; Ma, W.; Zhang, M.; Li, Y. A Wide-Bandgap Conjugated Polymer for Highly Efficient Inverted Single and Tandem Polymer Solar Cells. *Journal of Materials Chemistry A* **2016**, *4*, 13251–13258.

118. Li, N.; J. Brabec, C. Air-Processed Polymer Tandem Solar Cells with Power Conversion Efficiency Exceeding 10%. *Energy & Environmental Science* **2015**, *8*, 2902–2909, doi:10.1039/C5EE02145F.

119. Li, K.; Li, Z.; Feng, K.; Xu, X.; Wang, L.; Peng, Q. Development of Large Band-Gap Conjugated Copolymers for Efficient Regular Single and Tandem Organic Solar Cells. *Journal of the American Chemical Society* **2013**, *135*, 13549–13557.

120. Shi, X.; Zuo, L.; Jo, S.B.; Gao, K.; Lin, F.; Liu, F.; Jen, A.K.-Y. Design of a Highly Crystalline Low-Band Gap Fused-Ring Electron Acceptor for High-Efficiency Solar Cells with Low Energy Loss. *Chem. Mater.* **2017**, *29*, 8369–8376, doi:10.1021/acs.chemmater.7b02853.

121. Cheng, P.; Liu, Y.; Chang, S.-Y.; Li, T.; Sun, P.; Wang, R.; Cheng, H.-W.; Huang, T.; Meng, L.; Nuryyeva, S. Efficient Tandem Organic Photovoltaics with Tunable Rear Sub-Cells. *Joule* **2019**, *3*, 432–442.

122. Yu, Z.-P.; Liu, Z.-X.; Chen, F.-X.; Qin, R.; Lau, T.-K.; Yin, J.-L.; Kong, X.; Lu, X.; Shi, M.; Li, C.-Z. Simple Non-Fused Electron Acceptors for Efficient and Stable Organic Solar Cells. *Nature communications* **2019**, *10*, 1–9.

123. Dou, L.; Gao, J.; Richard, E.; You, J.; Chen, C.-C.; Cha, K.C.; He, Y.; Li, G.; Yang, Y. Systematic Investigation of Benzodithiophene-and Diketopyrrolopyrrole-Based Low-Bandgap Polymers Designed for Single Junction and Tandem Polymer Solar Cells. *Journal of the American Chemical Society* **2012**, *134*, 10071–10079.

124. Zeng, W.; Xie, C.; Wang, W.; Li, S.; Jiang, X.; Xiong, S.; Sun, L.; Qin, F.; Han, H.; Zhou, Y. Incorporation of Hydrogen Molybdenum Bronze in Solution-Processed Interconnecting Layer for Efficient Nonfullerene Tandem Organic Solar Cells. *Solar RRL* **2020**, *4*, 1900480.

125. Raïssi, M.; Vedraine, S.; Garuz, R.; Trigaud, T.; Ratier, B. Solution Processed Cathode and Interconnecting Layer of Silver Nanowires in an Efficient Inverted Tandem Organic Solar Cells. *Solar Energy Materials and Solar Cells* **2017**, *160*, 494–502.

126. Seo, J.; Moon, Y.; Lee, S.; Lee, C.; Kim, D.; Kim, H.; Kim, Y. High Efficiency Tandem Polymer Solar Cells with MoO 3/Ni/ZnO: PEOz Hybrid Interconnection Layers. *Nanoscale Horizons* **2019**, *4*, 1221–1226.

127. Zuo, L.; Chang, C.-Y.; Chueh, C.-C.; Zhang, S.; Li, H.; K.-Y. Jen, A.; Chen, H. Design of a Versatile Interconnecting Layer for Highly Efficient Series-Connected Polymer Tandem Solar Cells. *Energy & Environmental Science* **2015**, *8*, 1712–1718, doi:10.1039/C5EE00633C.

128. Becker, T.; Trost, S.; Behrendt, A.; Shutsko, I.; Polywka, A.; Görrn, P.; Reckers, P.; Das, C.; Mayer, T.; Di Carlo Rasi, D.; et al. All-Oxide MoOx/SnOx Charge Recombination Interconnects for Inverted Organic Tandem Solar Cells. *Advanced Energy Materials* **2018**, *8*, 1702533, doi:10.1002/aenm.201702533.

129. Kim, J.-H.; Song, C.E.; Kim, B.; Kang, I.-N.; Shin, W.S.; Hwang, D.-H. Thieno[3,2-b]Thiophene-Substituted Benzo[1,2-b:4,5-B′]Dithiophene as a Promising Building Block for Low Bandgap Semiconducting Polymers for High-Performance Single and Tandem Organic Photovoltaic Cells. *Chem. Mater.* **2014**, *26*, 1234–1242, doi:10.1021/cm4035903.

130. bin Mohd Yusoff, Abd.R.; Lee, S.J.; Kim, H.P.; Shneider, F.K.; da Silva, W.J.; Jang, J. 8.91% Power Conversion Efficiency for Polymer Tandem Solar Cells. *Advanced Functional Materials* **2014**, *24*, 2240–2247, doi:10.1002/adfm.201303471.

131. Mohd Yusoff, A.R. bin; Silva, W.J. da; Pil Kim, H.; Jang, J. Extremely Stable All Solution Processed Organic Tandem Solar Cells with TiO 2 /GO Recombination Layer under Continuous Light Illumination. *Nanoscale* **2013**, *5*, 11051–11057, doi:10.1039/C3NR03068G.

132. Shi, Z.; Liu, H.; Li, J.; Wang, F.; Bai, Y.; Bian, X.; Zhang, B.; Alsaedi, A.; Hayat, T.; Tan, Z. Engineering the Interconnecting Layer for Efficient Inverted Tandem Polymer Solar Cells with Absorption Complementary Fullerene and Nonfullerene Acceptors. *Solar Energy Materials and Solar Cells* **2018**, *180*, 1–9, doi:10.1016/j.solmat.2018.02.010.

133. Che, X.; Li, Y.; Qu, Y.; Forrest, S.R. High Fabrication Yield Organic Tandem Photovoltaics Combining Vacuum- and Solution-Processed Subcells with 15% Efficiency. *Nat Energy* **2018**, *3*, 422–427, doi:10.1038/s41560-018-0134-z.

134. Ullah, F.; Chen, C.-C.; Choy, W.C.H. Recent Developments in Organic Tandem Solar Cells toward High Efficiency. *Advanced Energy and Sustainability Research* **2021**, *2*, 2000050, doi:10.1002/aesr.202000050.

135. Zang, Y.; Xin, Q.; Zhao, J.; Lin, J. Effect of Active Layer Thickness on the Performance of Polymer Solar Cells Based on a Highly Efficient Donor Material of PTB7-Th. *J. Phys. Chem. C* **2018**, *122*, 16532–16539, doi:10.1021/acs.jpcc.8b03132.

136. Riede, M.; Spoltore, D.; Leo, K. Organic Solar Cells—The Path to Commercial Success. *Advanced Energy Materials* **2021**, *11*, 2002653, doi:10.1002/aenm.202002653.

137. Schueppel, R.; Timmreck, R.; Allinger, N.; Mueller, T.; Furno, M.; Uhrich, C.; Leo, K.; Riede, M. Controlled Current Matching in Small Molecule Organic Tandem Solar Cells Using Doped Spacer Layers. *Journal of Applied Physics* **2010**, *107*, 044503, doi:10.1063/1.3277051.

138. Swapna, P.; Rao, Y.S. Modeling and Simulation of Organic Solar Cell Using Transfer Matrix Method. In Proceedings of the 2013 International Mutli-Conference on Automation, Computing, Communication, Control and Compressed Sensing (iMac4s); March 2013; pp. 196–199.

139. Shabat, M.M.; El-Khozondar, H.J.; AlShembari, A.A.; El-Khozondar, R.J. Transfer Matrix Method Application on Semiconductor-Based Solar Cell Characteristics Measurements. *Modern Physics Letters B* **2018**, *32*, 1850346.

140. El-Khozondar, H.J.; Shabat, M.M.; AlShembari, A.N. Characteristics of Si-Solar Cell (PV) Waveguide Structure Using Transfer Matrix Method. In Proceedings of the 2017 International Conference on Promising Electronic Technologies (ICPET); IEEE, 2017; pp. 99–102.

141. Shabat, M.M.; Nassar, S.A.; Roskos, H.G. Modeling Plasmonic Solar Cells with Noble Metal Nanoparticles Using the Finite Difference Time Domain Method. *Romanian Journal of Physics* **2020**, *65*, 609.

142. Ghamande, M. Optical Modeling of Organic Photovoltaic Solar Cells, University of Akron, 2011.

143. Yang, F.; Forrest, S.R. Photocurrent Generation in Nanostructured Organic Solar Cells. *ACS nano* **2008**, *2*, 1022–1032.

144. Organic Heterojunctions in Solar Cells Available online: http://depts.washington.edu/cmditr/modules/opv/organic_heterojunctions_in_solar_cells.html (accessed on 24 February 2023).

145. Parkhomenko, H.; Solovan, M.; Mostovyi, A.; Orletskyi, I.; Brus, V. Electrical and Photoelectric Properties of Organic-Inorganic Heterojunctions PEDOT:PSS/n-CdTe. *East European Journal of Physics* **2021**, 43–48, doi:10.26565/2312-4334-2021-4-04.

146. Mishra, A.; Sharma, G.D. Harnessing the Structure-Performance Relationships in Designing Non-Fused Ring Acceptors for Organic Solar Cells. *Angewandte Chemie* **2023**.

147. Li, D.; Deng, N.; Fu, Y.; Guo, C.; Zhou, B.; Wang, L.; Zhou, J.; Liu, D.; Li, W.; Wang, K. Fibrillization of Non-Fullerene Acceptors Enables 19% Efficiency Pseudo-Bulk Heterojunction Organic Solar Cells. *Advanced Materials* **2023**, *35*, 2208211.

148. Tamai, Y. What's Next for Organic Solar Cells? The Frontiers and Challenges. *Advanced Energy and Sustainability Research* **2023**, *4*, 2200149.

149. Mao, L.; Sun, L.; Luo, B.; Jiang, Y.; Zhou, Y. Patching Defects in the Active Layer of Large-Area Organic Solar Cells. *Journal of Materials Chemistry A* **2018**, *6*, 5817–5824.

150. Goh, Y.; Kim, T.; Yang, J.-H.; Choi, J.H.; Hwang, C.-S.; Cho, S.H.; Jeon, S. Defects and Charge-Trapping Mechanisms of Double-Active-Layer In–Zn–O and Al–Sn–Zn–In–O Thin-Film Transistors. *ACS Applied Materials & Interfaces* **2017**, *9*, 9271–9279.

151. Ouslimane, T.; Et-Taya, L.; Elmaimouni, L.; Benami, A. Impact of Absorber Layer Thickness, Defect Density, and Operating Temperature on the Performance of MAPbI3 Solar Cells Based on ZnO Electron Transporting Material. *Heliyon* **2021**, *7*, e06379.

152. Schopp, N.; Luong, H.M.; Luginbuhl, B.R.; Panoy, P.; Choi, D.; Promarak, V.; Brus, V.V.; Nguyen, T.-Q. Understanding Interfacial Recombination Processes in Narrow-Band-Gap Organic Solar Cells. *ACS Energy Lett.* **2022**, *7*, 1626–1634, doi:10.1021/acsenergylett.2c00502.

153. Schopp, N.; Brus, V.V.; Lee, J.; Bazan, G.C.; Nguyen, T.-Q. A Simple Approach for Unraveling Optoelectronic Processes in Organic Solar Cells under Short-Circuit Conditions. *Advanced Energy Materials* **2021**, *11*, 2002760.

154. Yue, M.; Su, J.; Zhao, P.; Lin, Z.; Zhang, J.; Chang, J.; Hao, Y. Optimizing the Performance of CsPbI 3-Based Perovskite Solar Cells via Doping a ZnO Electron Transport Layer Coupled with Interface Engineering. *Nano-Micro Letters* **2019**, *11*, 1–14.

155. Tian, F.; Guo, D.; Liu, B.; Zhang, Q.; Tian, Q.; Ullah, R.; Xin, X. A Novel Concatenated Coded Modulation Based on GFDM for Access Optical Networks. *IEEE Photonics Journal* **2018**, *10*, 1–8.

156. Yuan, B.; Zhou, Y.; Liu, T.; Li, C.; Cao, B. Extending the Absorption Spectra and Enhancing the Charge Extraction by the Organic Bulk Heterojunction for CsPbBr3 Perovskite Solar Cells. *ACS Sustainable Chemistry & Engineering* **2023**.

157. Isikgor, F.H.; Zhumagali, S.; T. Merino, L.V.; De Bastiani, M.; McCulloch, I.; De Wolf, S. Molecular Engineering of Contact Interfaces for High-Performance Perovskite Solar Cells. *Nature Reviews Materials* **2023**, *8*, 89–108.

158. Camaioni, N.; Carbonera, C.; Ciammaruchi, L.; Corso, G.; Mwaura, J.; Po, R.; Tinti, F. Polymer Solar Cells with Active Layer Thickness Compatible with Scalable Fabrication Processes: A Meta-Analysis. *Advanced Materials* **2023**, 2210146.

159. Zhao, X.; An, Q.; Zhang, H.; Yang, C.; Mahmood, A.; Jiang, M.; Jee, M.H.; Fu, B.; Tian, S.; Woo, H.Y. Double Asymmetric Core Optimizes Crystal Packing to Enable Selenophene-Based Acceptor with Over 18% Efficiency in Binary Organic Solar Cells. *Angewandte Chemie International Edition* **2023**, *62*, e202216340.

160. Meng, L.; Liang, H.; Song, G.; Li, M.; Huang, Y.; Jiang, C.; Zhang, K.; Huang, F.; Yao, Z.; Li, C. Tandem Organic Solar Cells with Efficiency over 19% via the Careful Subcell Design and Optimization. *Science China Chemistry* **2023**, 1–8.

161. Yang, H.; Chen, W.; Yu, Y.; Shen, Y.; Yang, H.; Li, X.; Zhang, B.; Chen, H.; Cheng, Q.; Zhang, Z. Regulating Charge Carrier Recombination in the Interconnecting Layer to Boost the Efficiency and Stability of Monolithic Perovskite/Organic Tandem Solar Cells. *Advanced Materials* **2023**, *35*, 2208604.

162. Xie, C.; Liu, Y.; Wei, W.; Zhou, Y. Large-Area Flexible Organic Solar Cells with a Robust Silver Nanowire-Polymer Composite as Transparent Top Electrode. *Advanced Functional Materials* **2023**, *33*, 2210675.

163. Ghosh, B.K.; Jha, P.K.; Ghosh, S.K.; Biswas, T.K. Organic Solar Cells Pros and Cons: Outlooks toward Semitransparent Cell Efficiency and Stability. *AIP Advances* **2023**, *13*, 020701.

164. Schopp, N.; Brus, V.V.; Nguyen, T.-Q. On Optoelectronic Processes in Organic Solar Cells: From Opaque to Transparent. *Advanced Optical Materials* **2021**, *9*, 2001484.

165. Zeiske, S.; Sandberg, O.J.; Zarrabi, N.; Li, W.; Meredith, P.; Armin, A. Direct Observation of Trap-Assisted Recombination in Organic Photovoltaic Devices. *Nat Commun* **2021**, *12*, 3603, doi:10.1038/s41467-021-23870-x.

166. Kotadiya: A Window to Trap-Free Charge Transport... - Google Scholar Available online: https://scholar.google.com/scholar_lookup?title=A%20window%20to%20trap-free%20charge%20transport%20in%20organic%20semiconducting%20thin%20films&journal=Nat.%20Mater.&doi=10.1038%2Fs41563-019-0473-6&volume=18&pages=1182-1186&publication_year=2019&author=Kotadiya%2CNB&author=Mondal%2CA&author=Blom%2CPWM&author=Andrienko%2CD&author=Wetzelaer%2CG-JAH (accessed on 20 March 2023).

167. Nicolai: Unification of Trap-Limited Electron Transport... - Google Scholar Available online: https://scholar.google.com/scholar_lookup?title=Unification%20of%20trap-limited%20electron%20transport%20in%20semiconducting%20polymers&journal=Nat.%20Mater.&doi=10.1038%2Fnmat3384&volume=11&pages=882-887&publication_year=2012&author=Nicolai%2CHT (accessed on 20 March 2023).

168. Schopp, N.; Brus, V.V.; Lee, J.; Dixon, A.; Karki, A.; Liu, T.; Peng, Z.; Graham, K.R.; Ade, H.; Bazan, G.C. Effect of Palladium-Tetrakis (Triphenylphosphine) Catalyst Traces on Charge Recombination and Extraction in Non-Fullerene-Based Organic Solar Cells. *Advanced Functional Materials* **2021**, *31*, 2009363.

169. Yeboah, D.; Singh, J. Influence of Charge Carrier Extraction Parameters on the Performance of Bulk Heterojunction Organic Solar Cells. *J Mater Sci: Mater Electron* **2018**, *29*, 13354–13360, doi:10.1007/s10854-018-9460-y.

170. Street, R.A.; Krakaris, A.; Cowan, S.R. Recombination through Different Types of Localized States in Organic Solar Cells. *Advanced Functional Materials* **2012**, *22*, 4608–4619.

171. Lee, J.; Ko, S.-J.; Seifrid, M.; Lee, H.; Luginbuhl, B.R.; Karki, A.; Ford, M.; Rosenthal, K.; Cho, K.; Nguyen, T.-Q. Bandgap Narrowing in Non-Fullerene Acceptors: Single Atom Substitution Leads to High Optoelectronic Response beyond 1000 Nm. *Advanced Energy Materials* **2018**, *8*, 1801212.